

The University of Alabama in Huntsville

129 f

Final Report for Contract NAG8-834

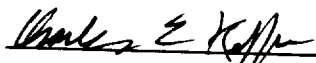
Due Date: June 25, 1994

"Theoretical and Experimental Studies Relevant to  
Interpretation of Auroral Emissions"

Submitted to

George C. Marshall Space Flight Center  
Space Science Laboratory  
National Aeronautics and Space Administration  
Marshall Space Flight Center, AL 35812

by



Charles E. Keffer

Principal Investigator

The University of Alabama in Huntsville

Physics Department

Huntsville, AL 35899

N94-36421

Unclas

G3/93 0012622

(NASA-CR-196032) THEORETICAL AND  
EXPERIMENTAL STUDIES RELEVANT TO  
INTERPRETATION OF AURORAL EMISSIONS  
Final Report (Alabama Univ.)  
129 p

419020

## **Theoretical and Experimental Studies Relevant to Interpretation of Auroral Emissions**

2

### **Introduction**

In recent years, there has been an increasing awareness of the fragile balance required to maintain the Earth's environment in a healthy condition. The Earth's upper atmosphere and its interaction with the Sun are recognized as playing a crucial role in maintaining this balance. Understanding of this link between the Earth and Sun contributes significantly to our understanding of Earth's atmosphere, climate, weather, magnetic storm activity, etc. Despite a rapidly increasing data base of knowledge on the solar-terrestrial environment much remains to be learned. Optical emissions from upper atmospheric constituents represent a fundamental tool for understanding both the composition and the physical processes that contribute to the ability of the atmosphere to sustain a high quality of life on the Earth. Space-based observation platforms are frequently able to make measurements of upper atmospheric emissions that are either impossible to make from the ground or superior to their ground-based counterparts. Specifically, auroral imaging from a space-based platform makes it possible to determine the total auroral energy influx and the characteristic energy of the incident auroral particles. In addition, it is possible, through modeling, to map and relate these parameters from the thermosphere and ionosphere to the various regions of the Earth's magnetosphere.

This report describes the accomplishments of a program designed to develop the tools necessary to interpret auroral emissions measured from a space-based platform. The research was divided into two major areas. The first area was a laboratory study designed to improve our understanding of the space vehicle external environment and how it will affect the space-based measurement of auroral emissions. Facilities have been setup and measurements taken to simulate the gas phase environment around a space vehicle; the radiation environment encountered by an orbiting vehicle that passes through the Earth's radiation belts; and the thermal environment of a vehicle in Earth orbit. The second major area of study was a modeling program to develop the capability of using auroral images at various wavelengths to infer the total energy influx and characteristic energy of the incident auroral particles. An ab initio auroral calculation has been added to the extant ionospheric/thermospheric global modeling capabilities within our group. Once the addition of the code was complete, the combined model was used to compare the relative intensities and behavior of various emission sources (dayglow, aurora, etc.).

The work completed under this grant has provided an essential foundation for understanding the FUV auroral images that will be available after deployment of the Ultraviolet Imager (UVI) on the Global Geospace Science (GGS) POLAR satellite. Thus, a significant contribution has been made to the field of space-based auroral imaging.

### **Cross Section Facility**

One of the fundamental factors that affects a space-based observing platform is the gas phase environment surrounding the platform. Atomic oxygen, in particular, plays a pivotal role in the induced environment for vehicles in low Earth orbit(LEO). Phenomena such as "shuttle

glow," erosion of spacecraft surfaces, and the "contaminant cloud" surrounding a spacecraft affect all instruments making observations from space. One of the tasks of this grant has been the development of a Cross Section Facility to address these issues. The Facility consists of a crossed molecular beam apparatus with a fast atomic oxygen beam and a thermal energy beam of another atmospheric gas ( $N_2$ ,  $O_2$ , etc.). A rotatable mass spectrometer serves as a sensitive particle detector. The Facility is described in greater detail in the paper entitled "Laboratory Facility for Simulation of Vehicle-Environment Interactions" that was presented by the Principal Investigator, Dr. Charles E. Keffer at the Vehicle-Environment Interactions Conference held at the Applied Physics Laboratory, Laurel, Maryland on March 11-13, 1991. The paper is attached as Appendix A of this report.

Initial work with the Cross Section Facility focused on a thorough characterization of the Facility. This was essential to ensure that measurements of gas-gas interactions such as differential scattering cross sections could be made without any serious systematic errors. Specifically, we have completed characterization of thermal energy beams of  $O_2$  and  $N_2$  to determine their spatial and temporal characteristics. This information was used to assist in the measurement of the thermal energy differential scattering cross section for collisions of  $O_2$  on  $N_2$ . Results of these measurements were compared with classical scattering theory and were found to be in good agreement (Figure 1). This serves as an indication that there are no serious systematic errors in differential scattering cross section measurements made with our Facility.

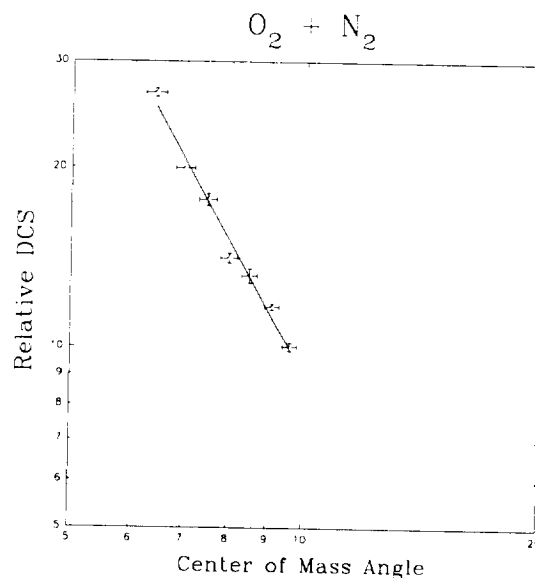


Figure 1: Differential scattering cross section for  $O_2$  on  $N_2$ .

Another major area of Cross Section Facility work was the development and characterization of an energetic, high flux source of atomic oxygen. The velocity and composition of the source were measured a large number of times. Beam velocity measurements are illustrated in Figure 2. Two peaks are evident in the intensity Vs time plot of the mass spectrometer signal. The first peak is due to photons from the plasma discharge formed from dissociation and ionization of molecular oxygen by a  $CO_2$  laser pulse. These photons arrive at

the detector essentially coincident with the formation of the fast O atoms. The second peak in the figure is due to the fast O atoms. The velocity of the atoms is the known distance from the pulsed valve to the mass spectrometer divided by the time between the two peaks since this time represents the time of flight for the fast O atoms. The velocity for the measurement shown is 6.8 km/sec. Mass spectrometer measurements of the fast oxygen beam demonstrated that it was composed predominantly of oxygen atoms. Some oxygen molecules, a small percentage of atomic oxygen ions, and some impurities are also present in the fast oxygen beam. Table 1 summarizes the characteristics of the energetic oxygen atom source.

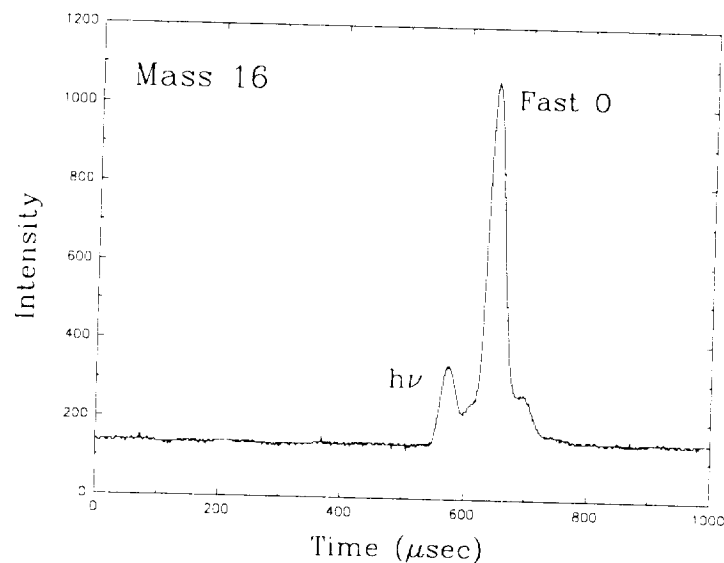


Figure 2: Fast atomic oxygen pulse.

Velocity Range	3 to 11 km/sec
Oxygen Atoms	> 80 %
Oxygen Molecules	< 20 %
Total Ions	< 1 %
Impurities (H, N <sub>2</sub> , etc.)	< 1 %

Table 1: Energetic oxygen atom source operating characteristics.

This work completes the development of a Cross Section Facility that is capable of performing a wide variety of vehicle-environment interaction measurements including both gas phase and gas-surface phenomena. This versatile tool should find extensive use in making laboratory measurements that can help in the interpretation of observations made from space-based platforms.

### Induced Environment Workshop

A workshop sponsored by this grant provided a forum for presentation and discussion of

5  
the latest research in the area of space vehicle induced external environments. A group of nationally recognized experts on space vehicle contamination met January 30-31, 1991 in Huntsville, Alabama. Twenty invited participants each presented a paper in their particular area of expertise. The papers and discussion addressed three questions:

- (1) What is our current state of knowledge of the likely induced external environment for a large space-based platform in low Earth orbit?
- (2) What progress has been made during the last two years in the vehicle contamination knowledge data base and in the predictive capability of induced vehicle contamination for future missions?
- (3) What issues remain unresolved and are the most important to investigate in future studies?

Appendix B contains the summary report from the workshop, an agenda of the meeting, and a list of the attendees. The Principal Investigator, Dr. Charles E. Keffer, presented a paper entitled "Cross Section Work at UAH/MSFC" at the workshop.

### Radiation Testing

As the Ultraviolet Imager (UVI) neared completion, the laboratory portion of this study began to concentrate on the effect of the natural and induced space environment on the UVI. The UVI is a part of the International Solar Terrestrial Physics (ISTP) mission to study the Earth's magnetosphere. It will be on a polar orbiting satellite exposed to the high radiation environment of space during its nominal three year mission lifetime. Of particular concern for the UVI is the all-dielectric multilayer interference reflection and transmission filters which are a part of the UVI optical system. The UVI filters will receive a radiation dose on orbit of  $< 250$  krad. Previous laboratory studies of high-energy radiation damage to optical materials at ultraviolet wavelengths are primarily transmittance measurements of uncoated substrates (Heath and Sacher, 1966; Nicoletta and Eubanks, 1972; Reft *et al.*, 1980; Pellicori *et al.*, 1979; Hass and Hunter, 1979; Grillot and Rosenberg, 1989). Prior to the work under this grant, the extent of damage, if any, that the UVI filters will likely experience from this radiation exposure was unknown. We have, therefore, performed a series of tests to simulate the anticipated radiation dose and to measure its impact on the UVI filters.

We selected 14 single layer thin films, 4 uncoated substrates, 2 multilayer transmission filters, and 2 multilayer reflection filters for radiation damage study. A  $^{60}\text{Co}$  source at Goddard Space Flight Center irradiated seven of the single layer thin films, 2 of the uncoated substrates, and all of the multilayer filters with 250 krad of gamma radiation. The remaining 9 samples served as controls with no irradiation. Table 2 shows a matrix of the 22 samples used with the substrate and thin film type shown together with the UVI filter to which it is similar. The complete set of samples is analogous to the substrates, thin films, and filters that make up the UVI optical system.

Sample	Substrate	Coating	Radiation/Control	UVI Filter
$\text{Al}_2\text{O}_3$ 1/2	Fused Silica	$\text{Al}_2\text{O}_3$	Radiation	TSOLAR
$\text{Al}_2\text{O}_3$ 2/2	Fused Silica	$\text{Al}_2\text{O}_3$	Control	none

Sample	Substrate	Coating	Radiation/Control	UVI Filter
BaF <sub>2</sub> 1/2	MgF <sub>2</sub>	BaF <sub>2</sub>	Radiation	T1304,T1356,TLBHS
BaF <sub>2</sub> 2/2	MgF <sub>2</sub>	BaF <sub>2</sub>	Control	none
CaF <sub>2</sub> 1/2	MgF <sub>2</sub>	CaF <sub>2</sub>	Radiation	none
CaF <sub>2</sub> 2/2	MgF <sub>2</sub>	CaF <sub>2</sub>	Control	none
F14-A	MgF <sub>2</sub>	BaF <sub>2</sub> ,MgF <sub>2</sub>	Radiation	none
Fused Silica uncoated 1/2	Fused Silica	none	Radiation	TLBHL,TSOLAR
Fused Silica uncoated 2/2	Fused Silica	none	Control	none
HfO <sub>2</sub> 1/2	MgF <sub>2</sub>	HfO <sub>2</sub>	Radiation	none
HfO <sub>2</sub> 2/2	MgF <sub>2</sub>	HfO <sub>2</sub>	Control	none
LaF <sub>3</sub> 1/2	MgF <sub>2</sub>	LaF <sub>3</sub>	Radiation	R1304,R1356,RLBHS,RLBHL, T1304,T1356,TLBHS
LaF <sub>3</sub> 2/2	MgF <sub>2</sub>	LaF <sub>3</sub>	Control	none
MF45-C	MgF <sub>2</sub>	BaF <sub>2</sub> ,MgF <sub>2</sub>	Radiation	none
MgF <sub>2</sub> 1/2	MgF <sub>2</sub>	MgF <sub>2</sub>	Radiation	all
MgF <sub>2</sub> 2/2	MgF <sub>2</sub>	MgF <sub>2</sub>	Control	none
MgF <sub>2</sub> uncoated 1/2	MgF <sub>2</sub>	none	Radiation	none
MgF <sub>2</sub> uncoated 2/2	MgF <sub>2</sub>	none	Control	none
RF135L/B	Fused Silica	LaF <sub>3</sub> /MgF <sub>2</sub>	Radiation	none
RF135L/D	Fused Silica	LaF <sub>3</sub> /MgF <sub>2</sub>	Radiation	none
SiO <sub>2</sub> 1/2	MgF <sub>2</sub>	SiO <sub>2</sub>	Radiation	TLBHL
SiO <sub>2</sub> 2/2	MgF <sub>2</sub>	SiO <sub>2</sub>	Control	none

Table 2. Summary of coatings and measurements.

A series of reflectance and transmittance measurements has been performed on the 22 samples shown in Table 2. The preradiation measurements were performed in a hydrocarbon-free cryopumped vacuum chamber at a pressure below  $10^{-5}$  Torr. A deuterium lamp with a MgF<sub>2</sub> window together with a 0.2-m vacuum monochromator provided 1 nm FWHM spectral resolution over the 120 to 180 nm wavelength range. Folding and collimating optics and a 6 mm diameter aperture limited the light incident on the eight position filter wheel holding the 12.5 mm diameter substrates to an area approximately 1/4th the area of the thin film. A photomultiplier tube with a MgF<sub>2</sub> window and a semi-transparent CsI photocathode served as the detector for all measurements. The postradiation measurements were accomplished in another hydrocarbon-free cryopumped vacuum chamber also at a pressure below  $10^{-5}$  Torr. A similar deuterium lamp, 0.2-m vacuum monochromator, and aperture were used for the postradiation measurements. However, the second chamber did not have any folding and collimating optics. The same CsI photomultiplier tube and eight position filter wheel was used for both the pre- and postradiation

measurements. Reflectance measurements were performed at a  $45^\circ$  angle of incidence while transmittance was measured at normal incidence. Figures 3 and 4 illustrate the optical configurations for the two vacuum chambers used.

For the reflection measurements, two identical scans from 120 to 180 nm were performed on each substrate prior to their radiation exposure. Filter RF135L/GII was measured as a control on every reflection measurement to check the reliability and reproducibility of the data from scan to scan. The RF135L/GII control ensured that no systematic errors were introduced when the vacuum chamber was vented and a new set of substrates was installed. Two identical scans from 120 to 180 nm were also performed on each substrate during the transmission measurements. Filter  $\text{MgF}_2$  17 was measured on every transmission measurement as a check on the scan to scan reliability and reproducibility. The RF135L/GII and  $\text{MgF}_2$  17 filters also provided traceability between the two vacuum chambers used in the pre- and postradiation measurements.

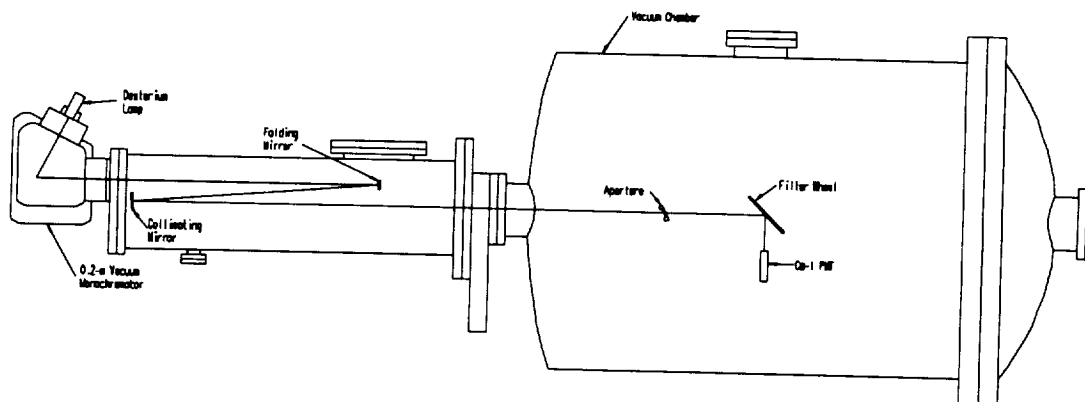


Figure 3. Optical configuration for preradiation measurements.

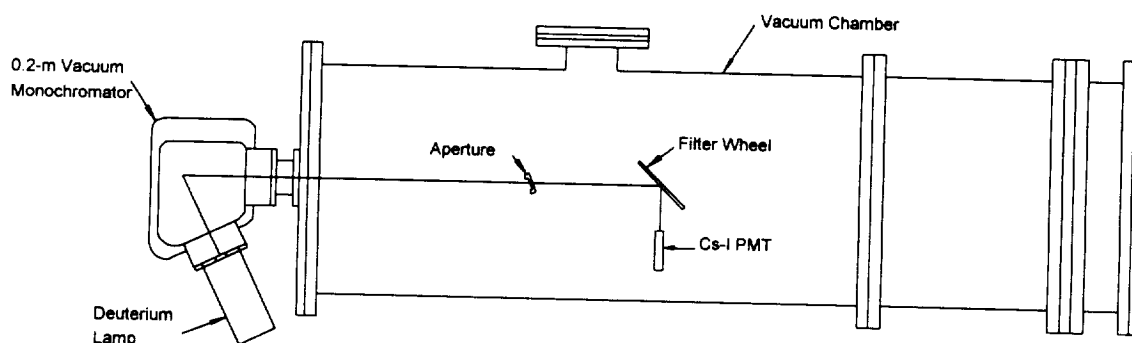


Figure 4. Optical configuration for postradiation measurements.

Repeated measurements of the RF135L/GII and  $\text{MgF}_2$  17 filters have led to an estimated run to run uncertainty of approximately  $\pm 3\%$ . Of the 13 irradiated samples, only 1 had any statistically significant differences in the 120 to 180 nm range after radiation exposure. The uncoated  $\text{MgF}_2$  sample had an apparent 5% absorption short of 160 nm before radiation exposure that was not present after radiation exposure.

The primary wavelength range of interest to the UVI is 120 to 180 nm. However, most ultraviolet optical materials that have been studied in the bulk form have their strongest radiation-induced absorption bands at wavelengths longer than 180 nm. So, another set of measurements was made from 160 to 300 nm where the irradiated samples were compared to their equivalent control samples because no preradiation measurements were made in this wavelength range. A 3-5% radiation-induced absorption band centered at 260 nm was discovered in two of the  $\text{MgF}_2$  substrates. This agrees with other published results on radiation damage to  $\text{MgF}_2$  crystals. Since 260 nm is outside the wavelength range of interest to the UVI, however, this radiation damage is not a concern for the UVI.

In summary, it appears that none of the samples tested have experienced any major radiation induced changes in reflectance or transmittance in the wavelength range of interest to the UVI. Since the UVI filters are made exclusively from materials that we have tested, it is anticipated that they will suffer less than approximately 5% loss in reflectance or transmittance during their nominal 3 year mission lifetime.

Two papers were written on the radiation testing results for the UVI filter materials. Preliminary results were presented on July 16, 1993, in a paper entitled "Radiation Damage Effects in Far Ultraviolet Filters and Substrates" at the X-Ray and Ultraviolet Polarimetry session of the SPIE International Symposium on Optics, Imaging, and Instrumentation in San Diego, California. Complete results have been presented in a paper entitled "Radiation Damage Effects in Far Ultraviolet Filters, Thin Films, and Substrates" that is scheduled for publication in Applied Optics in 1994. Copies of these two papers are attached to this report as Appendix C and Appendix D, respectively.

## Thermal Testing

The Ultraviolet Imager is passively cooled by radiative heat transfer from the instrument to the 3 °K thermal background of space. The performance of the UVI in this thermal environment is a key factor in the success of the mission. The radiative coupling between the UVI and the 3 °K thermal background of space must meet the critical cooling requirements for the instrument. These include a CCD detector temperature below - 55 °C for noise reduction, an optical bench temperature near room temperature to prevent misalignments caused by thermal expansion or contraction, and heat removal from "hot" electronic parts to prevent failures. We have, therefore, designed and carried out several tests of the UVI thermal performance.

A test chamber setup that was designed to simulate the thermal environment of the UVI on orbit was built into the VUV calibration vacuum system. The UVI was mounted on a baseplate cooled or heated over the nominal temperature range of - 20 to 30 °C by a recirculating water and ethanol mixture. A second cold plate was suspended approximately 2" above the UVI radiator. This cold plate was painted black to increase its emissivity and thus improve the radiative heat transfer from the UVI to the cold plate. Liquid nitrogen was flowed through the upper cold plate so that its temperature approached 77 °K. Several thermistors and thermocouples monitored the temperature at strategic locations.

Several key questions were addressed in this thermal test. Will the CCD reach its operational target temperature of < - 55 °C? Can the optical bench be maintained near room



temperature with 10 watts of available heater power? Will the electronics remain sufficiently warm during survival mode conditions? Do the "hot" electronic parts have adequate cooling? In all cases, the UVI thermal performance was found to be satisfactory. All the required thermal vacuum cycles and thermal balance tests were also completed.

### UVI Optical System Testing

The UVI is designed to measure atomic oxygen auroral emissions at 130.4 and 135.6 nm, N<sub>2</sub> Lyman-Birge-Hopfield (LBH) auroral emissions from 140 to 160 nm and from 160 to 180 nm, and the scattered sunlight from 180 to 210 nm. High sensitivity at the selected wavelength coupled with a high rejection ratio for other wavelengths is required. The UVI uses a filter wheel with five filter sets for the five different wavelength ranges. Each filter set consists of 3 reflection filters and 1 transmission filter.

The success of the UVI optical system depends on the correct design and performance of these filters. Accordingly, measurements have been completed of the reflectance or transmittance of all of the flight filters to verify that they achieve the necessary performance requirements. The measurements were completed in the same manner as the radiation test measurements and using a setup similar to that illustrated in Figure 4. The net transmittance for each filter set is shown in Figure 5.

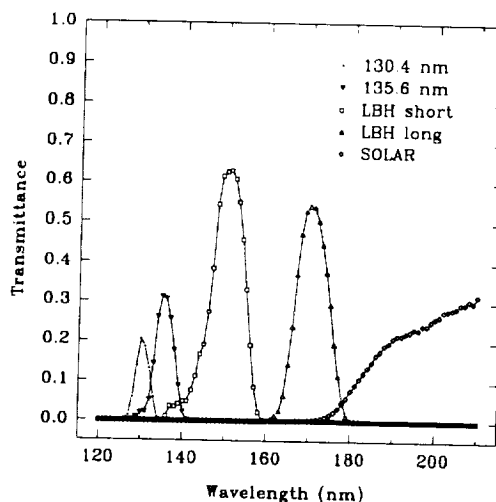


Figure 5: UVI flight filter sets.

In addition to the five filter sets, the UVI optical system has three telescope mirrors, a MgF<sub>2</sub> window in the aperture door, and a folding mirror for diverting light from the primary detector system to a secondary detector system if desired. Reflectance measurements have been completed on test coupons coated at the same time as the folding mirror and each telescope mirror. Reflectance values of 70% are typical in the 120 to 210 nm range. Transmittance measurements have also been completed on several conductive films designed for use on the MgF<sub>2</sub> window in the aperture door.

## **Auroral Modeling**

An unambiguous interpretation of auroral emissions is dependent on a successful modeling program. In particular, the modeling program must explicitly include the auroral electrons and the associated auroral emissions while maintaining the capability of incorporating the auroral results within a comprehensive global ionospheric model. The long term goal of our modeling program is to develop the capability of using auroral images at various wavelengths to infer the total energy influx and characteristic energy of the incident auroral particles. In addition, we want to be able to deduce additional parameters, e.g., neutral composition and ionospheric conductances.

In our research plan we proposed a program to incorporate an auroral code into our existing global model and conduct studies with the resultant computer model. As an associated part of the second task, we also provided support for two meetings of the members of the ISTP Ultraviolet Imager (UVI) science team. As described below, we have successfully met these goals.

## **Integration of Models**

We began this program with a global ionospheric model (FLIP) in a fully interhemispheric format, including photoelectron transport. The model accounted for the chemistry of all major emitting species, solved for key mechanisms, and provided the full odd nitrogen chemistry (see for example, Torr *et al.*, 1990; Torr, 1983; Torr and Torr, 1982; Young *et al.*, 1980). The global model, however, did not include the capabilities to model auroral electrons and their resultant emissions. The treatment of photoelectron transport within the global model does, however, readily lend itself to inclusion of auroral electrons. In preparation of our long term modeling needs, we had previously developed (with P. G. Richards) a two-stream auroral electron energy code that determines the energy degradation of the primary spectrum as a function of energy and altitude; it is fully described in Richards and Torr, [1990].

The integration of our two-stream auroral code with the global FLIP model is central to the modeling aspect of this program. The auroral electron code accurately models energy degradation of an incident electron flux and resultant auroral emissions. It has no knowledge, however, of the chemistry and dynamics of the global ionosphere-thermosphere. The FLIP is an excellent representation of these processes but does not include the auroral processes. The combined model allows simultaneous modeling of auroral emissions superimposed on underlying airglow. The updated FLIP model now accepts auroral production data from the auroral model as standard input data and is available for studies that exploit its combined capabilities.

## **High Latitude Extensions**

The FLIP model is a closed field line model and assumes, incorrectly, that the field lines remain closed throughout the polar regions. Attempts to model these regions with closed field

lines lead to infinitely large field lines and attendant computational difficulties. We had previously thought the FLIP model would have to be modified to include open field lines. Such a modification would have been an extensive project. Our work under this grant has shown, however, that a good model of the airglow can be obtained by turning off the field-line diffusive solutions in the FLIP code. This has the advantage of using the existing code with only minimal modification.

In addition to being able to run at polar latitudes, the FLIP model must also be modified to take account of several high latitude mechanisms. One of the more significant mechanisms is the drift of ionospheric plasma due to local electric fields. Plasma convection throughout the polar region can significantly alter the plasma densities relative to a static model which has the feet of the flux tubes anchored to the Earth's surface. Plasma convection is controlled by ionospheric electric fields which are intimately connected with the magnetospheric-ionospheric current systems and are generally not readily modeled because of their complexity. There are a number of empirical algorithms, however, which accurately model the overall convection patterns. We adapted the convection model of Sojka *et al.* [1986] as a first step to allow the FLIP model to include plasma drift. We are currently able to specify plasma trajectories as a function of time and interplanetary magnetic field strength and direction. This capability is significant in its own right and can be used in numerous studies. It will also form the basis for future extensions to the FLIP code.

## **Modeling Studies**

The combined codes have enabled studies of superimposed airglow and aurora. In addition, the models have been used to calculate conductances due to both EUV and auroral sources. Details of these studies are given below.

## **FUV Auroral Emissions**

Rees and Luckey [1974] showed that measurements of the 6300 Å emission of atomic oxygen and the 4278 Å emission of ionized molecular nitrogen could be used to infer the characteristic energy of the incident auroral particle flux. In this technique, the energy dependence is provided by the collisional deactivation of the 6300 Å emission at lower altitudes.

Strickland *et al.* [1983] demonstrated the same capabilities using FUV auroral emissions. In particular, they proposed the use of the O I (1356 Å) and N<sub>2</sub> Lyman-Birge-Hopfield (LBH) emissions as remote diagnostics of the auroral process. Instead of quenching mechanisms, the FUV technique relied on absorption of O<sub>2</sub> at lower altitudes to supply an energy dependence. In a previous study [Germany *et al.*, 1990], carried out under contract NAS8-37586, we examined the stability of FUV emission ratios formed from atomic oxygen and LBH emissions as a function of likely changes in the neutral atmosphere. These are the FUV emissions we studied under this grant and are shown in Figure 6. Some emissions (O I 1356 and LBH 1464) vary significantly with average energy, while others (LBH 1838) are relatively independent of energy and are indicators of the total flux. They found that emission ratios formed from the O I (1356 Å) emission varied significantly with seasonal and solar cyclic variations. On the other hand,

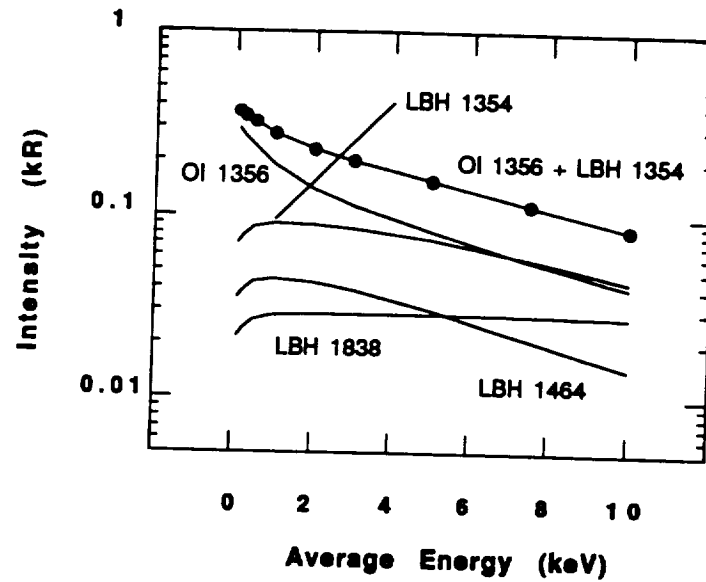


Figure 6. FUV auroral emissions used as diagnostics of the auroral processes.

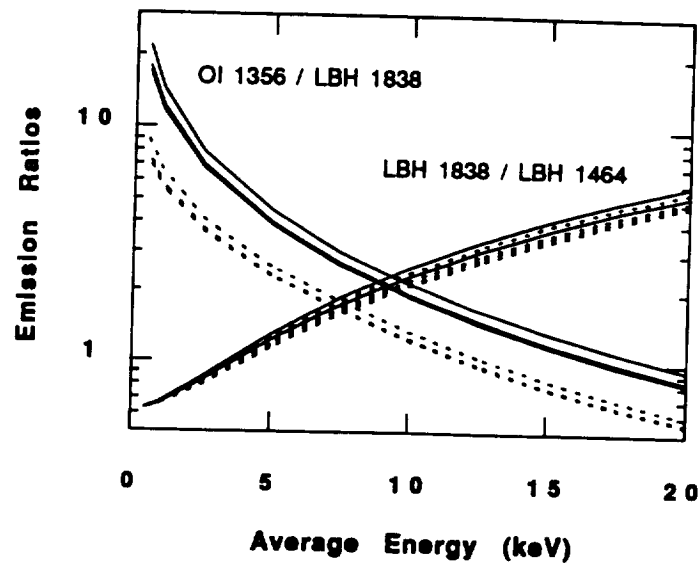


Figure 7. Ratio of FUV auroral emissions as a function of average energy. The 1356 Å emission ratio has a greater sensitivity, but also has a greater variability than the LBH ratio. Dashed lines are for summer conditions (day 173) and solid lines for winter (day 356). For each day, solar activity is varied by changing the F107 and  $A_p$  indices. The largest intensity ratios are obtained at solar minimum activity; the smallest ratios occur at solar maximum.

emission ratios employing long- and short-wavelength LBH emissions were much less sensitive to changes in the neutral atmosphere (Figure 7). Furthermore, blending of the O I (1356 Å) and LBH (1354 Å) emissions represents a serious observational difficulty. Consequently, the LBH emission ratios are potentially more valuable as remote diagnostics of the incident auroral flux than similar ratios using the O I (1356 Å) emission.

Much of our work under this grant on the use of auroral LBH and OI emissions as remote diagnostics of auroral processes is summarized by Germany *et al.* [1994]. A reprint of this paper is included in Appendix E. We examined the dependence of these emissions and their ratios on the shape of the energy distribution of the auroral electrons. We were particularly concerned that the column-integrated emissions might be overly sensitive to the energy distribution of the incident energy flux. Since different physical processes lead to different energy distributions there is not a single parameterization which applies to all situations. Furthermore, since the energy distribution is not typically known for remote sensing applications, a dependence on the distribution could severely limit the information which could be retrieved from the emissions. Strickland *et al.* [1983] examined the dependence of FUV auroral emissions on the choice of either a Gaussian or a Maxwellian incident energy spectrum. We extended that study by modeling auroral emissions resulting from incident energy distributions of different widths and shapes to determine whether changes in energy spectra might obscure, or render ambiguous, our determination of the incident characteristic energy from FUV emission ratios. In addition to varying the functional dependence of the energy distribution, we looked at the effects of varying its width and its low energy behavior. Results are shown in Figures 8-10.

Fortunately, we found that modeled column-integrated emissions showed less than 30% variance with changes in the shape and width of the incident energy spectrum, provided the average energy and total energy flux of the energy distribution are held constant. Our choice of distributions was not necessarily realistic; the distributions were chosen to illustrate extremes of shape and width. It is significant, in light of these choices, that a change of energy distribution affects the column emissions by less than 30%. This is relatively small, given the other uncertainties associated with auroral imaging. Regardless of the energy distributions modeled, we found that the differences in resulting emissions are governed primarily by the average energy of the distributions and the relative widths of the distributions. This is principally due to the predominate influence of O<sub>2</sub> absorption in determining the energy dependence of the FUV auroral emission. Changes in ratios of FUV emissions as a function of characteristic energy are much larger than those due to changes in energy distribution. Consequently, the uncertainties associated with the energy distribution are not large enough to significantly affect the characteristic energy determination.

The combined auroral and FLIP models allow simultaneous modeling of the EUV and auroral source functions. We modeled typical aurora with concurrent dayglow emissions as a function of solar zenith angle, solar activity levels, total electron energy flux, and incident characteristic energy. Figure 11 shows modeled auroral and dayglow emissions for O I (1356 Å) and LBH (1464 Å). The ratio of auroral to dayglow emissions was found to be a strong function of solar zenith angle because of the dayglow dependence on solar zenith angle. We found that the airglow can be quite intense relative to auroral emissions. Indeed, under certain

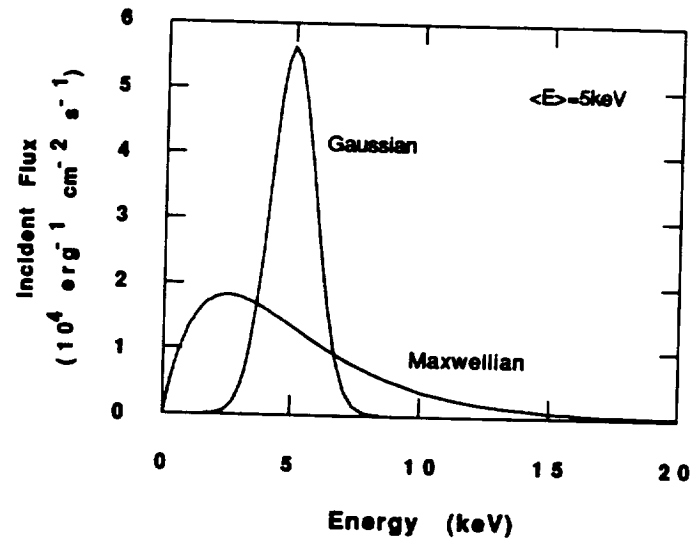
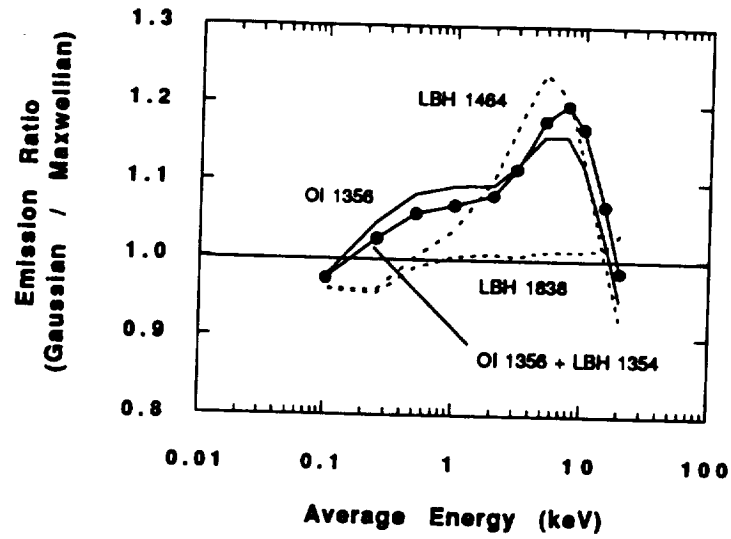


Figure 8. The top panel gives the ratio of column emissions from two energy distributions: a Gaussian and an Maxwellian (bottom panel). Both energy distributions have the same average energy and total flux.

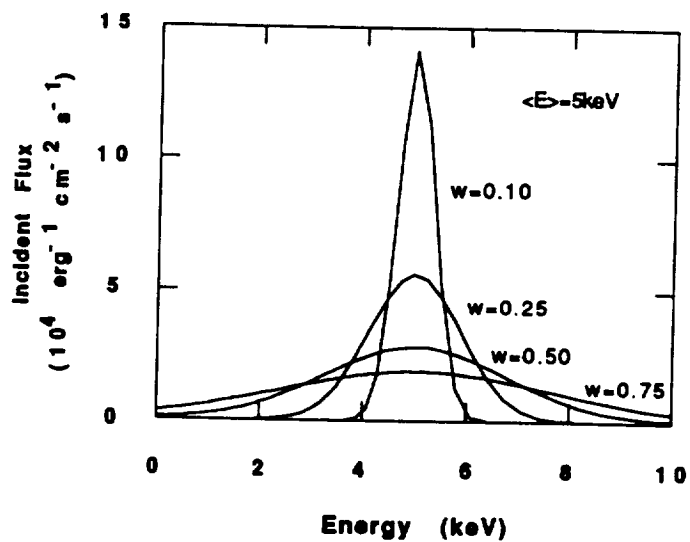
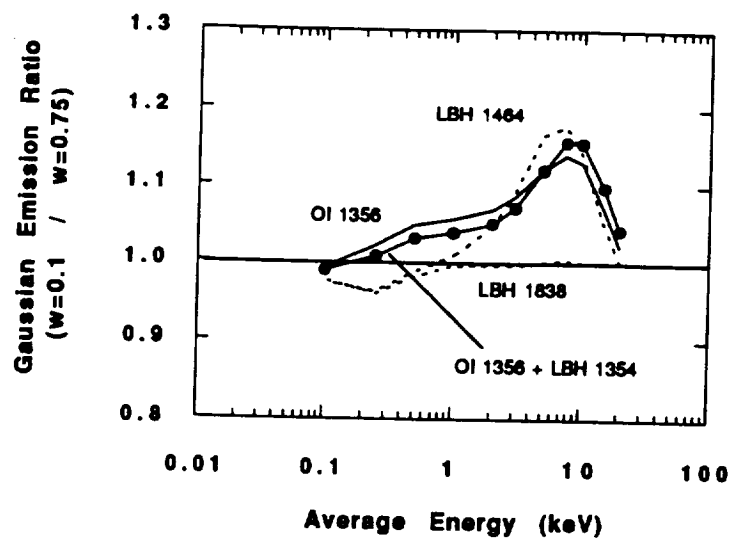


Figure 9. Same as previous figure, except for Gaussian distributions of varying width. Both energy distributions have the same average energy and total flux.

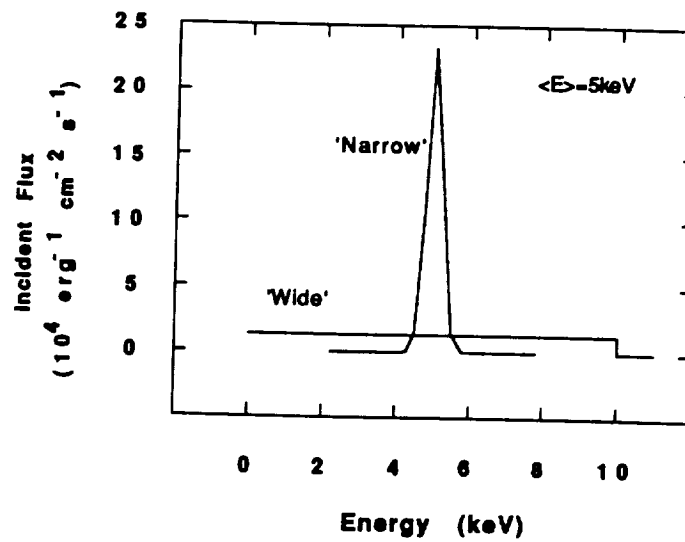
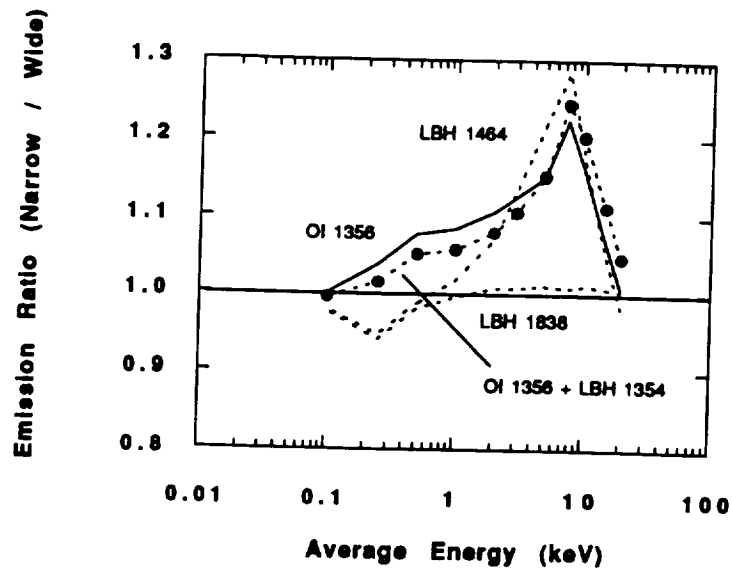


Figure 10. Same as previous two figures except for two arbitrary energy distributions. Both energy distributions have the same average energy and total flux.



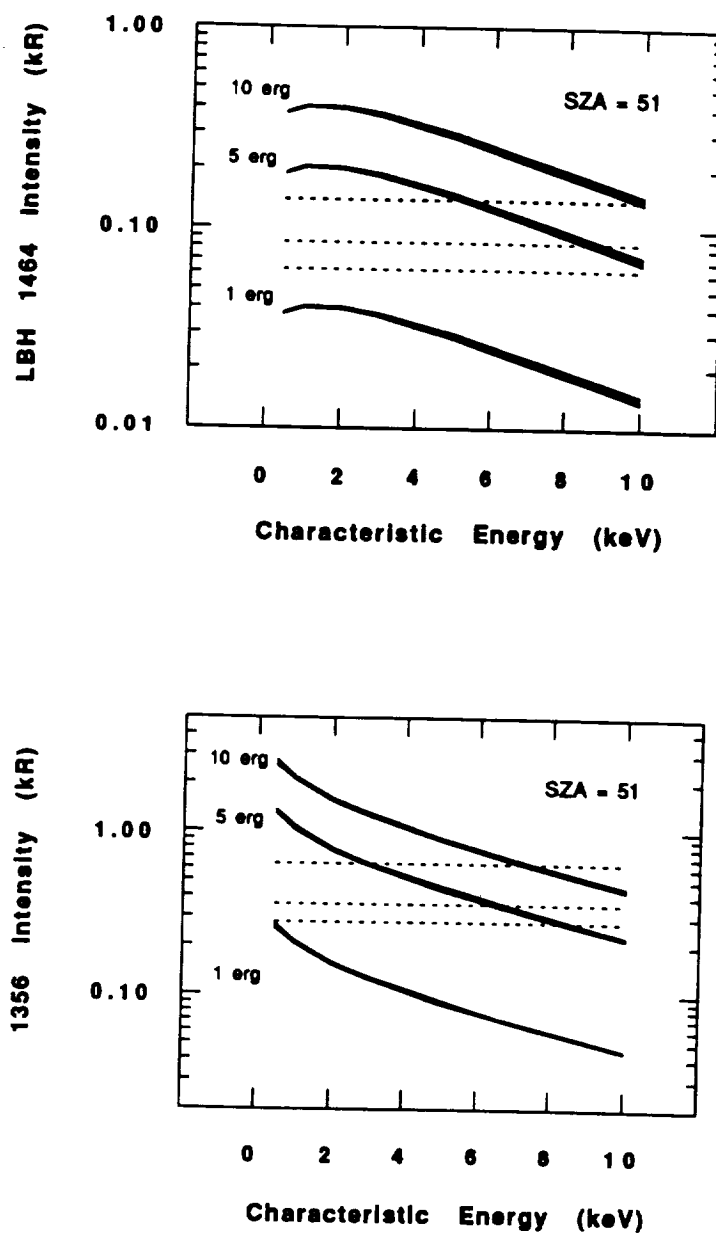


Figure 11. Simultaneously modeled auroral emissions with underlying airglow. Solar activity is varied by changing the F107 and Ap indices.

conditions (energy flux =  $1 \text{ erg cm}^{-2} \text{ s}^{-1}$  and solar zenith angle = 50 degrees) the dayglow will be the limiting factor in the detection of weak auroras.

### Auroral Conductances

The combination of the FLIP and auroral codes also allows the calculation of ionospheric conductances due to auroral precipitation. Knowledge of ionospheric conductivities is central to an understanding of the coupled nature of the ionosphere, thermosphere, and magnetosphere. This is reflected in models of ionospheric electrodynamics and convection requiring conductance distributions. Considerable effort has been directed toward modeling ionospheric conductances from EUV solar illumination, nocturnal sources, and auroral precipitation.

A key to remote determination of auroral conductances by optical methods is the ability to characterize the incident auroral flux. Since we have demonstrated the resultant column intensities are relatively insensitive to choice of energy distribution [Germany *et al.*, 1994], the principal task is to estimate the energy flux and characteristic energy.

Initial results of our conductance modeling were presented at the 1991 Fall meeting of the AGU. An abstract of that presentation is included in Appendix F. In addition, we have submitted a paper for publication discussing our use of LBH emissions to determine auroral conductances. This paper is currently in review; a preprint is included in Appendix G. The modeling study presented in the paper is a continuation of our previous examinations of the utility of LBH emission ratios as remote diagnostics of auroral processes. In this work, we examined the viability of using LBH emission ratios to infer auroral conductances and to quantify the strengths and weaknesses of this technique. To our knowledge, this is the first time the LBH emission ratio has been used to infer auroral conductances. We demonstrated that determinations of average energy and energy flux from a single measurement of two LBH emissions may be used to estimate column-integrated ionospheric conductances. Figure 12 shows modeled ionospheric conductances as a function of the ratio of two LBH emissions. We have examined changes in activity levels by varying the F107 and Ap indices in our models.

Conductances are directly proportional to the corresponding ionospheric electron densities. We calculate conductances using the densities, temperatures, and magnetic field strengths provided by the FLIP model. The dependence of the determined conductivities on incident average energy, total energy flux, and changes in solar and magnetic activity levels was examined. We showed that, for energies above 5 keV, auroral conductances may be scaled by the square root of the incident energy flux with errors less than about 20%. For lower energies, however, the scaling may deviate significantly from a power of 0.5. We provided appropriate scaling factors as a function of average energy. We also noted that the choice of either a Gaussian or Maxwellian distribution can significantly affect low-energy (<1 keV) conductance calculations (Figure 13).

Finally, we quantified the conditions under which the mean energy of a Gaussian energy distribution may differ significantly from the characteristic energy. It is common to state that the mean energy of a Gaussian energy distribution is its central, or characteristic, energy. Since energy is constrained to be non-negative, however, the distribution may be truncated at zero energy. If so, the distribution will be assymetric and the mean energy will be larger than the

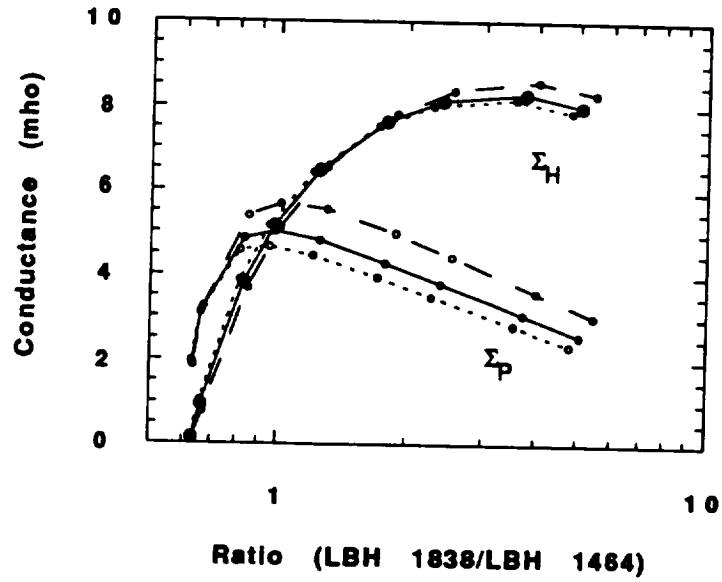


Figure 12. Ionospheric conductances as a function of the FUV LBH emission ratio. Solar activity is varied by changing the F107 and  $A_p$  indices.

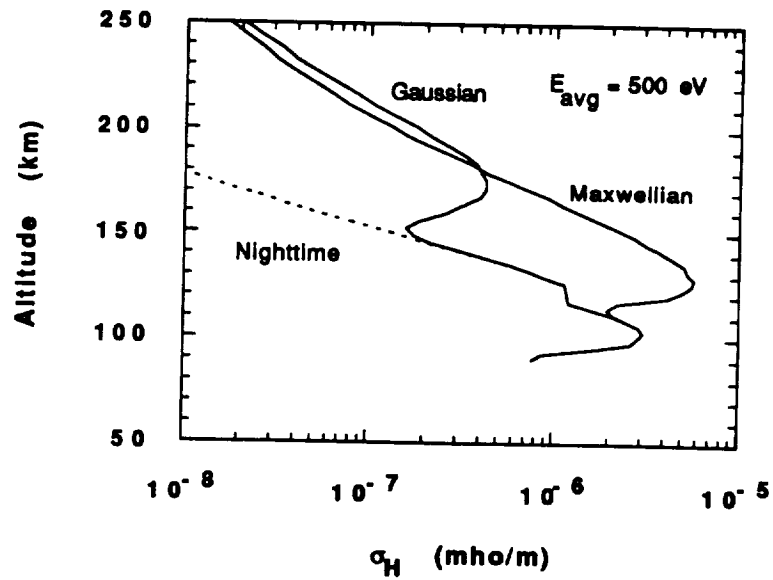


Figure 13. The choice of energy distribution can affect the modeled ionospheric conductivities. Note that the conductivity due to nighttime sources (starlight and reflected EUV) can exceed that from auroral sources.

characteristic energy. The approximation of the mean energy by the characteristic energy fails for energy distributions that are very wide compared with the central energy. The quantitative meaning of the phrase ‘very wide’ is given in the preprint contained in Appendix G.

### 1356 Å from O<sub>2</sub> Dissociative Excitation

In addition to the combination of the auroral and FLIP models, we’ve modified the auroral code to include an additional source of auroral 1356 Å emission. Most models, including our previous codes, have only considered a single source of O(5S) 1356 Å emission, namely electron impact excitation of O. There is, however, an additional potential source of 1356 Å emission, the dissociative excitation of molecular oxygen by electron impact. Dissociative excitation of O<sub>2</sub> by electrons is a significant source of O I 7774 Å emission for hard auroral spectra [Strickland, *et al.*, 1989]. We could reasonably assume that the same mechanism may also be important in the production of auroral 1356 Å emission. Dissociative excitation cross sections for 1356 Å have been reported [Wells *et al.*, 1971] but these have not generally been included in auroral codes.

Based on our initial modeling, we estimated factor of two changes in auroral 1356 Å column intensities due to this additional source. Our initial work, however, failed to account for subsequent revisions of calibration standards. As a consequence of these revisions, the 1356 Å column enhancements due to the additional excitation source are about 15% at 20 keV incident energy. The cross section picture is somewhat unclear and is detailed below.

As noted above, the cross section for the production of 1356 Å emission by electron impact of O<sub>2</sub> has been revised since its initial estimate. Ajello [1971] measured the relative cross section for 1356 Å emission from electron excitation of O<sub>2</sub>, estimating a lower limit of  $1.65 \times 10^{-18} \text{ cm}^2$  for the peak cross section at 100 eV. Central to this determination was the assumption of thermal velocity distributions for the dissociation fragments and the use of the radiative lifetime of the O(5S) state (565 μs) reported by Garstang [1961]. Freund [1971] measured relative 1356 Å emission functions and, along with Borst and Zipf [1971], observed non-thermal velocity distributions for O(5S) by time-of-flight (TOF) methods. Based on these studies, Wells *et al.* [1971] subsequently used a radiative field-of-view analysis to combine the work of Ajello [1971] and Freund [1971] and estimated a peak value of  $7 \times 10^{-18} \text{ cm}^2 \pm 50\%$  at 100 eV. They then renormalized the Ajello [1971] and Freund [1971] relative cross sections to this value.

The radiative lifetime of the O(5S) state was later measured and revised downward by about a factor of 3 [Johnson, 1972; Wells and Zipf, 1972; Wells and Zipf, 1974]. The 1356 Å peak cross section should therefore be revised downward by the same amount. Using the latest value of Wells and Zipf [1974] we estimate the peak cross section at 100 eV to be  $2.1 \times 10^{-18} \text{ cm}^2$ .

We note that none of the lifetime determinations [Johnson, 1972; Wells and Zipf, 1972; Wells and Zipf, 1974], the TOF studies [Freund, 1971; Borst and Zipf, 1971], or the analysis of Wells *et al.* [1971] were dependent on the Mumma and Zipf [1971] Lyman-alpha calibration benchmark. Ajello [1971] did employ a similar calibration, but it was independent of that of Mumma and Zipf [1971]. Hence subsequent revision of this benchmark [Shemansky *et al.*,

1985; Van Zyl *et al.*, 1985; Ajello *et al.*, 1988; Ajello *et al.*, 1991] should not have affected the 1356 Å dissociative emission cross section.

There appear to have been no recent measurements of the cross section. Though we have found no references to additional work beyond that discussed above, there are some conflicting references. Both Itakawa *et al.* [1989] and Ajello and Franklin [1985] reference the work of Wells *et al.* [1971] without mentioning the later lifetime revisions. On the other hand, Erdman and Zipf [1987] reference the lifetime revisions and then suggest an additional revision due to changes in the Lyman-alpha calibration benchmark. As noted above, we feel this is not necessary.

Clearly the 1356 Å dissociative cross section could benefit from additional study. Regardless of the value used, any dissociative emission cross section that is an appreciable fraction of the atomic cross section may contribute substantial 1356 Å emission due to the broad nature of its excitation function. This is the basis for our modeling of the effects of this additional source, using the cross sections of Wells *et al.* [1971] revised to reflect the lifetime determination of Wells and Zipf [1974].

## UVI Workshops

The modeling task included support for an Ultraviolet Imager (UVI) science working group meeting in the second and third years of support to enable prelaunch planning and to gauge science team requirements. It readily became apparent, however, that there were several issues that needed immediate discussion by the group. Therefore, the first UVI workshop was held on 15 & 16 August 1990 in Park City, Utah. The attendees included nationally prominent scientists in the fields of ionospheric and magnetospheric physics and chemistry and are listed in Table 3 along with the meeting's agenda. A major focus of the workshop was the mission science planning and the specific science requirements of each participant for the UVI instrument. The workshop was deliberately informal, with each participant giving presentations about topics of interest to them.

Agenda	
August 15, 1990	August 16, 1990
Introduction	Discussion of Analysis Tools
Instrument Observing Sequences	Discussion of Signal Extraction
Review of Science Objectives	Revised Data Analysis Plan
	Summary

Attendees	
Dr. Joe Ajello	Jet Propulsion Laboratory
Dr. Ken Clark	University of Washington
Dr. Bob Clauer	University of Michigan
Dr. Glynn Germany	University of Alabama in Huntsville
Dr. George Parks	University of Washington
Dr. Jim Spann	NASA/MSFC

Dr. Doug Torr	University of Alabama in Huntsville
Dr. Marsha Torr	NASA/MSFC

Table 3. Attendees and agenda of the 1990 UVI workshop held in Park City, Utah.

The second Ultraviolet Imager (UVI) workshop was held on August 1,2 1991 in Salt Lake City, Utah. The second workshop built on the progress of the first meeting and allowed each of the attendees to participate in the mission science planning and to address their specific science requirements for the UVI instrument. A major focus of the workshop was a review of available thermospheric/ionospheric modeling and image analysis techniques. The second workshop participants and agenda are given in Table 4.

Agenda	
August 1, 1991	August 2, 1991
Goals for Auroral Imaging	Program Status and Introduction
VUV Calibration Source	Automated Auroral Image Analysis
Improved Neutral Wind Modeling	Extraction of Parameters from Images
Summary	Update on Data Analysis
	Auroral Measurements and Models

Attendees	
Dr. Joe Ajello	Jet Propulsion Laboratory
Dr. Keith Cole	La Trobe University, Australia
Dr. Ken Clark	University of Washington
Dr. Glynn Germany	University of Alabama in Huntsville
Dr. Phil Richards	University of Alabama in Huntsville
Dr. Ramin Samadani	Stanford University
Dr. Stan Solomon	University of Colorado
Dr. Doug Torr	University of Alabama in Huntsville
Dr. Marsha Torr	NASA/MSFC

Table 4. Attendees and agenda of the 1991 UVI workshop in Salt Lake City, Utah.

The planning and coordination of both meetings was the responsibility of Dr. Germany. His responsibilities included arrangement of meeting facilities, communication with the science team members, and preparation of post workshop mailings. In addition, Dr. Germany participated in the workshop discussions and gave presentations at both meetings.

## REFERENCES

- Ajello, J. M., Dissociative excitation of O<sub>2</sub> in the vacuum ultraviolet by electron impact, *J. Chem. Phys.*, **55**, 3156, 1971.
- Ajello, J. M., and B. Franklin, A study of the extreme ultraviolet spectrum of O<sub>2</sub> by electron impact, *J. Chem. Phys.*, **82**, 2519, 1985.
- Ajello, J. M., and D. E. Shemansky, A reexamination of important N<sub>2</sub> cross sections by electron impact with application to the dayglow: The Lyman-Birge-Hopfield band system and N I (1119.99 nm), *J. Geophys. Res.*, **90**, 9845, 1985.
- Borst, W. L., and E. C. Zipf, Energy spectra of metastable oxygen atoms produced by electron-impact dissociation of O<sub>2</sub>, *Phys. Rev.*, **A 4**, 153, 1971.
- Erdman, P. W., and E. C. Zipf, Excitation of the OI(3s 5S0-3p 5P; 7774Å) multiplet by electron impact on O<sub>2</sub>, *J. Chem. Phys.*, **87**, 4540, 1987.
- Freund, R. S., Dissociation by electron impact of oxygen into metastable quintet and long-lived high-rydberg atoms, *J. Chem. Phys.*, **54**, 3125, 1971.
- Garstang, R. H., Mutual magnetic interactions and oscillator strengths in the first spectrum of oxygen, *Proc. Cambridge Philos. Soc.*, **57**, 115, 1961.
- Germany, G. A., M. R. Torr, D. G. Torr, and P. G. Richards, Use of FUV auroral emissions as diagnostic indicators, *J. Geophys. Res.*, **99**, 383, 1994.
- Germany, G. A., M. R. Torr, P. G. Richards, and D. G. Torr, The dependence of modeled OI 1356 and N<sub>2</sub> Lyman Birge Hopfield auroral emissions on the neutral atmosphere, *J. Geophys. Res.*, **95**, 7725, 1990.
- Grillot, Patrick N. and William J. Rosenberg, Proton radiation damage in optical filter glass, *Appl. Opt.* **28**, 4473, 1989.
- Hass, G. and W. R. Hunter, Laboratory experiments to study surface contamination and degradation of optical coatings and materials in simulated space environments, *Appl. Opt.* **9**, 2101, 1970.
- Heath, Donald-F. and Paul A. Sacher, Effects of a simulated high-energy space environment on the ultraviolet transmittance of optical materials between 1050 Å and 3000 Å, *Appl. Opt.* **5**, 937, 1966.
- Itikawa, Y., A. Ichimura, K. Onda, K. Sakimoto, and K. Takayanagi, Y. Hatano, M. Hayashi, H. Nishimura, and S. Tsurubuchi, Cross sections for collisions of electrons and photons with oxygen molecules, *J. Phys. Chem. Ref. Data*, **18**, 23, 1989.
- Johnson, C. E., Lifetime of the 2p3 3s5S metastable state of oxygen, *Phys. Rev.*, **A 5**, 2688, 1972.
- Mumma, M. J., and E. C. Zipf, Dissociative excitation of vacuum ultraviolet emission features by electron impact on molecular gases. I. H<sub>2</sub> and O<sub>2</sub>, *J. Chem. Phys.*, **55**, 1661, 1971.
- Nicoletta, C. A. and A. G. Eubanks, Effect of simulated space radiation on selected optical materials, *Appl. Opt.* **11**, 1365, 1972.
- Pellicori, S. F., E. E. Russell, and L. A. Watts, Radiation induced transmission loss in optical materials, *Appl. Opt.* **18**, 2618, 1979.
- Rees, M. H., and D. Luckey, Auroral electron energy derived from ratio of spectroscopic emissions 1. Model computations, *J. Geophys. Res.*, **79**, 5181, 1974.

- Reft, C. S., J. Becher, and R. L. Kernell, Proton-induced degradation of VUV transmission of LiF and MgF<sub>2</sub>, *Appl. Opt.* **19**, 4156, 1980.
- Richards, P. G., and D. G. Torr, Auroral modeling of the 3371 Å emission rate: Dependence on characteristic electron energy, *J. Geophys. Res.*, **95**, 10337, 1990.
- Shemansky, D. E., J. M. Ajello, D. T. Hall, Electron impact excitation of H<sub>2</sub>: Rydberg band systems and the benchmark dissociative cross section for H Lyman-alpha, *Ap. J.*, **296**, 765, 1985.
- Sojka, J. J., C. E. Rasmussen, and R. W. Schunk, An interplanetary magnetic field dependent model of the ionospheric convection electric field, *J. Geophys. Res.*, **91**, 11281, 1986.
- Strickland, D. J., J. R. Jasperse, and J. A. Whalen, Dependence of auroral FUV emissions on the incident electron spectrum and neutral atmosphere, *J. Geophys. Res.*, **88**, 8051, 1983.
- Strickland, D. J., R. R. Meier, J. H. Hecht, and A. B. Christensen, Deducing composition and incident electron spectra from ground-based auroral optical measurements: Theory and model results, *J. Geophys. Res.*, **94**, 13527, 1989.
- Torr, M. R. and D. G. Torr, The role of metastable species in the thermosphere, *Rev. Geophys.*, **20**, 91, 1982.
- Torr, M. R., Neutral and ion chemistry and solar fluxes, *J. Geomag. and Geoelectricity*, **35**, 131, 1983.
- Torr, D. G., The photochemistry of the upper atmosphere, in *The Photochemistry of Atmospheres*, edited by J. S. Levine, pp. 165-278, Academic, San Diego, Calif., 1985.
- Torr, M. R., D. G. Torr, P. G. Richards, and S. P. Yung, Mid- and low-latitude model of thermospheric emissions 1. O+(2P) 7320 Å and N<sub>2</sub> (2P) 3371 Å, *J. Geophys. Res.*, **95**, 21147, 1990.
- Van Zyl, B., M. W. Gealy, and H. Neumann, Excitation of low-energy H atoms in H + Ne collisions, *Phys. Rev. A* **31**, 2922, 1985.
- Wells, W. C., and E. C. Zipf, Absolute cross sections for the dissociative excitation of OI(5S<sub>0</sub>) and its radiative lifetime, *EOS Trans. AGU*, **53**, 459, 1972.
- Wells, W. C., and E. C. Zipf, Lifetime of the metastable 5S<sub>0</sub> state of atomic oxygen, *Phys. Rev.*, **A 9**, 568, 1974.
- Wells, W. C., W. L. Borst, and E. C. Zipf, Absolute cross section for the production of O(5S) by electron impact dissociation of O<sub>2</sub>, *Chem. Phys. Lett.*, **12**, 288, 1971.
- Young, E. R., P. G. Richards, and D. G. Torr, A flux preserving method of coupling first and second order equations to simulate the flow of plasma between the protonosphere and ionosphere, *J. Comp. Phys.*, **38**, 141, 1980.



**APPENDIX A**

**“Laboratory Facility for Simulation of  
Vehicle-Environment Interactions”**

**Vehicle-Environment Interactions Conference  
Applied Physics Laboratory  
Laurel, Maryland  
March 11-13, 1991**

## **Laboratory Facility for Simulation of Vehicle-Environment Interactions**

Charles E. Keffer  
University of Alabama in Huntsville  
Physics Department  
Huntsville, AL 35899

Marsha R. Torr  
NASA Marshall Space Flight Center  
Space Science Laboratory  
Huntsville, AL 35812

### **ABSTRACT**

A facility for simulation and study of interactions between a spacecraft in low Earth orbit (LEO) and its ambient environment is described. The facility is composed of a crossed beam apparatus with a rotatable mass spectrometer detector. It can be used for a wide variety of vehicle interaction studies including both gas phase and gas-surface interactions. Measurements of differential scattering cross sections, surface scattering phenomena, and spacecraft glow are representative examples. A key element in the facility is a laser-induced discharge energetic oxygen atom source for simulation of the ambient vehicle environment. Measurements of important characteristics of the oxygen atom source, including velocity and beam composition, are presented. Performance of differential scattering cross section measurements is evaluated using low angle scattering from thermal energy collisions between beams of oxygen and nitrogen molecules.

### **INTRODUCTION**

Spacecraft in low Earth orbit (200-700 km) are exposed to an intense flux of atomic and molecular species from the atmosphere. At these altitudes the major constituent of the atmosphere is atomic oxygen which is created by solar UV photodissociation of molecular oxygen. Typical orbital velocities of 8 km/sec produce an atomic oxygen kinetic energy relative to the spacecraft of nominally 5 eV. The density of atomic oxygen varies with the amount of solar activity, but an average value for 250 km is about  $10^9$  atoms/cm<sup>3</sup>. The flux of atomic oxygen impinging on spacecraft surfaces under these conditions is thus approximately  $10^{15}$  atoms/cm<sup>2</sup>/sec. This environment is known to cause a variety of phenomena including severe surface erosion of polymers and some metals as well as induced optical emissions in the ultraviolet, visible, and infrared portions of the electromagnetic spectrum [Bareiss et al., 1987].

Since the discovery of these effects several years ago, a significant effort has been made to study them. A combination of spacecraft glow data [see, e.g., Torr et al., 1977; Banks et al., 1983; Mende et al., 1988] and several recent laboratory investigations [Arnold and Coleman, 1988; Caledonia et al., 1990; Holtzclaw et al., 1990; Orient et al.,

1990] has led to the development of a preliminary data base for the spacecraft glow phenomena. However, very little is yet known about such fundamental atomic and molecular parameters as scattering, excitation, or ionization cross sections for 5 eV oxygen colliding with other species. Mechanisms for the spacecraft glow phenomena and the surface chemistry processes [Kofsky and Barrett 1986] are just beginning to be understood with much still remaining to be learned.

An improved understanding of these atomic oxygen effects on orbiting spacecraft is important to the success of Space Station Freedom and to future Space Shuttle missions with payloads which are sensitive to the induced environment around the vehicle. Atomic oxygen also plays a fundamental role in the chemistry of the upper atmosphere and in high temperature combustion reactions.

## FACILITY DESCRIPTION

Figure 1 shows a schematic diagram of the facility. The basic design consists of two orthogonal fixed beam sources and an in-plane quadrupole mass spectrometer detector which is rotatable around the collision region of the two gas beams [Lee et al., 1969]. The beam sources are pulsed to minimize pumping requirements and to optimize the energetic oxygen atom source in one of the beams. The configuration shown illustrates the setup for making differential scattering cross section measurements. For surface scattering measurements only one beam valve is used and the surface material is placed at the center of rotation of the mass spectrometer detector.

### Vacuum System

The cylindrical vacuum chamber is fabricated from 304L stainless steel with an inside diameter of 47" and height of 25.5" (see Figure 2). The walls are made thick to limit distortion and misalignment due to atmospheric pressure. The lid, which is removable to allow access to the interior of the chamber, is 1.5" thick, the bottom is 1" thick and the cylinder wall is 0.5" thick. The main chamber is pumped by a 3000 l/sec cryopump which removes essentially all of the gas from each pulse prior to the arrival of the next pulse at the usual 0.5 Hz repetition rate of the valves.

The pulsed valves are in differentially pumped chambers each evacuated by a 1000 l/sec turbomolecular pump. A 1 mm diameter beam skimmer separates each pulsed valve chamber from the main chamber and collimates the gas beam. Flexible bellows in the pulsed valve chambers, together with horizontal and vertical adjusting assemblies, allow the gas beams to be aligned so as to collide at the center of rotation of the mass spectrometer detector. Precision bearings and shafts in the adjusting assemblies allow an alignment accuracy of  $\pm .005"$ . Pressure in the pulsed valve chambers is kept below  $10^{-4}$  Torr during operation to limit loss in beam intensity due to scattering.

The mass spectrometer is mounted inside of a housing which is differentially pumped by a 230 l/sec ion pump. Interchangeable apertures on the front of the housing

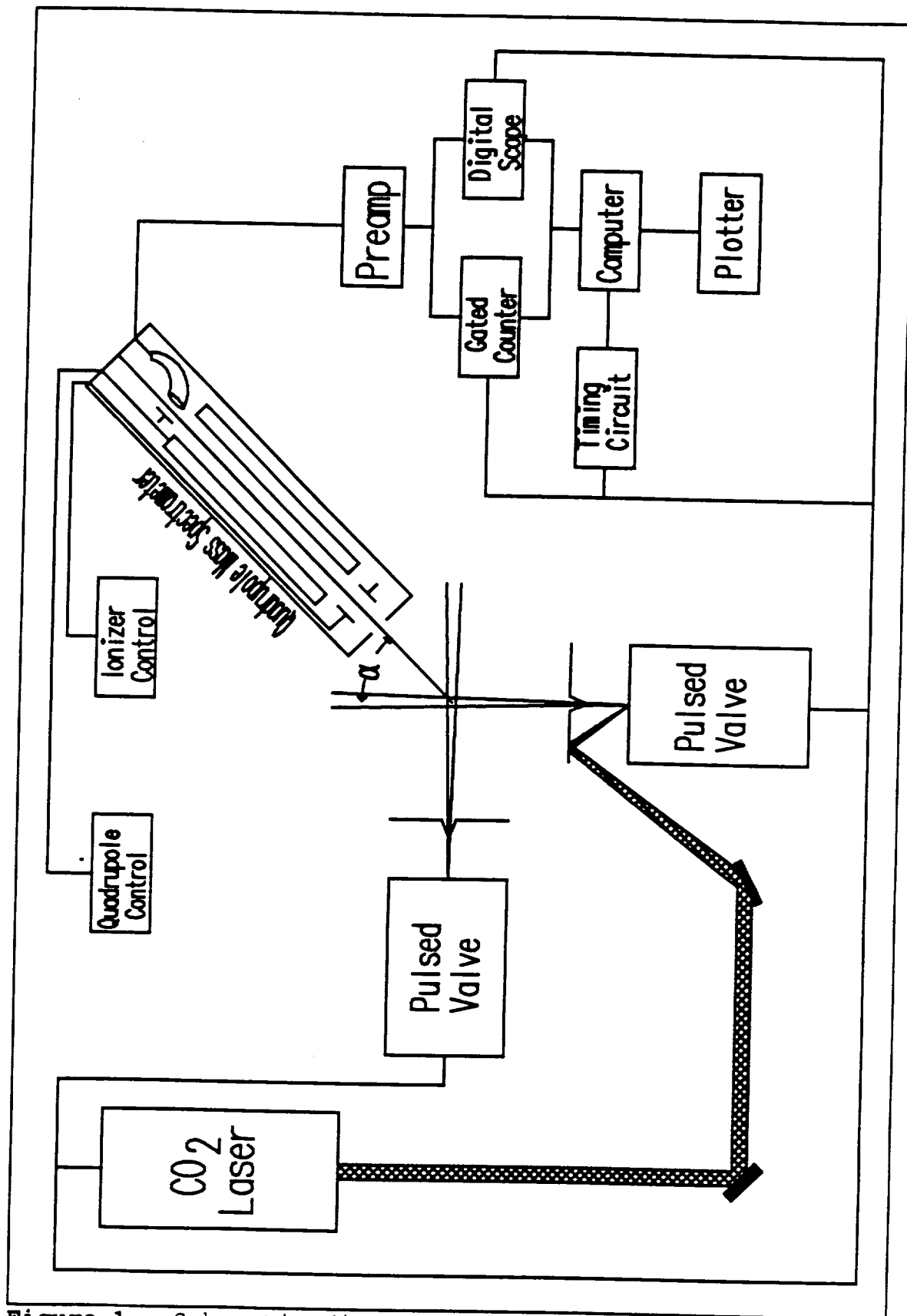


Figure 1. Schematic diagram of cross section facility.

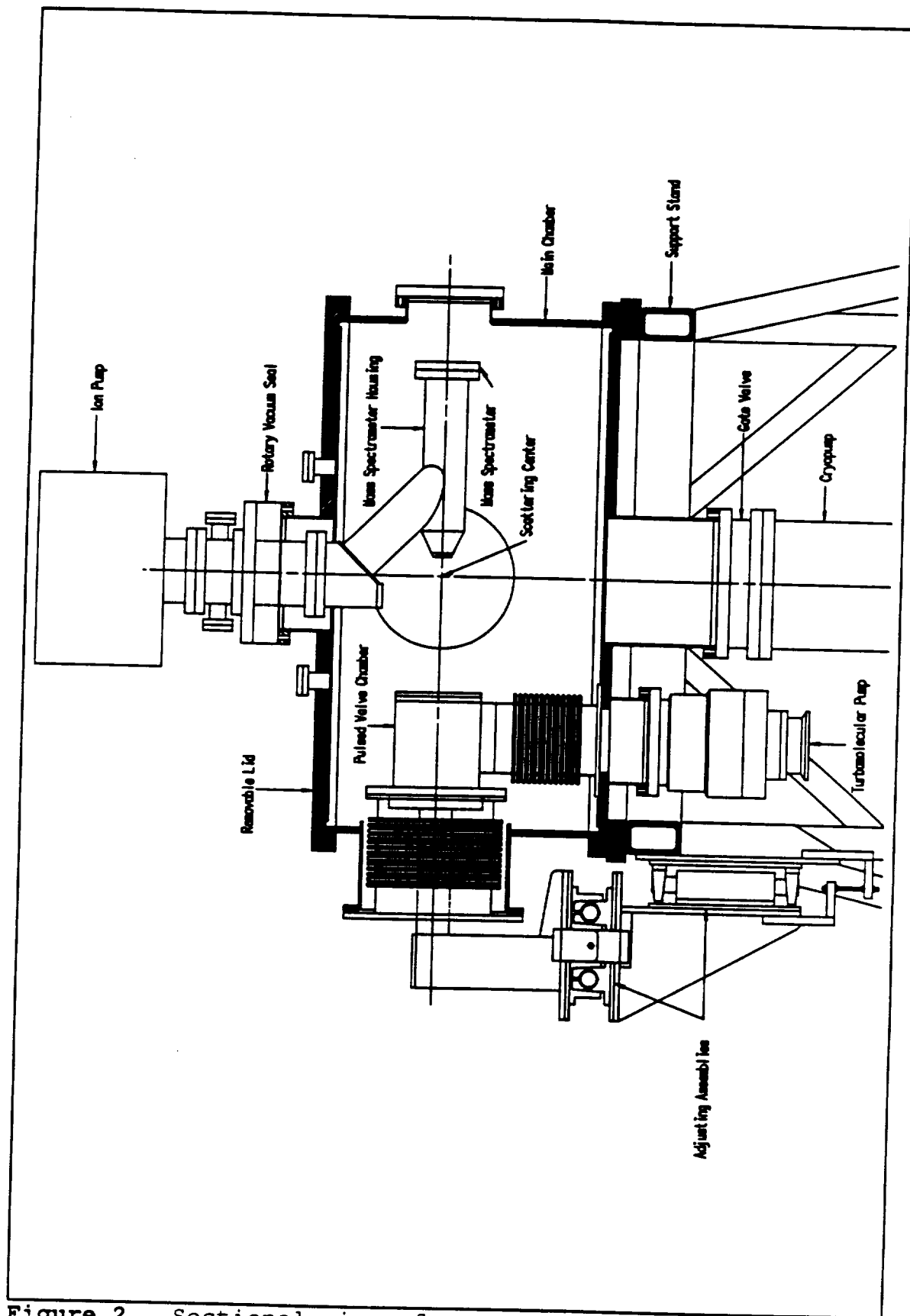


Figure 2. Sectional view of vacuum chamber.

and the entrance to the mass spectrometer ionizer limit the acceptance angle of the mass spectrometer to the region of overlap of the two gas beams. The mass spectrometer housing is suspended from a rotary vacuum seal which is differentially pumped by a small mechanical pump and a small ion pump. This arrangement allows the mass spectrometer to be rotated about the scattering center through approximately 200 degrees without significantly effecting the pressure in the main chamber or in the mass spectrometer housing. Base pressure in the mass spectrometer housing is  $10^{-9}$  Torr. No measurable effect on the pressure in the mass spectrometer occurs from operation of the pulsed valves.

### Atomic Oxygen Source

Atomic oxygen is formed in one of the beam sources by pulsed laser-induced breakdown of pure molecular oxygen in the manner developed and described by Caledonia et al., 1987. A sectional view of the atomic oxygen source is shown in Figure 3. A pulsed valve in the center of the figure introduces a short pulse of molecular oxygen into a conical expansion nozzle. An approximately 8 J CO<sub>2</sub> laser beam passes through a 1 meter focal length BaF<sub>2</sub> lens shown at the lower left of the figure. The CO<sub>2</sub> laser beam then passes through an AR coated ZnSe window which separates the vacuum in the pulsed valve chamber from atmospheric pressure. The beam is focussed to about 1 cm<sup>2</sup> on a gold coated nickel copper mirror. A smaller spot size results in an energy density on the mirror which can cause significant damage to the mirror coating. The 50 cm radius of curvature of the gold coated mirror focusses the CO<sub>2</sub> laser beam to about 1 mm<sup>2</sup> near the orifice of the valve. A direct hit on the valve orifice is avoided since this damages the o-ring tip which seals the valve closed between pulses. The energy density in the focussed laser beam is sufficient to dissociate the molecular oxygen creating a high temperature plasma near the throat of the nozzle. The hot plasma accelerates down the expansion nozzle as a blast wave dissociating and accelerating most of the remaining molecular oxygen. Fast oxygen atoms exiting the nozzle are collimated by a 1 mm diameter skimmer as they enter the main vacuum chamber. Residual gas deflected by the skimmer is removed from the pulsed valve chamber by the turbomolecular pump. A small fraction of the fast gas pulse is composed of ions. These are readily removed from the pulse by deflection plates in the main vacuum chamber. These deflection plates are spaced 1 cm apart and biased with a few hundred volts potential difference.

## FACILITY PERFORMANCE

### Differential Scattering

Classical scattering theory predicts that an intermolecular potential of the form

$$V(r) \propto -1/r^6 \quad (1),$$

where  $r$  is the intermolecular distance, should have a low-angle differential scattering cross section equal to

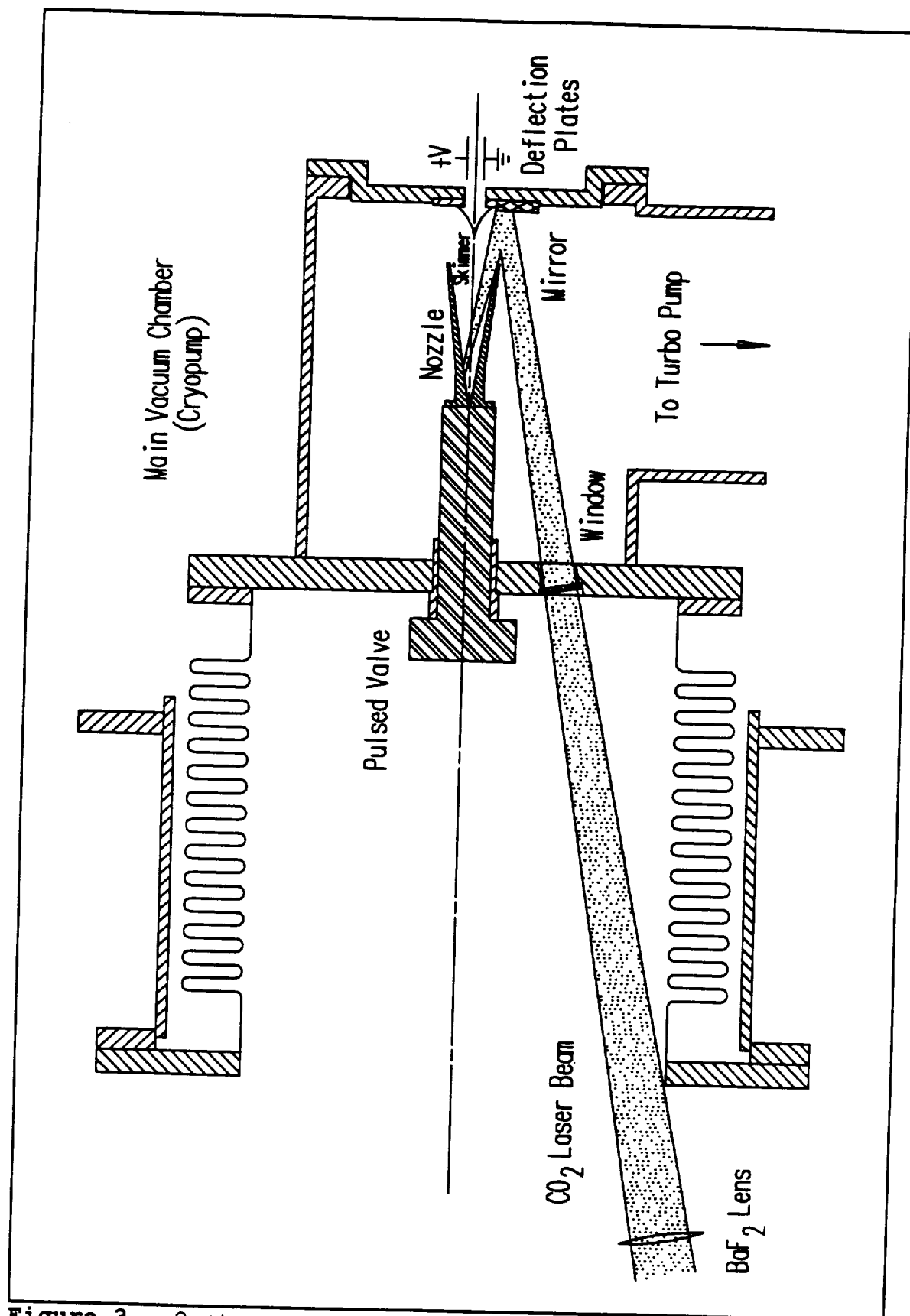


Figure 3. O atom source sectional view.

$$I(\theta) \propto \theta^{-7/3} \quad (2),$$

where  $\theta$  is the center-of-mass scattering angle [Bernstein, 1964]. This functional form of the potential is typical of the long range attractive van der Waals forces between atoms and molecules. Experimental results presented as log-log plots of differential scattering cross section vs center-of-mass angle have confirmed this predicted behavior in the range of center-of-mass angles from roughly 1 to 10 degrees for a large number of collision partners [Bernstein, 1964]. We have used this simple relationship to validate the capability of our facility for making differential scattering cross section measurements without serious systematic errors. Collisions between beams of thermal energy oxygen and nitrogen molecules have been used as a test system. Several sets of data were taken for center-of-mass angles less than 10 degrees. Transformation of the data from the laboratory to the center of mass coordinate system was accomplished assuming the approximation of elastic scattering of monoenergetic beams colliding at  $90^\circ$  with no divergence and scattering detected in the plane of the two beams [Bernstein, 1964]. Average values for the relative differential scattering cross section are shown in Table 1.

Table 1. Relative differential scattering cross section for  $O_2 + N_2$  collisions.

Center of Mass Angle (degrees)	Relative Differential Scattering Cross Section (arbitrary units)
$6.4 \pm 0.2$	$26.58 \pm 0.42$
$7.0 \pm 0.2$	$19.91 \pm 0.08$
$7.5 \pm 0.2$	$17.70 \pm 0.42$
$8.0 \pm 0.2$	$14.13 \pm 0.27$
$8.5 \pm 0.2$	$13.21 \pm 0.36$
$9.1 \pm 0.2$	$11.75 \pm 0.14$
$9.6 \pm 0.2$	$10.03 \pm 0.17$

Uncertainties in the angles are due primarily to the positional accuracy of the rotary vacuum seal. Relative differential scattering cross section uncertainties represent 1 standard deviation for each set of data at each angle. A least squares fit to the log of the scattered intensity vs the log of the center-of-mass angle results in an experimental value for the exponent of  $-2.30 \pm .13$ . This is within one standard deviation of the theoretical value and so indicates satisfactory agreement.



## Atomic Oxygen Source

Measurements have been made on the atomic oxygen source to determine the velocity of the atom beam. Figure 4 indicates the type of measurements which have been made. The figure shows three peaks. The first one is due to photons from the oxygen plasma discharge which strike the Channeltron detector of the mass spectrometer while the second peak is due to fast oxygen atoms. The third peak on the shoulder of the oxygen atom peak is due to a small amount of preamp ringing arising from the large, fast rise time O atom signal. The photon peak serves as a time marker since the arrival of the photons at the detector is essentially coincident in time with the formation of the fast atoms. So, the time between the two peaks represents the time of flight for the oxygen atoms. The velocity is thus calculated from the time of flight and the known distance from the valve to mass spectrometer. The average velocity is 6.8 km/sec for the oxygen atom pulse shown in Figure 4. The velocity of the oxygen atoms can be varied by changing the laser intensity or the amount of gas per pulse. A velocity range of 3 to 11 km/sec has been measured for this source.

The fast atom beam composition has also been measured to determine the ratio of oxygen atoms to oxygen molecules and to identify the presence of any impurities in the beam. Mass spectrometer measurements of the beam have been made indicating a range of 80 % to 95 % atoms in the beam. Two competing processes in the mass spectrometer ionizer contribute to an uncertainty in the actual fast atom content of the beam as it is deduced from the measurements. Dissociation of molecular oxygen by the ionizer results in an overestimation of the atom content in the beam. Ten percent dissociation of molecular oxygen is typical in our ionizer. For a beam which is predominately atomic oxygen, this represents a small uncertainty. For example, a beam of 80% O and 20% O<sub>2</sub> would appear as 82% O and 18% O<sub>2</sub> in the mass spectrometer due to the dissociative ionization. On the other hand, recombination of atoms in the mass spectrometer during the duration of the fast pulse results in a loss of atoms in the beam. The degree of recombination in the beam is likely small since there are no metal surfaces in the direct line-of-sight for the oxygen atoms as they enter the mass spectrometer ionizer. However, even if a large amount of recombination in the mass spectrometer does occur the mass spectrometer measurements would represent a lower limit on the percentage of atoms in the beam. So, the fast atom beam is conservatively estimated to be > 80 % atomic oxygen and < 20% molecular oxygen. Some oxygen ions are also present at less than 1 % of the beam. These ions are readily removed from the beam by the deflection plates described above. Impurities at other masses also represent less than 1 % of the beam.

## ACKNOWLEDGEMENTS

This work was supported by NASA Marshall Space Flight Center under Grant No. NAG8-834 to The University of Alabama in Huntsville.

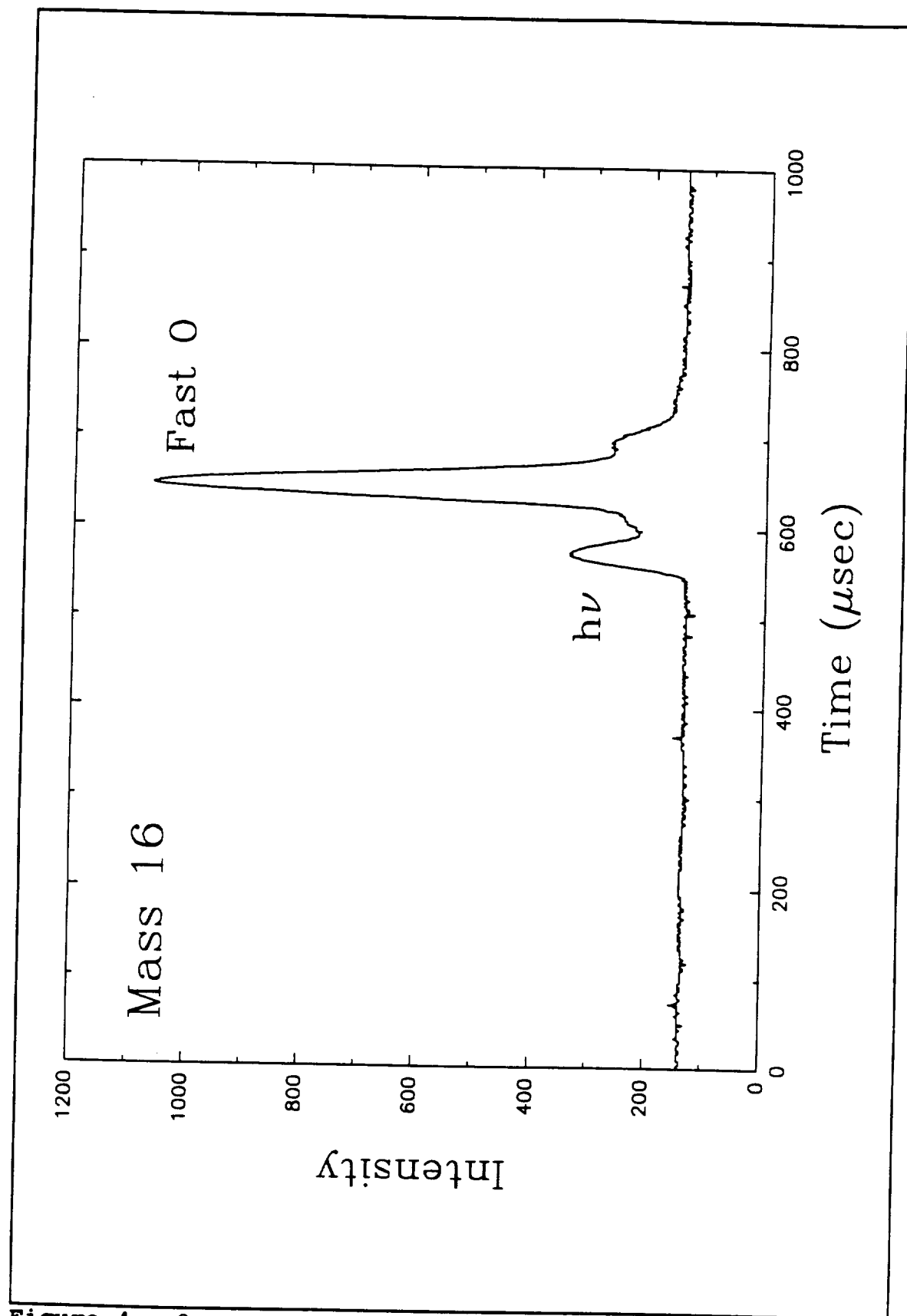


**Figure 4.** Oxygen atom velocity measurement.

## REFERENCES

- Arnold, G. S., and D. J. Coleman, Surface Mediated Radical Recombination Luminescence:  $O + NO + Ni$ , J. Chem. Phys., **88**, 7147-7156, 1988.
- Banks, P. M., P. R. Williamson, W. J. Raitt, Space Shuttle Glow Observations, Geophys. Res. Lett., **10**, 118-121, 1983.
- Bareiss, L. E., R. M. Payton, and H. A. Papazian, Shuttle/Spacelab Contamination Environment and Effects Handbook, NASA Contractor Report 4053, George C. Marshall Space Flight Center, Huntsville, AL, 1987.
- Bernstein, R. B., Molecular Beam Scattering at Thermal Energies, Science, **144**, 141-150, 1964.
- Caledonia, G. E., R. H. Krech, and B. D. Green, A High Flux Source of Energetic Oxygen Atoms for Material Degradation Studies, AIAA J., **25**, 59-63, 1987.
- Caledonia, G. E., K. W. Holtzclaw, B. D. Green, R. H. Krech, A. Leone, and G. R. Swenson, Laboratory Investigation of Shuttle Glow Mechanisms, Geophys. Res. Lett., **17**, 1881-1884, 1990.
- Holtzclaw, K. W., M. E. Fraser, and A. Gelb, Infrared Emission from the Reaction of High-Velocity Atomic Oxygen with Graphite and Polyethylene, J. Geophys. Res., **95**, 4147-4153, 1990.
- Kofsky, I. L., and J. L. Barrett, Spacecraft Glows from Surface-Catalyzed Reactions, Planet. Space Sci., **34**, 665-681, 1986.
- Lee, Y. T., J. D. McDonald, P. R. LeBreton, and D. R. Herschbach, Molecular Beam Reactive Scattering Apparatus with Electron Bombardment Detector, Rev. Sci. Instrum., **40**, 1402-1408, 1969.
- Mende, S. B., G. R. Swenson, and E. J. Llewellyn, Adv. Space Res., **8**, 229, 1988.
- Orient, O. J., A. Chutjian, and E. Murad, Recombination Reactions of 5-eV  $O(^3P)$  Atoms on a  $MgF_2$  Surface, Phys. Rev. A, **41**, 4106-4108, 1990.
- Torr, M. R., P. B. Hays, B. C. Kennedy, and J. C. G. Walker, Intercalibration of Airglow Observatories with the Atmosphere Explorer Satellite, Planet. Space Sci., **25**, 173-184, 1977.

**APPENDIX B**

**Workshop on the Induced Environment of Space Station Freedom  
Huntsville, Alabama  
January 30-31, 1991**

# **Workshop on the Induced Environment of Space Station Freedom**

**Proceedings of a workshop held at  
George C. Marshall Space Flight Center  
Huntsville, Alabama  
January 30-31, 1991**

# **Summary Report on the Workshop on the Induced Environment of Space Station Freedom**

**Huntsville, Alabama, January 30-31, 1991  
prepared by Dr Marsha R. Torr/MSFC**

**Introduction.** A workshop was held in Huntsville on January 30-31, 1991 for the purpose of reviewing the state of knowledge of the likely induced external environment around Space Station Freedom. This workshop was chaired by Dr Marsha R. Torr and was a continuation of an activity coordinated by the Marshall Space Flight Center since 1987 and sponsored by the Office of Space Science and Applications and more recently by the Space Station Utilization Office at Reston. Two previous workshops have been held (one in October 1987 and one in May 1988) with the express purpose of assessing our understanding of the causative mechanisms underlying the various phenomena in the induced environment (glows, ionization, surface effects, gas envelope, etc). Both of the previous meetings led to the publication of NASA Conference Proceedings which document the contributions. As a result of the earlier reviews, a limited number of studies were funded in an attempt to obtain information on certain of the more fundamental processes involved. The activity has also been used to assist NASA Headquarters in assessing the impact of various Station design issues on potential attached payloads. Information gathered applies just as readily to critical Station systems such as the solar arrays.

The purpose of this meeting was to address three questions:

- 1) Where are we in our knowledge of the likely induced environment?
- 2) What progress have we made in the past two years in understanding this environment?
- 3) What areas of study are the most important for the next two years?

Copies of the material presented at the meeting are available.

**Proceedings of Meeting.** The agenda for the meeting is included here as Attachment I. The list of attendees is included as Attachment II. The meeting attendance was intentionally limited to the participants and NASA invitees. Some additional observers attended on a space available basis. The objective was to keep the meeting rather small so as to facilitate a good working environment. As with the previous two workshops, however, it was clear that as word of the meeting got out, the interest in attending was high and we had to turn a relatively large number of people away. This may indicate the desirability of scheduling a wider attendance "tutorial" meeting at some point to serve the purpose of briefing various personnel working on the Station design on the issues that this panel of experts is addressing.

As part of the first question above, reviews were presented of various related activities that have been conducted over the past year, including a rather sizable DOD effort on vehicle glows, and a summary of the early findings from the LDEF program. In addition, presentations were made of the various studies that have been funded by this and other MSFC programs.

Despite the very limited funding that has gone into the effort, the progress that has been made since the 1988 workshop was found to be considerable. This is largely due to the fact that the external Station environment represents a region of most unusual physical processes, including both gas phase and surface phase interactions, so that scientists in fields of appropriate expertise are challenged by the task of understanding the phenomena. A number of facilities have been put in place for the purpose of studying such environments in the laboratory and early results are beginning to emerge. The progress in developing models of the environment has made excellent progress. Almost three years ago we had very little to work with apart from unexplained Shuttle phenomena, and "back-of-the-envelope" projections for Space Station Freedom. Now we are at a point where we have the tools to begin to do believable evaluations.

**Recommendations.** In order to predict the external Station environment, it is necessary that we are able to understand the nature of the processes taking place within it. At present, the state of knowledge is very poor. Over the past three years, with very nominal resources (~\$150K per year), it has been possible to make progress in the field and to set in place important tools which are now available for use in further studies.

At some point we anticipate that the Space Station Freedom will be used for purposes of attaching external payloads. If NASA is to remain a "smart buyer" in this area it is most important that we continue the efforts (albeit at a low level of effort) to understand the environment in which these systems will operate, and what the limitations on them will be. Maintenance of a multidisciplinary pool of expertise, such as is represented by the panels put together for these workshops and study efforts, is a valuable, if not essential, activity.

At present there are several activities that we would recommend for immediate attention. For example, in order to conduct almost any assessment of the external environment, one must first model the gas concentrations surrounding the vehicle. Once this is known, one can proceed to model the induced optical emission and the induced ionization. With these established one can compute the backscatter fluxes, arcing, plasma discharges, optical thresholds, etc. One can optimize the placement of vents, and establish the impact of leaks. However, a fundamental input to models of the neutral gas environment is the gas phase collision cross sections. Those relevant to this problem are essentially unknown. It is important to measure these cross sections in the laboratory and then input them to the models. During a shuttle docking the Station surfaces can become flooded with contaminants. We do not know what the residence times of these contaminants are on the surfaces, and in the induced environment. These lifetimes can be measured in the laboratory and it is recommended that studies be made for key likely species such as water. If attached payloads are initially to be mounted on the JEM, it is important that we try to establish the environment for this location first. Relevant new evidence of synergistic effects is emerging from the LDEF studies. These need to be examined in the light of the Space Station Freedom external environment work. A summary of the specific recommendations made by individual panel members is included here as Attachment III.



**ATTACHMENT I:**

**WORKSHOP on the INDUCED ENVIRONMENT of  
SPACE STATION FREEDOM**

**Radisson Hotel, Huntsville, Alabama**

**January 30-31, 1991**

**Wednesday, January 30, 1991**

8:30AM	Introduction and Objectives of Workshop	M. Torr
8:45AM	Environmental Definition and Assessment Program	D. Brewer
9:15AM	Current Requirements and Plans to Verify These	L. Leger
9:45AM	Status of Planned Investigations Attached to Space Station Freedom	M. Sistilli
10:15AM	BREAK	
10:30AM	Environmental Issues from the Utilization Viewpoint	K. Schaefer
11:00AM	Vehicle Interaction Program at JHU/APL	C. Meng
11:30AM	LUNCH	
1:00PM	Glows, Accomodation and Surface Residence Times	G. Caledonia
1:30PM	Summary of Space Station Grounding Issues	R. Carruth
2:00PM	LDEF: Lessons Learned	convenor: A. Whitaker R. Linton R. Rantanen
3:15PM	BREAK	

**January 30, 1991, continued:**

3:30PM	Overview of Spacecraft Glow	T. Slanger
4:00PM	Summary of JPL Workshop on Modeling Tools	J. Murphy
4:30PM	Discussion	
5:00PM	End of Formal Presentations for the Day	
6:00PM	SPECIAL EVENT AT ALABAMA SPACE AND ROCKET CENTER see attached sheet	

**Thursday, January 31, 1991**

8:30AM	ISEM Space Station Model Update	T. Gordon
9:00AM	Cross Section Work at Rice	K. Smith
9:30AM	Cross Section Work at UAH/MSFC	C. Keffer
10:00AM	BREAK	
10:15AM	Induced Emissions	D. Torr
10:45AM	Atomic Oxygen Studies at PPPL	J. Cuthbertson
11:15AM	Spacecraft Glow Studies and Mechanisms	S. Mende
11:45AM	LUNCH	
1:00PM	Visit to Space Station Mockup	
2:30PM	Surface Temperature Dependent Glow Mechanisms in Space	N. Tolk
3:00PM	What Have We Learned?	
3:30PM	BREAK	
3:45PM	Where do we go from here?	
4:30PM	End of Meeting	

## **ATTACHMENT II:**

### **LIST OF ATTENDEES**

Marsha Torr, Chairperson	NASA\MSFC
Charles Keffer	UAH
Anderson, Jeff	NASA/MSFC
Blanchette, Fred	McDonnell Douglas Space Systems Co.
Brewer, Dana	NASA/HQ
Caledonia, George	Physical Sciences Inc.
Carruth, Ralph	NASA/MSFC
Chappell, Rick	NASA/MSFC
Collier, Jack	NASA/HQ
Crane, Mike	Boeing
Cuthbertson, John	Princeton Plasma Physics Lab
Erlandson, Bob	Applied Physics Lab
Espy, Pat	NASA/MSFC
Feddes, Allan	Boeing
Fichtl, George	NASA/MSFC
Gordon, Tim	Applied Science Technologies
Hefling-Miller, Hilda	Grumman SSPSD
Hwang, Kai-Shen	Grumman SSEIC
Jongward, Gary	S-Cubed
Katz, Ira	S-Cubed
Leifer, Joel	Booz-Allen & Hamilton
Linton, Roger	NASA/MSFC
McCombs, Roger	BA&E
Mende, Steve	Lockheed Palo Alto Research Lab
Melendez, Daniel	NRC
Meng, Ching	Applied Physics Lab
Murphy, Gerry	JPL
Nahra, Henry	NASA/Lewis
Nebolsine, Peter	Physical Sciences Inc.
O'Keefe, Ed	Boeing
Plaster, Teresa	Grumman Space Station Integration
Rantanen, Ray	ROR Enterprises
Schaefer, Kevin	NASA/Reston

Sistilli, Mark  
Slanger, Tom  
Smith, Ken  
Snyder, Dave  
Suggs, Rob  
Taylor, Bill  
Tolk, Norman  
Torr, Doug  
Whitaker, Ann  
Wyman, Pete  
Young, Dave

NASA/HQ  
SRI International  
Rice University  
NASA/Lewis  
Grumman Space Station Integration  
NASA/HQ  
Vanderbilt University  
UAH  
NASA/MSFC  
NASA/HQ  
Grumman

### **ATTACHMENT III:**

**Recommendations Made by Individual Panel Members (in alphabetical order).**

**Brewer(HQ/MSS):**

**\*Cross comparison of model results used by station engineers and science community using station vent, leakage and outgassing data for**

**-each stage in assembly sequence to identify potential problems early on**

**-identification of sensitive surfaces (which will change orientation as a function of stage)**

**\*Identification/quantification of neutral/plasma effects on Station hardware.**

**Carruth(MSFC/EH12)**

**\*Needed:**

**- definition of data required and models for environment**

**- meeting of atomic oxygen facility groups**

**- determine the causative processes involved in new LDEF phenomena (i.e. fluorescence and synergistic effects)**

**- studies of basic interactions which affect surfaces rather subtly over time**

**- investigations of plasma phenomena (interactions) on SSF systems and of mitigating techniques**

**Cuthbertson(PPPL):**

**For further progress we need:**

**\*laboratory investigation of synergistic phenomena (UV, temperature cycling)**

# **Cross Section Work at UAH/MSFC**

**Charles E. Keffer  
UAH**

**Presented at Space Station Freedom  
Induced External Environment Review  
January 31, 1991**

## **APPENDIX C**

A7

**“Radiation Damage Effects in Far  
Ultraviolet Filters and Substrates”**

**Presented by Dr. Charles E. Keffer**

**at**

**Passive Materials for Optical Elements II  
SPIE Annual Meeting  
14-15 July 1993  
San Diego, California**

# PROCEEDINGS REPRINT

 SPIE—The International Society for Optical Engineering

*Reprinted from*

## ***Passive Materials for Optical Elements II***

14–15 July 1993  
San Diego, California



**Volume 2018**



## Radiation Damage Effects in Far Ultraviolet Filters and Substrates

Charles E. Keffer<sup>1</sup>, Marsha R. Torr<sup>2</sup>, Muamer Zukic<sup>1</sup>,  
James F. Spann<sup>2</sup>, Douglas G. Torr<sup>1</sup>, and Jongmin Kim<sup>1</sup>

<sup>1</sup>Department of Physics  
The University of Alabama in Huntsville  
Optics Building, Suite 300  
Huntsville, AL 35899

<sup>2</sup>NASA/Marshall Space Flight Center  
Space Science Laboratory  
Huntsville, AL 35812

### ABSTRACT

New advances in VUV thin film filter technology have been made using filter designs with multilayers of materials such as  $\text{Al}_2\text{O}_3$ ,  $\text{BaF}_2$ ,  $\text{CaF}_2$ ,  $\text{HfO}_2$ ,  $\text{LaF}_3$ ,  $\text{MgF}_2$ , and  $\text{SiO}_2$ . Our immediate application for these filters will be in an imaging system to be flown on a satellite where a 2 X 9  $R_E$  orbit will expose the instrument to approximately 275 krad of radiation. In view of the fact that no previous studies have been made on potential radiation damage of these materials in the thin film format, we report on such an assessment here. Transmittances and reflectances of  $\text{BaF}_2$ ,  $\text{CaF}_2$ ,  $\text{HfO}_2$ ,  $\text{LaF}_3$ ,  $\text{MgF}_2$ , and  $\text{SiO}_2$  thin films on  $\text{MgF}_2$  substrates,  $\text{Al}_2\text{O}_3$  thin films on fused silica substrates, uncoated fused silica and  $\text{MgF}_2$ , and four multilayer filters made from these materials were measured from 120 nm to 180 nm before and after irradiation by 250 krad from a  $^{60}\text{Co}$  gamma radiation source. No radiation-induced losses in transmittance or reflectance occurred in this wavelength range. Additional postradiation measurements from 160 nm to 300 nm indicated a 3 - 5% radiation-induced absorption near 260 nm in some of the samples with  $\text{MgF}_2$  substrates. From these measurements it is concluded that far ultraviolet filters made from the materials tested should experience less than 5% change from exposure to up to 250 krad of high energy radiation in space applications.

### 1. INTRODUCTION

The Ultraviolet Imager (UVI) for the Global Geospace Science (GGS) POLAR spacecraft has been designed to acquire coherent global images of the Earth's aurora under both day and night conditions<sup>1</sup>. The major goals of the observations are to obtain information on the temporal and spatial morphology of the aurora, as well as on the total incident energy flux and energy characteristics of the precipitating particles giving rise to the aurora. In order to achieve these goals, a fast (f/2.9) imaging camera has been developed which obtains wide field of view (8°) images through 5 specially designed FUV filters. Success in achieving the scientific goals is therefore dependent on the high performance of these filters. In addition to spectral resolution of closely spaced features (130.4 nm and 135.6 nm), the filters must also have sufficiently high throughput in order to allow detection of the relatively weak Lyman Birge Hopfield bands of  $\text{N}_2$ , and must be capable of blocking out-of-band sunlight by a factor of  $10^4$  at wavelengths longer than 190 nm and isolating the OI emissions at 130.4 nm and 135.6 nm from the bright Lyman- $\alpha$

PRECEDING PAGE BLANK NOT FILMED

emission at 121.6 nm. Attainment of these filter characteristics has required the development of a new multilayer stack named the  $\Pi$  multilayer.<sup>2</sup> The design approach was to obtain high filter throughput by minimizing energy losses in the filters with the  $\Pi$  multilayer design and by operating in a reflective, rather than transmissive, mode. Each UVI filter consists of three  $\Pi$  multilayer reflection filters and one transmission filter in series to achieve the necessary performance requirements. The transmission filter provides short wavelength rejection by acting as a cut-on filter while the three reflectors provide excellent long wavelength rejection. Additional blocking of sunlight beyond 190 nm is provided by a solar blind CsI photocathode in the UVI detector. A detailed description of the design and development of the UVI filters is given by Zukic, et al.<sup>3</sup>

The three year mission lifetime of the POLAR spacecraft will result in a radiation exposure to the UVI of approximately 275 krad. Radiation damage to optical materials has a long history of study in the space science and nuclear physics fields. At ultraviolet wavelengths, transmission of optical materials exposed to high energy radiation has been previously measured for a variety of bulk materials including  $\text{Al}_2\text{O}_3$ <sup>4,5</sup>,  $\text{BaF}_2$ <sup>4,7</sup>,  $\text{CaF}_2$ <sup>4</sup>,  $\text{CsF}$ <sup>6</sup>, fused silica<sup>4,5,8-9</sup>,  $\text{LiF}$ <sup>4,5,10-11</sup>,  $\text{MgF}_2$ <sup>4,5,10-11</sup>, and several optical glass materials<sup>4,8</sup>. Ultraviolet transmission has also been measured for irradiated colored glass filters and thin film interference filters<sup>9</sup>. Ultraviolet reflectance measurements of irradiated optical materials have been made at 121.6 nm for aluminum mirrors with  $\text{MgF}_2$  protective coatings<sup>5,11</sup>. Radiation damage effects on the materials used in these FUV filters have not been previously studied in the thin film format. In this paper we report the results of an investigation into the potential for radiation induced damage to the UVI filters by making measurements on the thin films and substrates used to fabricate the filters. Only long term radiation damage was studied since measurements were not made immediately following radiation exposure.

## 2. EXPERIMENTAL PROCEDURES

A set of 22 samples was selected for use in this study. These include  $\text{BaF}_2$ ,  $\text{CaF}_2$ ,  $\text{HfO}_2$ ,  $\text{LaF}_3$ ,  $\text{MgF}_2$ , and  $\text{SiO}_2$  single layer thin films on  $\text{MgF}_2$  substrates (two of each),  $\text{Al}_2\text{O}_3$  single layer thin films on fused silica substrates (two), two uncoated  $\text{MgF}_2$  substrates, and two uncoated fused silica substrates. Two multilayer transmission filters ( $\text{BaF}_2/\text{MgF}_2$  on a  $\text{MgF}_2$  substrate) and two multilayer reflection filters ( $\text{LaF}_3/\text{MgF}_2$  on a fused silica substrate) were also used. Every single layer thin film has a thickness between 8 nm and 22 nm with the exact thickness for each film material corresponding to the optimum thickness from the  $\Pi$  multilayer design. The filters used are 35-layer  $\Pi$  stacks. The complete set of samples is summarized in Table 1 and is representative of the substrates, thin films, and filters which make up the UVI filter system.

All of the test samples were prepared with 12.7 mm diameter and 2 mm thick VUV grade substrates used as received from Acton Research Corporation.  $\text{BaF}_3$ ,  $\text{CaF}_3$ , and  $\text{LaF}_3$  film materials were 99.9% pure from CERAC.  $\text{Al}_2\text{O}_3$  (99.5%),  $\text{MgF}_2$  (99.95%), and  $\text{SiO}_2$  (99.98%) thin films were deposited with standard Balzers coating materials.  $\text{HfO}_2$  was supplied by EM Chemicals with 99.5% purity. All depositions were completed at The University of Alabama in Huntsville Optical Astronomy Laboratory. An oil-free coating chamber with a sorption pump and cryopump was used to prevent hydrocarbon contamination of the films.

One of each type of single layer thin film, one of each type of uncoated substrate and all of the multilayer filters were mounted in an aluminum sample holder which was then sealed in an ultrahigh purity dry nitrogen purged double bag made from ultra clean radiation resistant Aclar. The samples were subsequently taken to Goddard Space Flight Center where they were exposed for 110 hours to a  $^{60}\text{Co}$  gamma radiation source. The total dose received was 250 krad. After radiation exposure, the Aclar bag remained clear and had no visible evidence of radiation damage. The remaining single layer thin films and uncoated substrates served as control samples and received identical handling, with the exception of radiation exposure, including being sealed in an ultrahigh purity dry nitrogen purged double bag made from Aclar.

A series of reflectance and transmittance measurements was performed at the Marshall Space Flight Center Ionosphere Thermosphere Mesosphere Branch on the 22 samples described above. The preradiation measurements were performed in a hydrocarbon-free cryopumped vacuum chamber at a pressure below  $10^{-5}$  Torr. A deuterium lamp with a  $\text{MgF}_2$  window together with a 0.2-m vacuum monochromator provided 1 nm FWHM spectral resolution over the 120 nm to 180 nm wavelength range. Folding and collimating optics and a 6 mm diameter aperture limited the light incident on the eight position filter wheel holding the 12.7 mm diameter substrates to an area approximately 1/4th the area of the thin film. The small aperture insured that small positioning errors from rotating the filter wheel did not significantly impact the reproducibility of the measurements. A photomultiplier tube with a  $\text{MgF}_2$  window and a semi-transparent Cs-I photocathode served as the detector for all measurements. The postradiation measurements were accomplished in a different hydrocarbon-free cryopumped vacuum chamber also at a pressure below  $10^{-5}$  Torr. A similar deuterium lamp, 0.2-m vacuum monochromator, and aperture were used for the postradiation measurements. However, the second chamber did not have any folding and collimating optics. The same Cs-I photomultiplier tube and eight position filter wheel was used for both the pre- and postradiation measurements in the 120 nm to 180 nm wavelength range. A second set of postradiation transmission measurements was made from 160 nm to 300 nm using a Cs-Te photomultiplier tube. All reflectance measurements were performed at a  $45^\circ$  angle of incidence while transmittance was measured at normal incidence. Figures 1 and 2 illustrate the optical configurations for the two vacuum chambers utilized.

For the reflection measurements, two identical scans from 120 nm to 180 nm were performed on every sample both before and after the radiation exposure. A reference reflection filter was measured as a control with every reflection measurement to check the reliability and reproducibility of the data from measurement to measurement. The reference filter also insured that no systematic errors were introduced when the vacuum chamber was vented and a new set of samples was installed. Two identical transmission measurements from 120 nm to 180 nm were also performed on every sample both before and after the radiation exposure. An uncoated fused silica substrate in the incident beam served as a filter to block second order monochromator reflections for the 160 nm to 300 nm postradiation transmission measurements. Two identical scans from 160 nm to 300 nm were recorded for each sample. A reference transmission filter was measured with every transmission measurement as a check on the measurement reliability and reproducibility. The reflection and transmission reference filters also provided traceability between the two vacuum chambers used in the preradiation and postradiation measurements.

Absolute reflectance values were determined by comparing the reflected beam intensity from each filter with the reflected beam intensity from a VUV-enhanced aluminum mirror whose reflectance was calibrated using an Acton vacuum reflectometer model VRSC-100. Absolute transmittance values were determined by measuring the ratio of the transmitted beam intensity to the unattenuated beam intensity measured at an empty filter wheel position. Background signal was subtracted and signal drift was corrected using measurements before and after the filters were measured.

### 3. RESULTS

The primary wavelength range of interest for the UVI filters is 120 nm to 180 nm. Transmission and reflection measurements in this range were analyzed by first averaging the two scans taken for each sample. The difference, defined as the average of the postradiation measurements minus the average of the preradiation measurements, was then calculated. Figures 3 through 11 show the results for all of the thin films studied. The error bars represent one standard deviation. The preradiation measurements have a lower signal to noise ratio due to signal intensity losses from the folding and collimating optics used in the preradiation measurements but not in the postradiation measurements.

Repeated measurements of the transmission and reflection reference filters result in an estimated measurement uncertainty ( $\sigma$ ) of 2%. Differences between the postradiation and preradiation measurements of greater than 4% are considered to be due to radiation-induced effects. Particular regard is given to those wavelengths where radiation-induced absorption bands are known to occur in the bulk materials.<sup>4</sup> With this criterion as a benchmark, none of the 13 samples which each received 250 krad of radiation showed evidence of statistically significant radiation-induced changes in reflectance in the 120 nm to 180 nm wavelength range. For the transmittance measurements in the 120 nm to 180 nm range, only the  $\text{MgF}_2$  uncoated substrate had any statistically significant changes. This sample had an apparent absorption short of 160 nm before radiation exposure which was not present after 250 krad radiation exposure.

Most of the UV optical materials that have been studied in bulk form have their strongest radiation-induced absorption bands at wavelengths longer than 180 nm.<sup>4</sup> From 160 nm to 300 nm, the irradiated samples were compared with their equivalent control samples since no preradiation measurements were made in this wavelength range. Differences were calculated in the same manner as for the 120 nm to 180 nm wavelength measurements. Of the nine irradiated samples in this group, three show evidence of a small radiation-induced absorption band centered near 250 nm - 260 nm. Figures 5, 8, and 9 are for a  $\text{CaF}_2$  film on a  $\text{MgF}_2$  substrate, a  $\text{LaF}_3$  film on a  $\text{MgF}_2$  substrate, and a  $\text{MgF}_2$  film on a  $\text{MgF}_2$  substrate, respectively. The coincidence of the absorption with the well known 260 nm absorption band in  $\text{MgF}_2$ <sup>4</sup> and the fact that the  $\text{MgF}_2$  substrate is common to the three samples strongly suggests that the radiation damage is limited to the  $\text{MgF}_2$  bulk material. The small 3 - 5% absorption seen in these three samples is near the limit of the measurement uncertainty and thus explains how four other samples with  $\text{MgF}_2$  substrates do not show similar indications of radiation-induced absorption.

Heath and Sacher<sup>4</sup> irradiated a 1.5 mm thick  $\text{MgF}_2$  crystal with  $10^{14}$  electrons/cm<sup>2</sup> at 1 MeV followed by  $10^{14}$  electrons/cm<sup>2</sup> at 2 MeV. They observed 16% loss in transmittance at 120

nm and approximately 60% loss in transmittance at 260 nm. Hass and Hunter<sup>5</sup> reported a 5% decrease in transmittance at 121.6 nm and approximately 20% decrease at 260 nm after exposure of their 3 mm thick  $\text{MgF}_2$  crystal to  $10^{15}$  electrons/cm<sup>2</sup> at 1 MeV. They attribute the smaller loss in transmittance compared with Heath and Sacher's results to a  $\text{MgF}_2$  crystal which was probably higher in purity. Becher, et al.<sup>10</sup> found approximately 20% decrease in  $\text{MgF}_2$  transmittance at 260 nm from irradiation with  $8 \times 10^{12}$  protons/cm<sup>2</sup> at 85 MeV. Reft, et al.<sup>11</sup> measured  $\text{MgF}_2$  transmittance losses of 10% at 121.6 nm and 14% at 180 nm from irradiation with 85 - and 600-MeV protons at a total absorbed energy of  $5.7 \times 10^{14}$  MeV/cm<sup>3</sup>. In the present study, the total absorbed energy in the samples with  $\text{MgF}_2$  substrates is  $5 \times 10^{13}$  MeV/cm<sup>3</sup>. This is over ten times less total energy absorbed than in any of the other reports cited. The maximum 5% transmittance loss at 260 nm and no measurable change at 120 nm reported in the present study is thus in reasonable agreement with the earlier reports on radiation-induced damage in  $\text{MgF}_2$  crystals.

Fused silica has been reported by Heath and Sacher<sup>4</sup> to decrease in transmittance approximately 15% at 220 nm after irradiation with  $10^{14}$  electrons/cm<sup>2</sup> at 1 MeV and  $10^{14}$  electrons/cm<sup>2</sup> at 2 MeV. Hass and Hunter<sup>5</sup> measured approximately 10% loss in transmittance at 220 nm after irradiation of fused silica by  $10^{15}$  electrons/cm<sup>2</sup> at 1 MeV. Nicoletta and Eubanks<sup>9</sup> used  $10^{14}$  electrons/cm<sup>2</sup> at 1.5 MeV to irradiate fused silica and reported similar transmittance losses to Heath and Sacher. In the present study, no radiation-induced transmission losses were observed in the samples with fused silica substrates. The total absorbed energy was  $3 \times 10^{13}$  MeV/cm<sup>3</sup> for these samples.

Nicoletta and Eubanks<sup>9</sup> measured radiation damage in three interference filters which were shielded by 3.1 mm of fused silica and then irradiated with  $2.7 \times 10^{13}$  electrons/cm<sup>2</sup> of energies 0.3 MeV, 0.5 MeV, 1.0 MeV, and 1.5 MeV. Transmission losses were very small from the electron irradiation shielded by the fused silica. No changes in transmittance or reflectance have been observed in the present study which can be attributed to radiation damage in the thin films used. This is probably because only a small fraction of the energy is likely to be absorbed in the thin films and also because the radiation levels used were moderate.

#### 4. CONCLUSION

None of the samples tested showed evidence of any major radiation-induced changes in reflectance or transmittance. Since the UVI filters are made from materials which we have tested and since they are housed within the body of the instrument where they will experience a total radiation dose of less than 20 krads, it is anticipated that they will suffer negligible loss in reflectance or transmittance during the nominal 3 year mission lifetime of the POLAR spacecraft.

#### 5. ACKNOWLEDGEMENTS

This work was supported by NASA grant NAG8-834 and NASA contract NAS8-38145.

#### 6. REFERENCES

1. M. R. Torr, D. G. Torr, M. Zukic, J. Spann, and R. B. Johnson, "An Ultraviolet Imager

- for the International Solar-Terrestrial Physics Mission," submitted to *Rev. Space Sci.*, Jan. 1993.
2. M. Zukic and D. G. Torr, "Multiple reflectors as narrow-band and broadband VUV filters," *Appl. Opt.* **31**, 1588-1596 (1992).
  3. M. Zukic, D. G. Torr, J. Kim, J. F. Spann, and M. R. Torr, "Far ultraviolet filters for the ISTP UV Imager," *Instrumentation for Planetary and Terrestrial Atmospheric Sensing*, SPIE Proceedings Vol. 1745, 99-107 (1992).
  4. D. F. Heath and P. A. Sacher, "Effects of a simulated high-energy space environment on the ultraviolet transmittance of optical materials between 1050 Å and 3000 Å," *Appl. Opt.* **5**, 937-943 (1966).
  5. G. Hass and W. R. Hunter, "Laboratory experiments to study surface contamination and degradation of optical coatings and materials in simulated space environments," *Appl. Opt.* **9**, 2101-2110 (1970).
  6. S. Majewski and M. K. Bently, "Gamma radiation induced damage effects in the transmission of barium fluoride and cesium fluoride fast crystal scintillators," *Nucl. Instr. and Meth.* **A260**, 373-376, (1987).
  7. M. Murashita, H. Saitoh, K. Tobimatsu, M. Chiba, T. Hirose and F. Takasaki, "Performance and radiation damage of a BaF<sub>2</sub> calorimeter," *Nucl. Instr. and Meth.* **A243**, 67-76 (1986).
  8. M. T. Shetter and V. J. Abreu, "Radiation effects on the transmission of various optical glasses and epoxies," *Appl. Opt.* **18**, 1132-1133 (1979).
  9. C. A. Nicoletta and A. G. Eubanks, "Effect of simulated space radiation on selected optical materials," *Appl. Opt.* **11**, 1365-1370 (1972).
  10. J. Becher, R. L. Kernell and C. S. Reft, "Proton-induced F-centers in LiF and MgF<sub>2</sub>," *J. Phys. Chem. Solids* **44**, 759-763 (1983).
  11. C. S. Reft, J. Becher and R. L. Kernell, "Proton-induced degradation of VUV transmission of LiF and MgF<sub>2</sub>," *Appl. Opt.* **19**, 4156-4158 (1980).
  12. L. R. Canfield, G. Hass and J. E. Waylonis, "Further studies of MgF<sub>2</sub>-overcoated aluminum mirrors with highest reflectance in the vacuum ultraviolet," *Appl. Opt.* **5**, 45-50 (1966).

Table 1: Summary of thin films and substrates tested.

Film Type	Film Materials	Substrate
Single Layer	$\text{Al}_2\text{O}_3$	Fused Silica
Single Layer	$\text{BaF}_2$	$\text{MgF}_2$
Single Layer	$\text{CaF}_2$	$\text{MgF}_2$
Single Layer	$\text{HfO}_2$	$\text{MgF}_2$
Single Layer	$\text{LaF}_3$	$\text{MgF}_2$
Single Layer	$\text{MgF}_2$	$\text{MgF}_2$
Single Layer	$\text{SiO}_2$	$\text{MgF}_2$
$\Pi$ Multilayer	$\text{BaF}_2/\text{MgF}_2$	$\text{MgF}_2$
$\Pi$ Multilayer	$\text{LaF}_3/\text{MgF}_2$	Fused Silica
None	None	Fused Silica
None	None	$\text{MgF}_2$

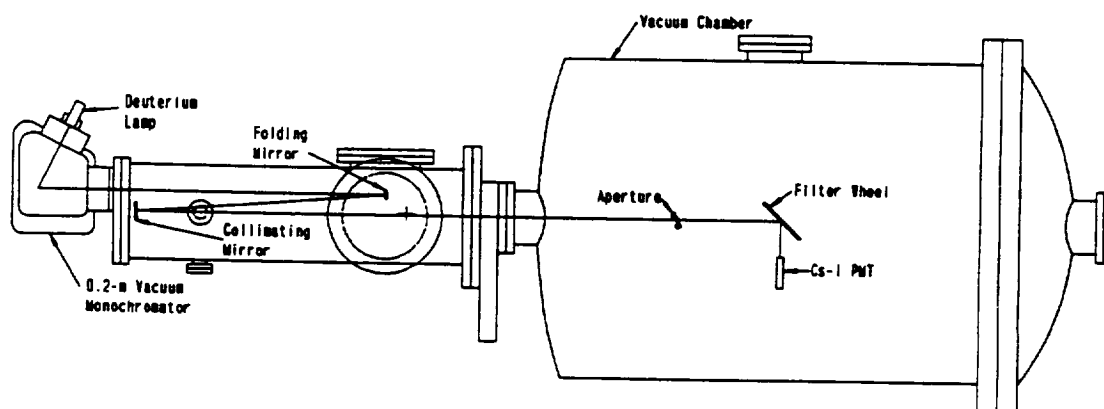


Figure 1: Vacuum chamber for preradiation measurements. Chamber is hydrocarbon free and cryogenically pumped. Optical configuration shown is for 45° reflectance measurements.

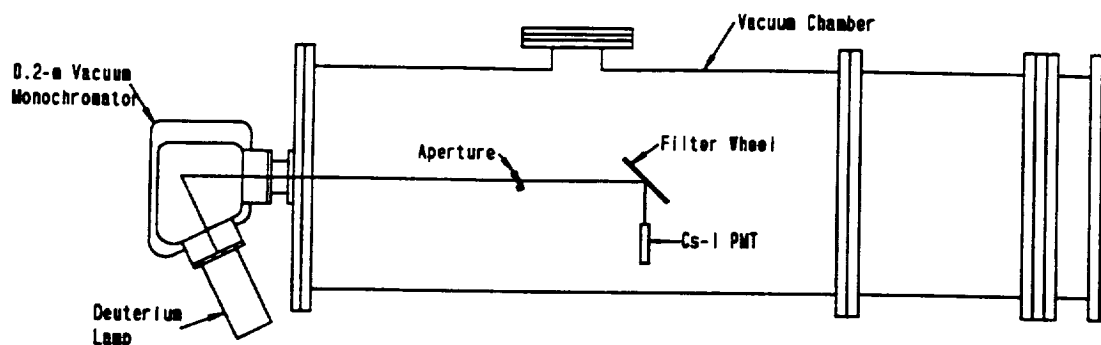


Figure 2: Vacuum chamber for postradiation measurements. Chamber is hydrocarbon free and cryogenically pumped. Optical configuration shown is for 45° reflectance measurements using a Cs-I pmt for the 120 nm to 180 nm range.

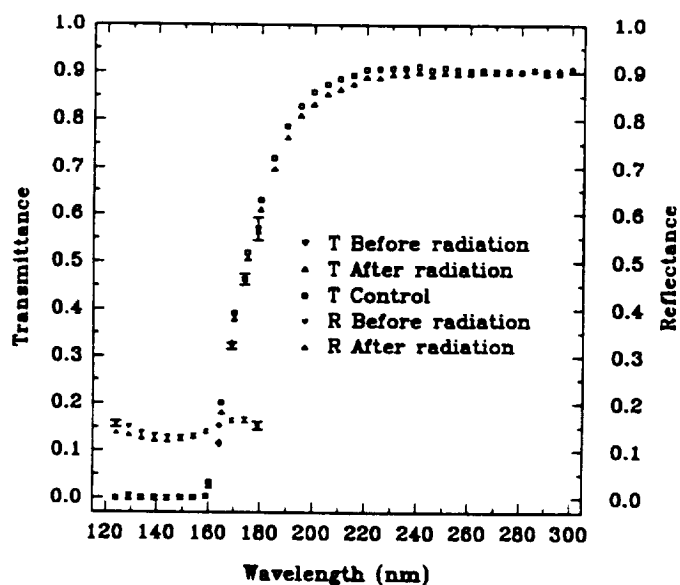


Figure 3: Reflectance and transmittance of an  $\text{Al}_2\text{O}_3$  thin film on a fused silica substrate. Comparison is shown in the 120 nm to 180 nm range before and after radiation exposure of a single sample. In the 160 nm to 300 nm range, comparison is between the radiation exposed sample and a control sample with no radiation exposure.



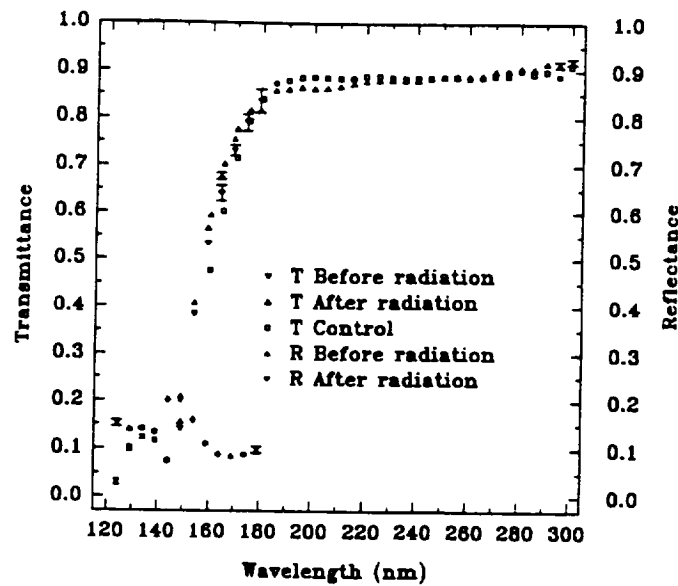


Figure 4: Reflectance and transmittance of a  $\text{BaF}_2$  thin film on a  $\text{MgF}_2$  substrate. Comparison is shown in the 120 nm to 180 nm range before and after radiation exposure of a single sample. In the 160 nm to 300 nm range, comparison is between the radiation exposed sample and a control sample with no radiation exposure.

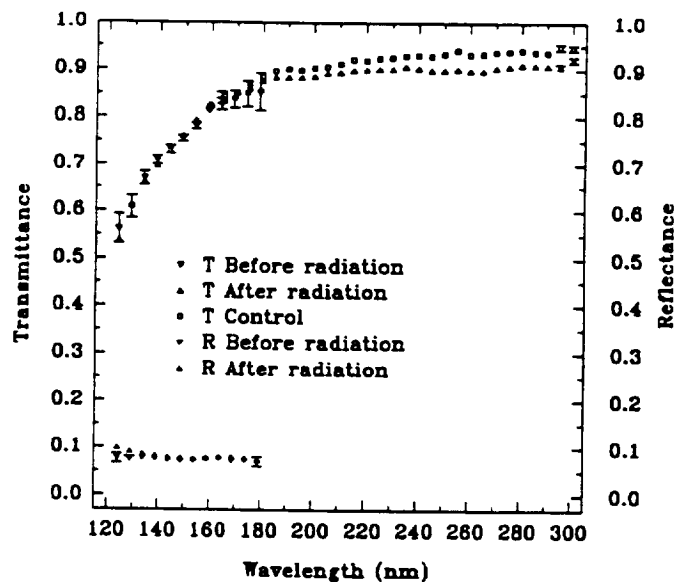


Figure 5: Reflectance and transmittance of a  $\text{CaF}_2$  thin film on a  $\text{MgF}_2$  substrate. Comparison is shown in the 120 nm to 180 nm range before and after radiation exposure of a single sample. In the 160 nm to 300 nm range, comparison is between the radiation exposed sample and a control sample with no radiation exposure.

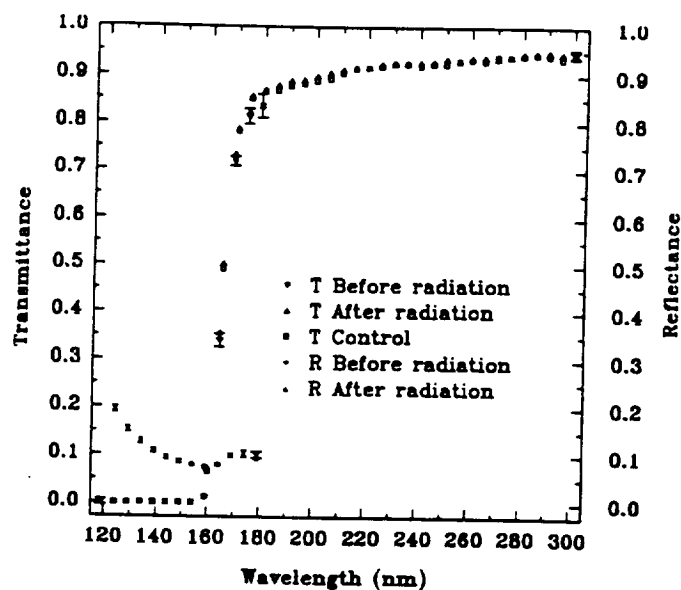


Figure 6: Reflectance and transmittance of an uncoated fused silica substrate. Comparison is shown in the 120 nm to 180 nm range before and after radiation exposure of a single sample. In the 160 nm to 300 nm range, comparison is between the radiation exposed sample and a control sample with no radiation exposure.

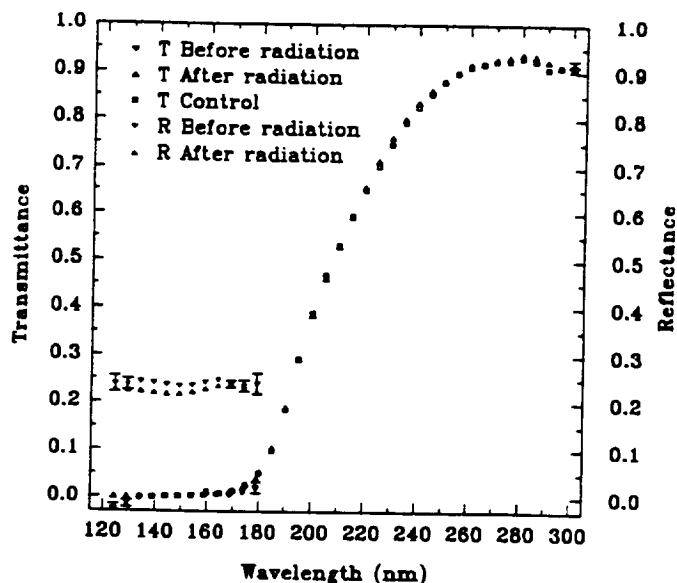


Figure 7: Reflectance and transmittance of a  $\text{HfO}_2$  thin film on a  $\text{MgF}_2$  substrate. Comparison is shown in the 120 nm to 180 nm range before and after radiation exposure of a single sample. In the 160 nm to 300 nm range, comparison is between the radiation exposed sample and a control sample with no radiation exposure.

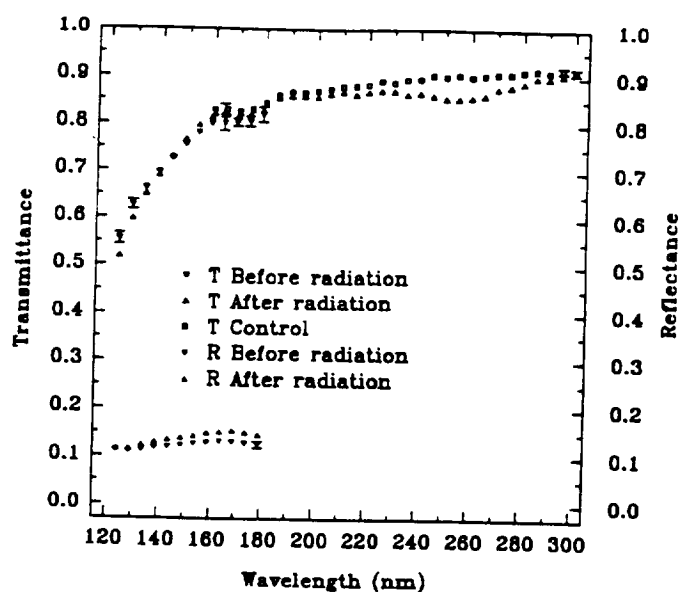


Figure 8: Reflectance and transmittance of a  $\text{LaF}_3$  thin film on a  $\text{MgF}_2$  substrate. Comparison is shown in the 120 nm to 180 nm range before and after radiation exposure of a single sample. In the 160 nm to 300 nm range, comparison is between the radiation exposed sample and a control sample with no radiation exposure.

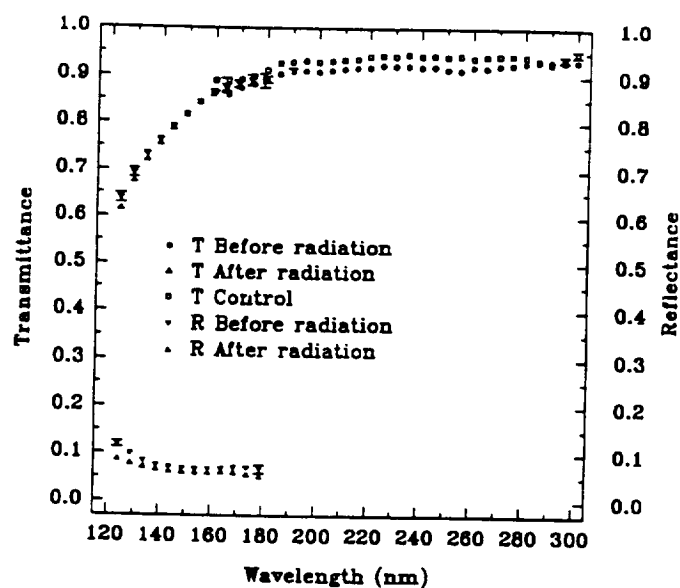


Figure 9: Reflectance and transmittance of a  $\text{MgF}_2$  thin film on a  $\text{MgF}_2$  substrate. Comparison is shown in the 120 nm to 180 nm range before and after radiation exposure of a single sample. In the 160 nm to 300 nm range, comparison is between the radiation exposed sample and a control sample with no radiation exposure.

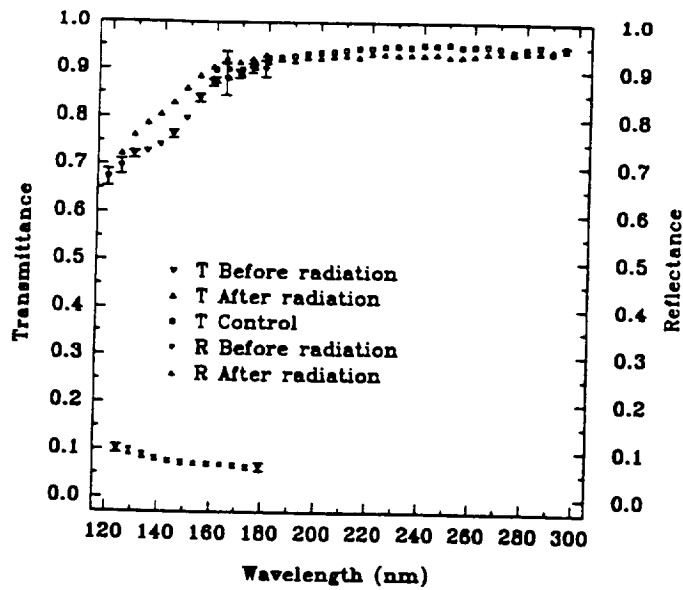


Figure 10: Reflectance and transmittance of an uncoated  $\text{MgF}_2$  substrate. Comparison is shown in the 120 nm to 180 nm range before and after radiation exposure of a single sample. In the 160 nm to 300 nm range, comparison is between the radiation exposed sample and a control sample with no radiation exposure.

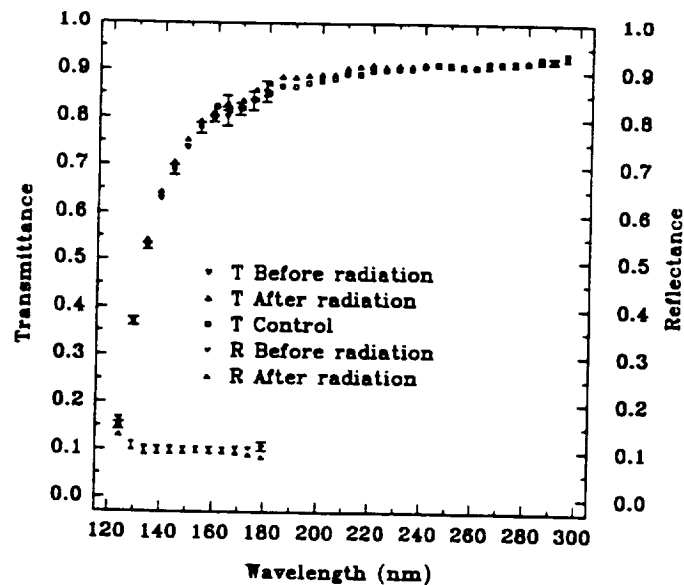


Figure 11: Reflectance and transmittance of a  $\text{SiO}_2$  thin film on a  $\text{MgF}_2$  substrate. Comparison is shown in the 120 nm to 180 nm range before and after radiation exposure of a single sample. In the 160 nm to 300 nm range, comparison is between the radiation exposed sample and a control sample with no radiation exposure.

**APPENDIX D**

**“Radiation Damage Effects in Far Ultraviolet  
Filters, Thin Films, and Substrates”**

Applied Optics, in press.

**Radiation Damage Effects in Far Ultraviolet  
Filters, Thin Films, and Substrates**

**Charles E. Keffer<sup>1</sup>, Marsha R. Torr<sup>2</sup>, Muamer Zukic<sup>1</sup>,  
James F. Spann<sup>3</sup>, Douglas G. Torr<sup>1</sup>, and Jongmin Kim<sup>1</sup>**

<sup>1</sup>Department of Physics  
The University of Alabama in Huntsville  
Optics Building, Suite 300  
Huntsville, AL 35899

<sup>2</sup>NASA/Marshall Space Flight Center  
Payload Projects Office  
Huntsville, AL 35812

<sup>3</sup>NASA/Marshall Space Flight Center  
Space Science Laboratory  
Huntsville, AL 35812

## **Abstract**

New advances in VUV thin film filter technology have been made using filter designs with multilayers of materials such as  $\text{Al}_2\text{O}_3$ ,  $\text{BaF}_2$ ,  $\text{CaF}_2$ ,  $\text{HfO}_2$ ,  $\text{LaF}_3$ ,  $\text{MgF}_2$ , and  $\text{SiO}_2$ . Our immediate application for these filters will be in an imaging system to be flown on a satellite where a 2 X 9  $R_E$  orbit will expose the instrument to approximately 250 krads of radiation. In view of the fact that no previous studies have been made on potential radiation damage of these materials in the thin film format, we report on such an assessment here. Transmittances and reflectances of  $\text{BaF}_2$ ,  $\text{CaF}_2$ ,  $\text{HfO}_2$ ,  $\text{LaF}_3$ ,  $\text{MgF}_2$ , and  $\text{SiO}_2$  thin films on  $\text{MgF}_2$  substrates,  $\text{Al}_2\text{O}_3$  thin films on fused silica substrates, uncoated fused silica and  $\text{MgF}_2$ , and four multilayer filters made from these materials were measured from 120 nm to 180 nm before and after irradiation by 250 krads from a  $^{60}\text{Co}$  gamma radiation source. No radiation-induced losses in transmittance or reflectance occurred in this wavelength range. Additional postradiation measurements from 160 nm to 300 nm indicated a 2 - 5% radiation-induced absorption near 260 nm in some of the samples with  $\text{MgF}_2$  substrates. From these measurements it is concluded that far ultraviolet filters made from the materials tested should experience less than 5% change from exposure to up to 250 krads of high energy radiation in space applications.

*Key words:* Radiation effects, ultraviolet filters, thin films

### **A. Introduction**

The Ultraviolet Imager (UVI) for the Global Geospace Science (GGS) POLAR spacecraft has been designed to acquire coherent global images of the Earth's aurora under both day and

night conditions<sup>1</sup>. The major goals of the observations are to obtain information on the temporal and spatial morphology of the aurora, as well as on the total incident energy flux and energy characteristics of the precipitating particles giving rise to the aurora. In order to achieve these goals, a fast (f/2.9) imaging camera has been developed which obtains wide field of view (8°) images through 5 specially designed FUV filters. Success in achieving the scientific goals is therefore dependent on the high performance of these filters. In addition to spectral resolution of closely spaced features (130.4 nm and 135.6 nm), the filters must also have sufficiently high throughput in order to allow detection of the relatively weak Lyman Birge Hopfield bands of N<sub>2</sub>, and must be capable of blocking out-of-band sunlight by a factor of 10<sup>4</sup> at wavelengths longer than 190 nm and isolating the OI emissions at 130.4 nm and 135.6 nm from the bright Lyman-α emission at 121.6 nm. Attainment of these filter characteristics has required the development of a new multilayer stack named the Π multilayer.<sup>2</sup> The design approach was to obtain high filter throughput by minimizing energy losses in the filters with the Π multilayer design and by operating in a reflective, rather than transmissive, mode. Each UVI filter consists of three Π multilayer reflection filters and one transmission filter in series to achieve the necessary performance requirements. The transmission filter provides short wavelength rejection by acting as a cut-on filter while the three reflectors provide excellent long wavelength rejection. Additional blocking of sunlight beyond 190 nm is provided by a solar blind CsI photocathode in the UVI detector. A detailed description of the design and development of the UVI filters is given by Zukic, et al.<sup>3</sup>

The three year mission lifetime of the POLAR spacecraft will result in a radiation exposure to the UVI of approximately 250 krads due to passage of the spacecraft through the



Earth's radiation belts. This radiation environment consists primarily of electrons and protons with energies from less than 1 MeV to tens of MeV. Bremsstrahlung from high energy electrons impacting the spacecraft or instrument housings can also be a major source of radiation. We have taken the common approach of using a  $^{60}\text{Co}$  gamma radiation source to simulate the Earth's radiation environment. In order for this to be a valid approach for radiation damage assessments in optical materials, the density of F-center formation from different types of radiation must be known. Durand, et al.<sup>4</sup> have found that the density of F-center formation from x-ray bombardment of LiF is proportional to the square root of the total energy absorbed. Becher, et al.<sup>5</sup> have found that the same relationship holds true for proton and electron bombardment of LiF and  $\text{MgF}_2$  with some deviation below a few Mrad in  $\text{MgF}_2$ . The use of a  $^{60}\text{Co}$  radiation source to simulate radiation damage to optical materials in space should be a reasonable approximation particularly for optical elements which are fairly well shielded from direct exposure to the proton and electron flux.

Radiation damage to optical materials has a long history of study in the space science and nuclear physics fields. At ultraviolet wavelengths, transmission of optical materials exposed to high energy radiation has been previously measured for a variety of bulk materials including  $\text{Al}_2\text{O}_3$ <sup>6,7</sup>,  $\text{BaF}_2$ <sup>6,9</sup>,  $\text{CaF}_2$ <sup>6</sup>,  $\text{CsF}$ <sup>8</sup>, fused silica<sup>6,7,10-11</sup>,  $\text{LiF}$ <sup>5,7,12</sup>,  $\text{MgF}_2$ <sup>5,7,12</sup>, and several optical glass materials<sup>6,10</sup>. Ultraviolet transmission has also been measured for irradiated colored glass filters and thin film interference filters<sup>11</sup>. Ultraviolet reflectance measurements of irradiated optical materials have been made at 121.6 nm for aluminum mirrors with  $\text{MgF}_2$  protective coatings<sup>7,12</sup>. Radiation damage effects on the materials used in the UVI filters have not been previously studied in the thin film format. In this paper we report the results of an investigation into the

potential for radiation-induced damage to the UVI filters by making measurements on the thin films and substrates used to fabricate the filters. Only long term radiation damage was studied since measurements were not made immediately following radiation exposure.

## **B. Experimental Procedures**

A set of 22 samples was selected for use in this study. These include  $\text{BaF}_2$ ,  $\text{CaF}_2$ ,  $\text{HfO}_2$ ,  $\text{LaF}_3$ ,  $\text{MgF}_2$ , and  $\text{SiO}_2$  single layer thin films on  $\text{MgF}_2$  substrates (two of each),  $\text{Al}_2\text{O}_3$  single layer thin films on fused silica substrates (two), two uncoated  $\text{MgF}_2$  substrates, and two uncoated fused silica substrates. Two multilayer transmission filters ( $\text{BaF}_2/\text{MgF}_2$  on a  $\text{MgF}_2$  substrate) and two multilayer reflection filters ( $\text{LaF}_3/\text{MgF}_2$  on a fused silica substrate) were also used. Every single layer thin film has a thickness between 8 nm and 22 nm with the exact thickness for each film material corresponding to the optimum thickness from the  $\Pi$  multilayer design. The filters used are 35-layer  $\Pi$  stacks. The complete set of samples is representative of the substrates, thin films, and filters which make up the UVI filter system.

All of the test samples were prepared with 12.7 mm diameter and 2 mm thick VUV grade substrates used as received from Acton Research Corporation.  $\text{BaF}_3$ ,  $\text{CaF}_3$ , and  $\text{LaF}_3$  film materials were 99.9% pure from CERAC.  $\text{Al}_2\text{O}_3$  (99.5%),  $\text{MgF}_2$  (99.95%), and  $\text{SiO}_2$  (99.98%) thin films were deposited with standard Balzers coating materials.  $\text{HfO}_2$  was supplied by EM Chemicals with 99.5% purity. All depositions were completed at The University of Alabama in Huntsville Optical Astronomy Laboratory. An oil-free coating chamber with a sorption pump and cryopump was used to prevent hydrocarbon contamination of the films.

One of each type of single layer thin film, one of each type of uncoated substrate and all

of the multilayer filters were mounted in an aluminum sample holder which was then sealed in an ultrahigh purity dry nitrogen purged double bag made from ultra clean radiation resistant Aclar. The samples were subsequently taken to Goddard Space Flight Center where they were exposed for 110 hours to a  $^{60}\text{Co}$  gamma radiation source. The total dose received was 250 krads. After radiation exposure, the Aclar bag remained clear and had no visible evidence of radiation damage. The remaining single layer thin films and uncoated substrates served as control samples and received identical handling, with the exception of radiation exposure, including being sealed in an ultrahigh purity dry nitrogen purged double bag made from Aclar.

A series of reflectance and transmittance measurements was performed at the Marshall Space Flight Center Ionosphere Thermosphere Mesosphere Branch on the 22 samples described above. The preradiation measurements were performed in a hydrocarbon-free cryopumped vacuum chamber at a pressure below  $10^{-5}$  Torr. A deuterium lamp with a  $\text{MgF}_2$  window together with a 0.2-m vacuum monochromator provided 1 nm FWHM spectral resolution over the 120 nm to 180 nm wavelength range. Folding and collimating optics and a 6 mm diameter aperture limited the light incident on the eight position filter wheel holding the 12.7 mm diameter substrates to an area approximately 1/4th the area of the thin film. The small aperture insured that small positioning errors from rotating the filter wheel did not significantly impact the reproducibility of the measurements. A photomultiplier tube with a  $\text{MgF}_2$  window and a semi-transparent Cs-I photocathode served as the detector for all measurements. The postradiation measurements were accomplished in a different hydrocarbon-free cryopumped vacuum chamber also at a pressure below  $10^{-5}$  Torr. A similar deuterium lamp, 0.2-m vacuum monochromator, and aperture were used for the postradiation measurements. However, the second chamber did

not have any folding and collimating optics. The same Cs-I photomultiplier tube and eight position filter wheel was used for both the pre- and postradiation measurements in the 120 nm to 180 nm wavelength range. A second set of postradiation transmission measurements was made from 160 nm to 300 nm using a Cs-Te photomultiplier tube. All reflectance measurements were performed at a 45° angle of incidence while transmittance was measured at normal incidence.

For the reflection measurements, two identical scans from 120 nm to 180 nm were performed on every sample both before and after the radiation exposure. A reference reflection filter was measured as a control with every reflection measurement to check the reliability and reproducibility of the data from measurement to measurement. The reference filter also insured that no systematic errors were introduced when the vacuum chamber was vented and a new set of samples was installed. Two identical transmission measurements from 120 nm to 180 nm were also performed on every sample both before and after the radiation exposure. An uncoated fused silica substrate in the incident beam served as a filter to block second order monochromator reflections for the 160 nm to 300 nm postradiation transmission measurements. Two identical scans from 160 nm to 300 nm were recorded for each sample. A reference transmission filter was measured with every transmission measurement as a check on the measurement reliability and reproducibility. The reflection and transmission reference filters also provided traceability between the two vacuum chambers used in the preradiation and postradiation measurements.

Absolute reflectance values were determined by comparing the reflected beam intensity from each filter with the reflected beam intensity from a VUV-enhanced aluminum mirror whose reflectance was calibrated using an Acton vacuum reflectometer model VRSC-100. Absolute

transmittance values were determined by measuring the ratio of the transmitted beam intensity to the unattenuated beam intensity measured at an empty filter wheel position. Background signal was subtracted and signal drift was corrected using measurements before and after the filters were measured.

### C. Results

The primary wavelength range of interest for the UVI filters is 120 nm to 180 nm. Transmission and reflection measurements in this range were analyzed by averaging the two scans taken for each sample. Repeated measurements of the transmission and reflection reference filters result in an estimated measurement uncertainty ( $\sigma$ ) of  $\pm 2\%$ . Differences between the postradiation and preradiation measurements of greater than 2% are considered to be due to radiation-induced effects. Particular regard is given to those wavelengths where radiation-induced absorption bands are known to occur in the bulk materials.<sup>6</sup> With this criterion as a benchmark, none of the 13 samples which each received 250 krad of radiation showed evidence of statistically significant radiation-induced changes in reflectance in the 120 nm to 180 nm wavelength range. For the transmittance measurements in the 120 nm to 180 nm range, only the  $\text{MgF}_2$  uncoated substrate had any statistically significant changes. This sample had an apparent absorption short of 160 nm before radiation exposure which was not present after 250 krad radiation exposure (see Figure 1).

Most of the UV optical materials that have been studied in bulk form have their strongest radiation-induced absorption bands at wavelengths longer than 180 nm.<sup>6</sup> From 160 nm to 300 nm, the irradiated samples were compared with their equivalent control samples since no

preradiation measurements were made in this wavelength range. Of the nine irradiated samples in this group, only the  $\text{CaF}_2$  film on a  $\text{MgF}_2$  substrate (Figure 2) and the  $\text{LaF}_3$  film on a  $\text{MgF}_2$  substrate (Figure 3) show evidence of a small radiation-induced absorption band centered near 250 nm - 260 nm. The coincidence of the absorption with the well known 260 nm F-center absorption band in  $\text{MgF}_2$ <sup>6</sup> and the fact that the  $\text{MgF}_2$  substrate is common to these samples strongly suggests that the radiation damage is limited to the  $\text{MgF}_2$  bulk material. The small 2 - 5% absorption seen in these samples is near the limit of the measurement uncertainty and thus explains how the other samples with  $\text{MgF}_2$  substrates do not show similar indications of radiation-induced absorption.

The four multilayer filter samples were measured in the wavelength range from 120 nm to 180 nm. None of these filters show any statistically significant radiation-induced changes in transmittance or reflectance. Table 1 summarizes the results for all the filters, thin films, and substrates tested.

Heath and Sacher<sup>6</sup> irradiated a 1.5 mm thick  $\text{MgF}_2$  crystal with  $10^{14}$  electrons/cm<sup>2</sup> at 1 MeV followed by  $10^{14}$  electrons/cm<sup>2</sup> at 2 MeV. They observed 16% loss in transmittance at 120 nm and approximately 60% loss in transmittance at 260 nm. Hass and Hunter<sup>7</sup> reported a 5% decrease in transmittance at 121.6 nm and approximately 20% decrease at 260 nm after exposure of their 3 mm thick  $\text{MgF}_2$  crystal to  $10^{15}$  electrons/cm<sup>2</sup> at 1 MeV. They attribute the smaller loss in transmittance compared with Heath and Sacher's results to a  $\text{MgF}_2$  crystal which was probably higher in purity. Becher, et al.<sup>5</sup> found approximately 20% decrease in  $\text{MgF}_2$  transmittance at 260 nm from irradiation with  $8 \times 10^{12}$  protons/cm<sup>2</sup> at 85 MeV. Reft, et al.<sup>12</sup> measured  $\text{MgF}_2$  transmittance losses of 10% at 121.6 nm and 14% at 180 nm from irradiation with 85 - and 600-

MeV protons at a total absorbed energy of  $5.7 \times 10^{14}$  MeV/cm<sup>3</sup>. In the present study, the total absorbed energy in the samples with MgF<sub>2</sub> substrates is  $5 \times 10^{13}$  MeV/cm<sup>3</sup>. This is over ten times less total energy absorbed than in any of the other reports cited. The maximum 5% transmittance loss at 260 nm and no measurable change at 120 nm reported in the present study is thus in reasonable agreement with the earlier reports on radiation-induced damage in MgF<sub>2</sub> crystals.

Fused silica has been reported by Heath and Sacher<sup>6</sup> to decrease in transmittance approximately 15% at 220 nm after irradiation with  $10^{14}$  electrons/cm<sup>2</sup> at 1 MeV and  $10^{14}$  electrons/cm<sup>2</sup> at 2 MeV. Hass and Hunter<sup>7</sup> measured approximately 10% loss in transmittance at 220 nm after irradiation of fused silica by  $10^{15}$  electrons/cm<sup>2</sup> at 1 MeV. Nicoletta and Eubanks<sup>11</sup> used  $10^{14}$  electrons/cm<sup>2</sup> at 1.5 MeV to irradiate fused silica and reported similar transmittance losses to Heath and Sacher.<sup>6</sup> In the present study, no radiation-induced transmission losses were observed in the samples with fused silica substrates. The total absorbed energy was  $3 \times 10^{13}$  MeV/cm<sup>3</sup> for these samples.

Nicoletta and Eubanks<sup>11</sup> measured radiation damage in three interference filters which were shielded by 3.1 mm of fused silica and then irradiated with  $2.7 \times 10^{13}$  electrons/cm<sup>2</sup> of energies 0.3 MeV, 0.5 MeV, 1.0 MeV, and 1.5 MeV. Transmission losses were very small from the electron irradiation shielded by the fused silica. No changes in transmittance or reflectance have been observed in the present study which can be attributed to radiation damage in the thin films used. This is probably because only a small fraction of the energy is likely to be absorbed in the thin films and also because the radiation levels used were moderate.

#### **D. Conclusion**

None of the samples tested showed evidence of any major radiation-induced changes in reflectance or transmittance. Since the UVI filters are made from materials which we have tested and since they are housed within the body of the instrument where they will experience a total radiation dose of less than 20 krads, it is anticipated that they will suffer negligible loss in reflectance or transmittance during the nominal 3 year mission lifetime of the POLAR spacecraft. Thus, we have experimentally demonstrated that  $\Pi$  multilayer thin films are sufficiently radiation resistant to allow their use in the high energy radiation environment of space. In a follow-up study, we will present a theoretical model of high energy radiation effects on multilayer thin films.

This work was supported by NASA grant NAG8-834 and NASA contract NAS8-38145.



## References

1. M. R. Torr, D. G. Torr, M. Zukic, J. Spann, and R. B. Johnson, "An Ultraviolet Imager for the International Solar-Terrestrial Physics Mission," submitted to Rev. Space Sci., Jan. 1993.
2. M. Zukic and D. G. Torr, "Multiple reflectors as narrow-band and broadband VUV filters," Appl. Opt. **31**, 1588-1596 (1992).
3. M. Zukic, D. G. Torr, J. Kim, J. F. Spann, and M. R. Torr, "Far ultraviolet filters for the ISTP UV Imager," Instrumentation for Planetary and Terrestrial Atmospheric Sensing, SPIE Proceedings Vol. 1745, 99-107 (1992).
4. P. Durand, Y. Farge and M. Lambert, "The creation of F centers in lithium fluoride between 77° and 600°K and their interpretation by a recombination model of interstitial-vacancies," J. Phys. Chem. Solids **30**, 1353-1374 (1969).
5. J. Becher, R. L. Kernell and C. S. Reft, "Proton-induced F-centers in LiF and MgF<sub>2</sub>," J. Phys. Chem. Solids **44**, 759-763 (1983).
6. D. F. Heath and P. A. Sacher, "Effects of a simulated high-energy space environment on the ultraviolet transmittance of optical materials between 1050 Å and 3000 Å," Appl. Opt. **5**, 937-943 (1966).
7. G. Hass and W. R. Hunter, "Laboratory experiments to study surface contamination and degradation of optical coatings and materials in simulated space environments," Appl. Opt. **9**, 2101-2110 (1970).
8. S. Majewski and M. K. Bently, "Gamma radiation induced damage effects in the transmission of barium fluoride and cesium fluoride fast crystal scintillators," Nucl. Instr.

- and Meth. **A260**, 373-376, (1987).
9. M. Murashita, H. Saitoh, K. Tobimatsu, M. Chiba, T. Hirose and F. Takasaki, "Performance and radiation damage of a BaF<sub>2</sub> calorimeter," Nucl. Instr. and Meth. **A243**, 67-76 (1986).
  10. M. T. Shetter and V. J. Abreu, "Radiation effects on the transmission of various optical glasses and epoxies," Appl. Opt. **18**, 1132-1133 (1979).
  11. C. A. Nicoletta and A. G. Eubanks, "Effect of simulated space radiation on selected optical materials," Appl. Opt. **11**, 1365-1370 (1972).
  12. C. S. Reft, J. Becher and R. L. Kernell, "Proton-induced degradation of VUV transmission of LiF and MgF<sub>2</sub>," Appl. Opt. **19**, 4156-4158 (1980).
  13. L. R. Canfield, G. Hass and J. E. Waylonis, "Further studies of MgF<sub>2</sub>-overcoated aluminum mirrors with highest reflectance in the vacuum ultraviolet," Appl. Opt. **5**, 45-50 (1966).

Table 1: Summary of results for all the filters, thin films, and substrates tested.

Film Type	Film Materials	Substrate	Reflectance Changes	Transmittance Changes
Single Layer	Al <sub>2</sub> O <sub>3</sub>	Fused Silica	None	None
Single Layer	BaF <sub>2</sub>	MgF <sub>2</sub>	None	None
Single Layer	CaF <sub>2</sub>	MgF <sub>2</sub>	None	See Figure 3
Single Layer	HfO <sub>2</sub>	MgF <sub>2</sub>	None	None
Single Layer	LaF <sub>3</sub>	MgF <sub>2</sub>	None	See Figure 2
Single Layer	MgF <sub>2</sub>	MgF <sub>2</sub>	None	None
Single Layer	SiO <sub>2</sub>	MgF <sub>2</sub>	None	None
Π Multilayer	BaF <sub>2</sub> /MgF <sub>2</sub>	MgF <sub>2</sub>	None	None
Π Multilayer	LaF <sub>3</sub> /MgF <sub>2</sub>	Fused Silica	None	None
None	None	Fused Silica	None	None
None	None	MgF <sub>2</sub>	None	See Figure 1

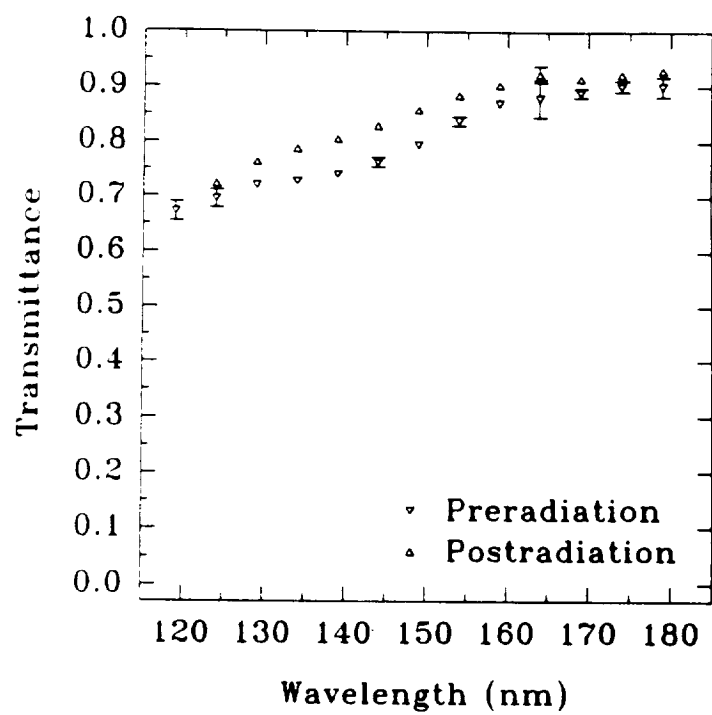
## Figure Captions

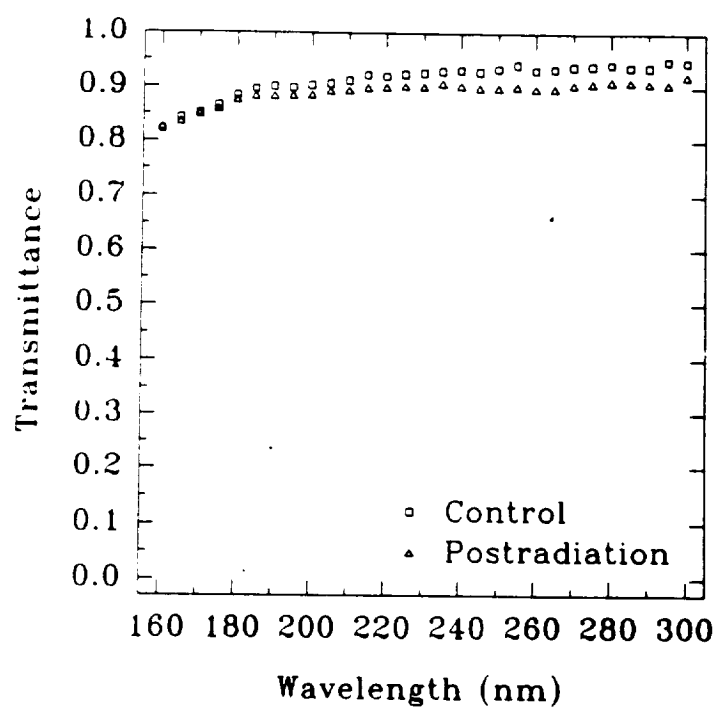
Figure 1: Transmission measurements for the uncoated  $\text{MgF}_2$  substrate. Comparison is shown in the 120 nm to 180 nm range before and after 250 krad of radiation exposure to the sample. The error bars represent one standard deviation.

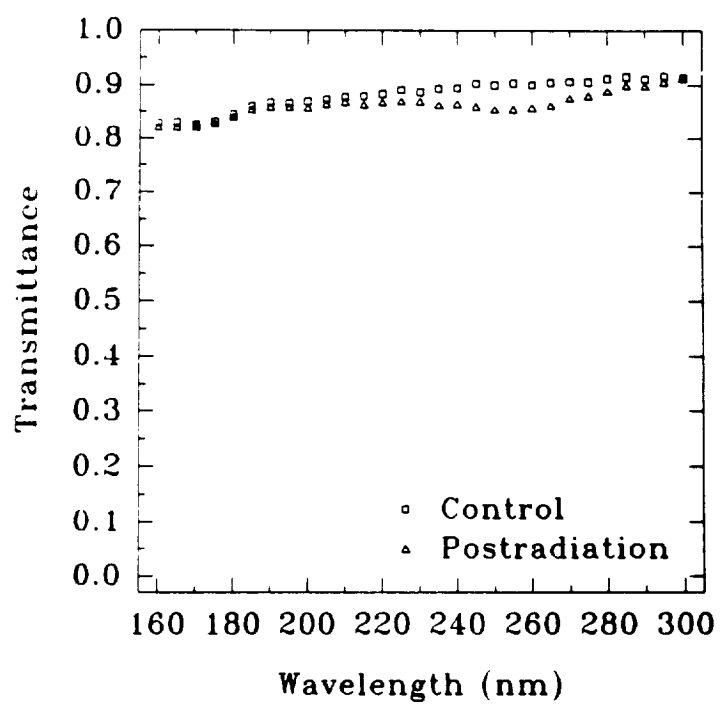
Figure 2: Transmission measurements for the  $\text{CaF}_2$  thin film on a  $\text{MgF}_2$  substrate. Comparison in the 160 nm to 300 nm range is between the radiation exposed sample and a control sample with no radiation exposure. The error bars represent one standard deviation.

Figure 3: Transmission measurements for the  $\text{LaF}_3$  thin film on a  $\text{MgF}_2$  substrate. Comparison in the 160 nm to 300 nm range is between the radiation exposed sample and a control sample with no radiation exposure. The error bars represent one standard deviation.

Figure 1, 5-22-77







**APPENDIX E**

“Use of FUV Auroral Emissions as Diagnostic Indicators”

Journal of Geophysical Research  
99, 383-388 (1994)



## Use of FUV auroral emissions as diagnostic indicators

G. A. Germany,<sup>1</sup> M. R. Torr,<sup>2</sup> D. G. Torr,<sup>3</sup> and P. G. Richards<sup>4</sup>

In an earlier study we modeled selected FUV auroral emissions (O I (1356 Å), N<sub>2</sub> Lyman-Birge-Hopfield (LBH) (1464 Å), and LBH (1838 Å)) to examine the sensitivity of these emissions and their ratios to likely changes in the neutral atmosphere. In this paper we extend that study to examine the dependence of these same emissions and their ratios on the shape of the energy distribution of the auroral electrons. In particular, we wish to determine whether changes in energy spectra might interfere with our determination of the characteristic energy. Modeled column-integrated emissions show relatively small (<30%) dependences on the shape and width of the incident energy spectrum, provided the average energy and total energy flux of the energy distribution are held constant. Long-wavelength FUV emissions, which are relatively unaffected by O<sub>2</sub> absorption losses, exhibit virtually no dependence on the shape of the incident energy distribution. Changes in ratios of FUV short- to long-wavelength emissions as a function of characteristic energy are much larger than those due to changes in energy distribution. As a result, the determination of characteristic energy using these emission ratios is relatively unambiguous. We also examine the relative intensities of the aurora and the dayglow for various conditions. The intensities of modeled FUV auroral emissions relative to the dayglow emissions are presented as a function of solar zenith angle and incident energy flux. Under certain conditions (energy flux  $\leq 1 \text{ erg cm}^{-2} \text{ s}^{-1}$  and solar zenith angle  $\leq 50^\circ$ ) the dayglow will be the limiting factor in the detection of weak auroras.

### INTRODUCTION

In a previous study, *Germany et al.* [1990] investigated the dependence of modeled far ultraviolet (FUV) atomic oxygen and N<sub>2</sub> Lyman-Birge-Hopfield (LBH) auroral emissions on likely uncertainties and anticipated changes in the neutral atmosphere. In this paper, we extend that study by examining the dependence of modeled FUV auroral emissions on the energy spectrum of the incident electron flux and by comparing the modeled FUV auroral emissions to anticipated underlying dayglow emissions.

*Germany et al.* [1990] modeled auroral emissions (O I (1356 Å), LBH (1464 Å), and LBH (1838 Å)) to evaluate their utility in extracting fundamental information about the incident auroral electrons. As an example of this utility, a ratio of the column intensities formed from either of the shorter-wavelength emissions and the LBH (1838 Å) emission (O I 1356/LBH 1838 or LBH 1464/LBH 1838) may be used to infer the characteristic energy of the incident auroral electrons. They also investigated the sensitivity of these emissions and their intensity ratios to changes in the modeled neutral atmosphere. The O I (1356 Å) to LBH (1838 Å) intensity ratio exhibits a greater dependence on the characteristic energy of the incident electrons than does the LBH (1838 Å) to LBH (1464 Å) intensity ratio. This is offset, however, by the

greater stability of the LBH emission ratio to changes in seasonal and solar cyclic activity.

We have evaluated the sensitivity of selected FUV auroral emissions to a variety of energy distributions. Since different physical processes lead to different energy distributions, there is not a single parameterization which applies to all situations. *Strickland et al.* [1983] examined the dependence of FUV auroral emissions on the choice of either a Gaussian or a Maxwellian incident energy spectrum. Here we extend that study by modeling auroral emissions resulting from incident energy distributions of different widths and shapes to determine whether changes in energy spectra might obscure, or render ambiguous, our determination of the incident characteristic energy from FUV emission ratios.

In addition, we investigate the relative intensities of modeled dayglow and auroral emissions as a function of solar activity levels and solar zenith angle. Since imaging in the far ultraviolet avoids problems with exceedingly bright visible dayside scattering, the detection limit is set by the brightness of the superimposed dayglow emission.

### EMISSION MODELS

The auroral code used to compute the auroral intensities is a two-stream model described in an earlier paper [*Richards and Torr*, 1990]. A two-stream model can serve well in cases such as the present which emphasize energy deposition and column intensities and in which detailed knowledge of pitch angle distributions is not crucial [*Stamnes*, 1981]. As noted by *Richards and Torr* [1990], our auroral code gives excellent agreement with the more detailed multistream model of *Strickland et al.* [1983] and *Daniell and Strickland* [1986].

The dayglow emissions are computed using our field line interhemispheric plasma (FLIP) model optimized for airglow studies [*Torr et al.*, 1990]. Emission cross sections for N<sub>2</sub> LBH are those of *Ajello and Shemansky* [1985]. The O(<sup>3</sup>S) 1356 excitation cross section is that of *Stone and Zipf* [1974] scaled by the same factor of 3.1 by which their 1304-Å emission

<sup>1</sup>Center for Space Plasma and Aeronomic Research, University of Alabama, Huntsville.

<sup>2</sup>NASA Marshall Space Flight Center, Huntsville, Alabama.

<sup>3</sup>Department of Physics, Center for Space Plasma and Aeronomic Research, University of Alabama, Huntsville.

<sup>4</sup>Computer Science Department, Center for Space Plasma and Aeronomic Research, University of Alabama, Huntsville.

cross sections were reduced by *Zipf and Erdman* [1985]. Dissociative excitation of  $O_2$  by electrons is a significant source of  $O\ I$  (7774 Å) emission for hard auroral spectra [*Strickland et al.*, 1989]. Since the same mechanism could also serve as an additional source of 1356-Å emission, we modeled the effects of this additional source, using the cross sections of *Wells et al.* [1971] revised to reflect the lifetime determination of *Wells and Zipf* [1974]. We find that the increase in the auroral 1356-Å column intensity with the additional excitation source is about 30% at 10 keV. The production of 1356-Å dayglow by photoelectron dissociative excitation of  $O_2$  is considerably smaller, since photoelectrons are typically produced with energies below that of the peak  $e+O_2$  cross section. For completeness we include the dissociative excitation source in the auroral 1356-Å emissions modeled below.

For the present study, both the auroral and the FLIP codes used the MSIS-86 neutral atmosphere [*Hedin*, 1987]. The model parameters differ slightly between the two studies reported below and will be given separately in each section. When necessary to model emissions for a range of activity levels, we vary the  $F_{10.7}$  and  $A_p$  indices used in our emission models. The range of modeled activity levels is given in Table 1.

We model three emissions as seen from a nadir-looking orbiting platform:  $O\ I$  (1356 Å), LBH (1,1) (1464 Å), and LBH (2,8) (1838 Å). These emissions are chosen as representative of the principal FUV emissions available to space-based observations and as potential remote diagnostics. The prominent  $O\ I$  (1304 Å) emission is not included because it is optically thick and undergoes multiple scattering. The 1356-Å emission does undergo multiple scattering, but its efficiency is relatively small [*Strickland and Anderson*, 1983] and is ignored for the nadir-looking geometry considered here. In photometric imaging, the  $O\ I$  (1356 Å) emission is not resolved from the LBH (3,0) (1354 Å) emission which can be a significant contributor to a measured 1356-Å signal (Figure 1). Hence we also model the LBH (1354 Å) emission. Where appropriate, we present results for both the  $O\ I$  (1356 Å) emission alone and for the summed  $O\ I$  (1356 Å) and LBH (1354 Å) emissions. In practice, we correct the signal at 1356 Å for the LBH (3,0) band by measuring the longer-wavelength LBH bands separately.

#### DEPENDENCE ON INCIDENT ENERGY DISTRIBUTION

We studied the dependence of FUV auroral emissions on selected energy distributions for the incident auroral electron flux by varying the energy spectrum and comparing resultant modeled emissions. In addition to varying the functional dependence of the energy distribution, we looked at the effects of varying its width and its low-energy behavior.

We first modeled auroral emissions using either a Gaussian or Maxwellian energy distribution. Model parameters which might affect the modeled intensities, such as energy flux and average energy, were held constant throughout this study.

TABLE 1. Input Parameters

	Activity		
	Minimum	Moderate	Maximum
$F_{10.7}$ cm flux index	75	110	200
$A_p$ magnetic activity index	4	20	100

Furthermore, care was taken to prevent high-energy truncation of the broader distributions due to either improper altitude or energy limits within the model. Emissions were modeled for a 1 erg cm<sup>-2</sup> s<sup>-1</sup> incident energy flux; the moderate activity level from Table 1; geographic latitude = 60°; geographic longitude = 0°; solar apparent time = 0.0 hours, and day = 173.

After *Daniell and Strickland* [1986], we define the Gaussian energy distribution as

$$f_{\text{Gauss}}(E) = \frac{Q}{\pi^{1.5} W E_c^2} \exp\left[-\left(\frac{E-E_c}{W E_c}\right)^2\right] \quad (1)$$

and the Maxwellian distribution by

$$f_{\text{Max}}(E) = \frac{QE}{2\pi E_c^3} \exp\left[-\left(\frac{E}{E_c}\right)\right] \quad (2)$$

where  $Q$  sets the incident energy flux,  $W$  sets the width of the Gaussian distribution, and  $E_c$  is the characteristic energy of the incident distribution. The Gaussian scale parameter  $W$  is held constant at 0.25 for comparison with the Maxwellian distribution. The choice of this parameter is not important in itself, as we are not trying to match a particular auroral energy distribution at this point. The average energy  $\langle E \rangle$  of an energy distribution  $f(E)$  is taken to be

$$\langle E \rangle = \frac{\int E f(E) dE}{\int f(E) dE} \quad (3)$$

Figure 2 shows the two distributions for an average energy of 5 keV and a 1 erg cm<sup>-2</sup> s<sup>-1</sup> incident flux. The Maxwellian distribution is asymmetric, and its average energy will therefore not correspond to its characteristic energy (energy at which the distribution is maximum). Rather, the average energy of the Maxwellian distribution is equal to twice its characteristic energy. On the other hand, the Gaussian distribution is symmetric, and its average energy is thus equal to its characteristic energy. The average, not the characteristic, energy was held constant when comparing distributions.

In Figure 3 we show the ratio of the auroral column intensities as calculated with the Gaussian and Maxwellian distributions. The longer-wavelength LBH (1838 Å) emission is virtually unaffected (less than 5%) by the choice of energy

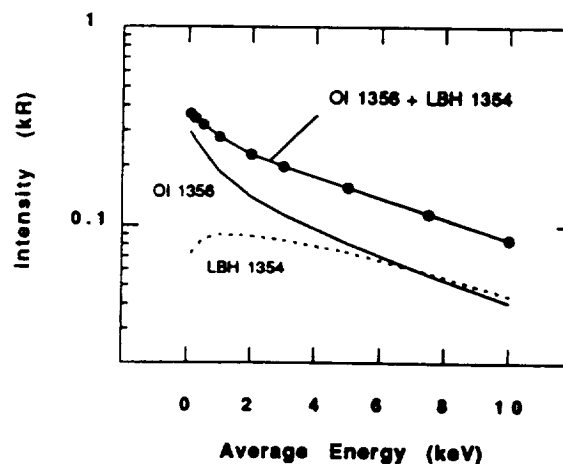


Fig. 1.  $O\ I$  1356 and LBH 1354 Å auroral emissions for a 1 erg cm<sup>-2</sup> s<sup>-1</sup> incident energy flux and a moderate activity level as given in Table 1.

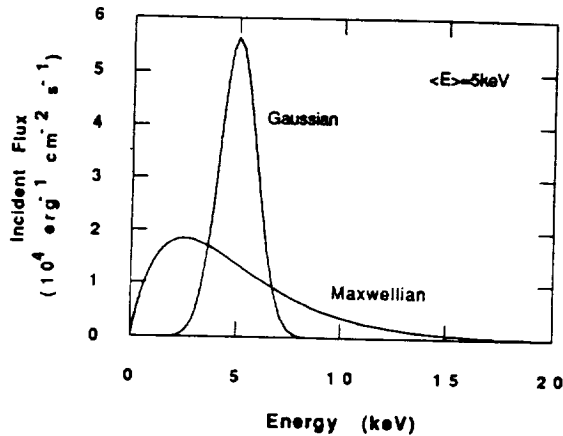


Fig. 2. Gaussian and Maxwellian energy distributions with a 5-keV average energy and a  $1 \text{ erg cm}^{-2} \text{ s}^{-1}$  incident energy flux.

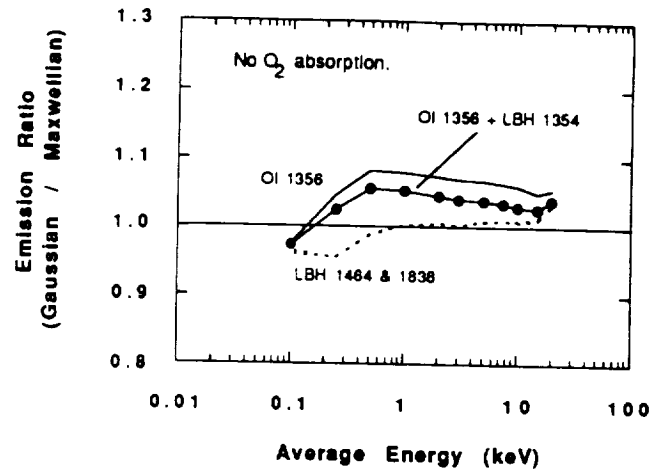


Fig. 4. Same as Figure 2 except without  $\text{O}_2$  absorption.

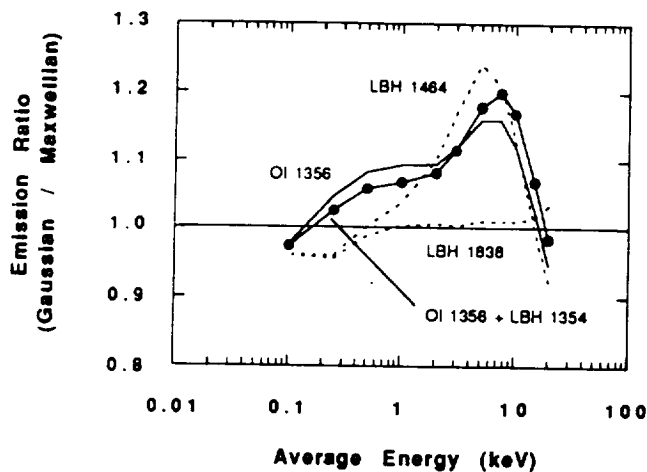


Fig. 3. Ratio of integrated column brightnesses calculated from a Gaussian energy distribution to those from a Maxwellian distribution.

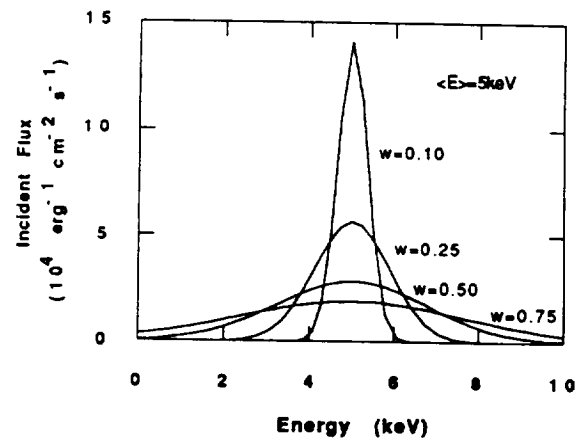


Fig. 5. Gaussian energy distributions with varying widths. Each distribution has an average energy of 5 keV and an energy flux of  $1 \text{ erg cm}^{-2} \text{ s}^{-1}$ .

distribution. Because of  $\text{O}_2$  absorption, the shorter-wavelength emissions exhibit significant variation with energy distribution. When the  $\text{O}_2$  absorption mechanism is disabled within the auroral code, we find that the LBH (1464 Å) (and LBH (1354 Å)) variations are entirely due to  $\text{O}_2$  absorption (Figure 4). The O I (1356 Å) emission, however, is only partially dependent on the effects of  $\text{O}_2$  absorption.

The differences between modeled emissions from the Gaussian and Maxwellian distributions are due, in part, to the differences in the functional dependence of the two energy distributions on the incident energy, i.e., their shapes. In addition, however, the Maxwellian distribution is broader (in energy) than the Gaussian distribution. A wider energy distribution will contribute relatively greater numbers of both high- and low-energy electrons than a more narrow distribution. Since much of the energy dependence of FUV auroral emissions is due to absorption by  $\text{O}_2$ , some of the differences seen in Figure 3 can be expected to be due solely to the relative widths of the energy distributions.

Accordingly, we selected a single distribution, a Gaussian, and modeled auroral emissions which differed only in the width of the distribution used. The width of the Gaussian distribution was varied by adjusting the width parameter  $W$  in equation (1) from 0.1 to 0.75. Sample distributions for an average energy of 5 keV are shown in Figure 5. Again, each distribution is constrained to have an energy flux of  $1 \text{ erg cm}^{-2} \text{ s}^{-1}$ . Figure 6

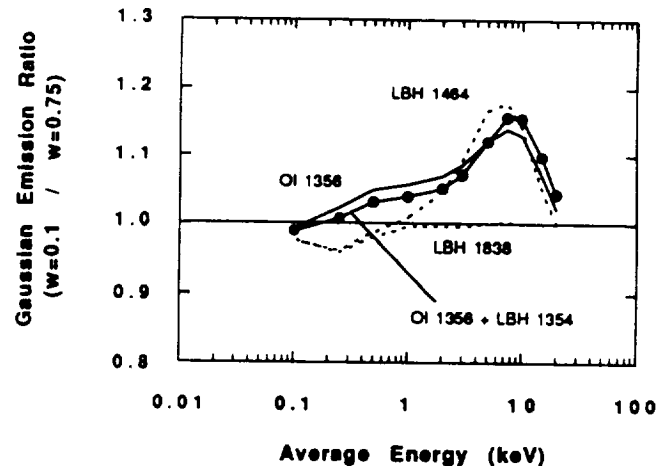


Fig. 6. Ratio of integrated column brightnesses calculated from a Gaussian energy distribution with  $W=0.1$  to those with  $W=0.75$ .

shows column intensity ratios for  $W=0.75$  and  $W=0.1$ . Note that the behavior is similar to that of Figure 3.

We also studied auroral emissions using two arbitrary energy distributions. The intent of this comparison was to study the modeled emissions from energy distributions with quite different functional dependences and widths but with fixed average energies. The first of these arbitrary distributions was

a step function which extended from 0 eV to a maximum energy equal to twice its average energy. The second distribution was a very narrow ( $W=0.06$ ) Gaussian distribution. Both distributions, labeled "wide" and "narrow", are shown in Figure 7 for an average energy of 5 keV and a  $1 \text{ erg cm}^{-2} \text{ s}^{-1}$  incident flux. The choice of  $W$  for the narrow distribution results in a distribution whose width (full width at half maximum) is only 10% of its characteristic energy. With this combination of energy distributions, the wide distribution is about 20 times broader than the narrow distribution. Figure 8 shows the ratio of column emissions modeled with the two distributions. Despite the dissimilarities in energy distribution, the results shown are similar to those in Figures 3 and 6. Each of these studies implies that for a fixed average energy and energy flux, the width of the energy distribution is more significant than its shape in determining modeled FUV auroral column intensities.

Previous work has pointed out the significance of the low-energy part of the energy spectrum in modeling visible emissions. For example, Meier *et al.* [1989] noted that measured energy distributions often have significantly more low-energy electrons than are provided by either the Gaussian or Maxwellian distributions given here by equations (1) and (2). This low-energy tail adds little to the total energy flux but should enhance  $F$  region emissions. The addition of the low-energy tail is not a significant emission source for the FUV emissions modeled here and results in changes of less than about 5%.

#### COMPARISON TO AURORAL DAYGLOW

The second task of this study was to compare the intensity of modeled auroral emissions with that of anticipated dayglow emissions as they would be seen from space for the features of interest here. Though FUV auroral images have served as remote diagnostics in a number of studies [e.g., Robinson *et al.*, 1989, 1992], comparatively little work has been done for images seen against a full midday airglow background. We have recently developed a FUV imager for the Global Geospace Science mission (M. R. Torr *et al.*, An ultraviolet imager for the International Solar-Terrestrial Physics Mission, submitted to *Reviews in Space Science*, 1993) which incorporates ultraviolet filters both sufficiently narrow to allow separation of the FUV features of interest and with approximately 10 orders of magnitude blocking throughout the visible and near infrared. We here assess the in-band competing elements of

aurora and airglow by modeling FUV auroral emissions against a superimposed dayglow as a function of solar zenith angle and incident energy flux.

Since the incident auroral flux is highly dynamic, individual measurements of incident energy fluxes may span a large range. For our study we desire an estimate of average energy fluxes coupled with an estimate of their anticipated frequency of occurrence. Such a study has been reported by Hardy *et al.* [1985] in which they analyzed data from two Defense Meteorological Satellite Program satellites as well as the Satellite Test Program P78-1 satellite. They reported average energy fluxes ( $\text{keV cm}^{-2} \text{ s}^{-1} \text{ sr}^{-1}$ ) as a function of magnetic local time, magnetic latitude, and  $Kp$  for a period from September 1977 to August 1980. We can use these results to estimate the average incident energy flux ( $\text{ergs cm}^{-2} \text{ s}^{-1}$ ) in specific parts of the auroral oval. The average energy flux reported by Hardy *et al.* [1985] for  $Kp \leq 3$  was less than about  $10 \text{ ergs cm}^{-2} \text{ s}^{-1}$  in the midnight sector and less than about  $3 \text{ ergs cm}^{-2} \text{ s}^{-1}$  in the noon sector. For the roughly 20% of analyzed data in which  $Kp$  exceeded 3, the average energy flux rose to about  $25 \text{ ergs cm}^{-2} \text{ s}^{-1}$  in the midnight sector but stayed relatively constant in the noon sector.

In a similar study, Spiro *et al.* [1982] analyzed data from the Low Energy Electron experiments on the Atmosphere Explorer C and D satellites from January 1974 to April 1976. They sorted their data by both  $Kp$  and the auroral electrojet index ( $AE$ ) but presented detailed tabular results only for the  $AE$  index. They found that over 90% of their data occurred for values of  $AE$  less than 600. Within this selection, the average energy flux was less than about  $6 \text{ ergs cm}^{-2} \text{ s}^{-1}$  in the midnight sector and less than about  $4 \text{ ergs cm}^{-2} \text{ s}^{-1}$  in the noon sector. The higher-activity cases showed an increase to about  $9 \text{ ergs cm}^{-2} \text{ s}^{-1}$  for the midnight sector with no increase in the noon sector. This is essentially in agreement with Hardy *et al.* [1985], though the latter reported higher fluxes in the midnight sector.

We have modeled incident auroral fluxes as Gaussian distributions ( $W=0.25$ ) with an incident energy flux of 1, 5, and  $10 \text{ ergs cm}^{-2} \text{ s}^{-1}$ . Characteristic energies between 0.5 and 10 keV were used for the incident auroral electrons. Local ionospheric conditions were modeled with the FLIP model using a flux tube characterized by an  $L$  shell of 5 for midsummer

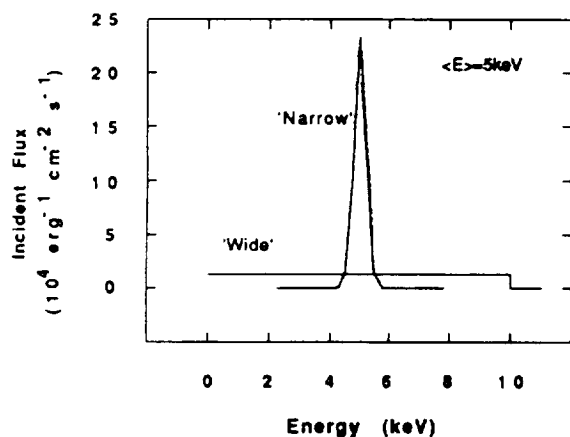


Fig. 7. "Narrow" and "wide" energy distributions with a 5-keV average energy and a  $1 \text{ erg cm}^{-2} \text{ s}^{-1}$  incident energy flux.

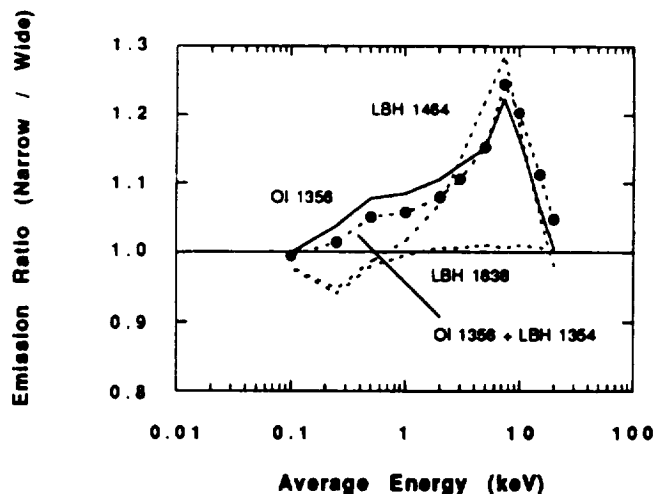


Fig. 8. Ratio of integrated column brightnesses calculated from the narrow energy distribution shown in Fig. 7 to those from the wide distribution.

conditions (day=173). The solar zenith angle varied from about  $50^\circ$  at local noon to  $83^\circ$  near local midnight. To monitor the variability of the combined auroral/dayglow intensity as a function of solar cyclic activity, the  $F_{10.7}$  and  $A_p$  input parameters were varied as shown in Table 1. The initial case modeled here (solar zenith angle of  $51^\circ$  at  $L=5$ , local summer noon) represents something of a worst case as auroras will typically lie to higher latitudes and hence larger solar zenith angles and less dayglow. The addition of the LBH (1354 Å) emission to the O I (1356 Å) has little effect on the conclusions drawn from this part of the study. Therefore we omit the addition of the LBH (1354 Å) in the remainder of the figures.

Figure 9 shows a comparison of noon airglow and auroral emissions, where the latter have been computed for 1, 5, and 10

ergs  $\text{cm}^{-2} \text{s}^{-1}$  cases. The dayglow is strongly dependent on the selected activity level; the auroral is much less dependent. (For each wavelength, both the dayglow and the three auroral cases are modeled for three distinct activity levels.)

For solar zenith angles of  $\leq 51^\circ$  the dayglow intensities exceed those of a 1 erg  $\text{cm}^{-2} \text{s}^{-1}$  aurora. Weak auroras with high characteristic energies would be the most difficult to detect at noon. Fortunately, dayside auroras tend to be caused by soft cusp particles. Figure 10 shows the ratio of 1356-Å aurora to airglow for the 5 ergs  $\text{cm}^{-2} \text{s}^{-1}$  case for this same location as a function of solar zenith angle. As would be expected, the ratio is a strong function of solar zenith angle because of the airglow dependence on the latter.

## DISCUSSION

FUV auroral emissions have been modeled as a function of several different incident electron energy distributions. Our choice of distributions was not necessarily realistic; the distributions were chosen to illustrate extremes of shape and width. It is significant, in light of these choices, that a change of energy distribution affects the column emissions by less than 30%. Regardless of the energy distributions modeled, we see that the differences in resulting emissions are governed primarily by the average energy of the distributions and the relative widths of the distributions. Therefore, much of the behavior seen in Figures 3, 6, and 8 can be discussed solely in terms of the relative widths of the energy distributions. This is principally due to the predominate influence of  $\text{O}_2$  absorption in determining the energy dependence of the FUV auroral emission.

The relative width of the energy distribution affects the modeled emissions via either a low-energy or a high-energy mechanism, with the distinction between the two being at an average incident energy of about 10 keV. Below 10 keV, FUV auroral emissions generated by the broader distribution experience a greater loss at the low-altitude edge of the emission altitude profile and produce subsequently reduced column intensities. For average energies above 10 keV,  $\text{O}_2$  absorption dominates, and only those emissions due to the lower-energy part of the distribution are seen. (The emissions from the higher-energy electrons are totally absorbed.) Longer-wavelength emissions, such as LBH (1838 Å), do not experience  $\text{O}_2$  absorption and are relatively unaffected by the choice of incident energy distribution. The O I (1356 Å)

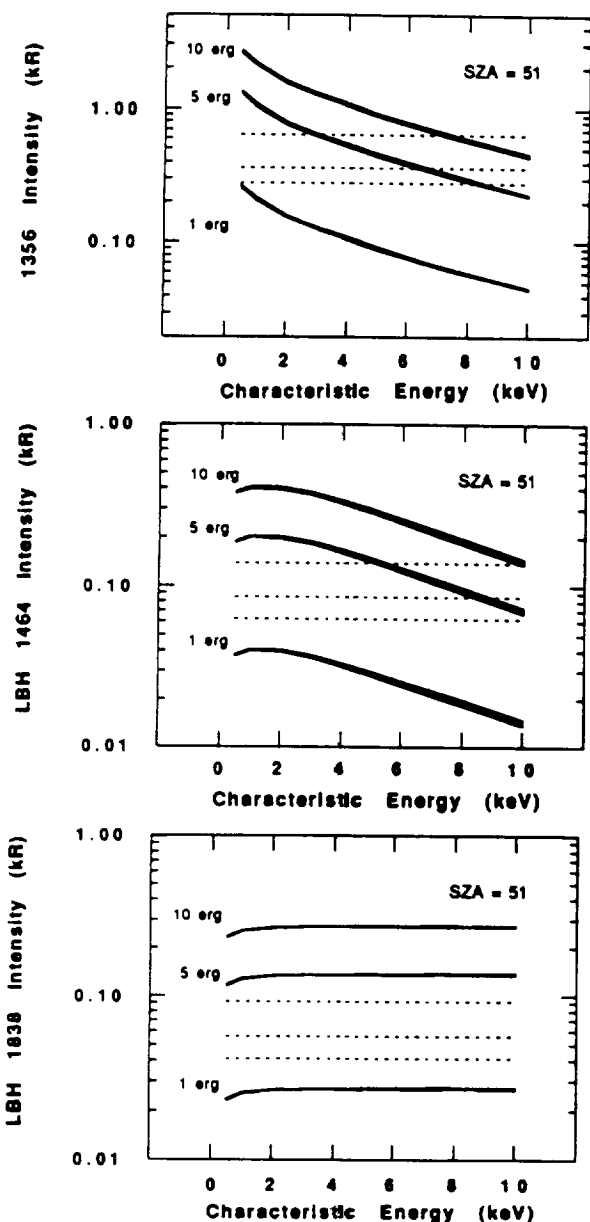


Fig. 9. Integrated column brightnesses for auroral (solid) and dayglow (dashed) emissions with a solar zenith angle of  $51^\circ$ . All emissions are given for the range of activity levels defined in Table 1. Within each set, the largest values are obtained for maximum activity conditions. The auroral emissions are modeled for 1, 5, and 10 ergs  $\text{cm}^{-2} \text{s}^{-1}$  incident energy fluxes: (a) O I 1356, (b) LBH 1464, and (c) LBH 1838.

a

b

c

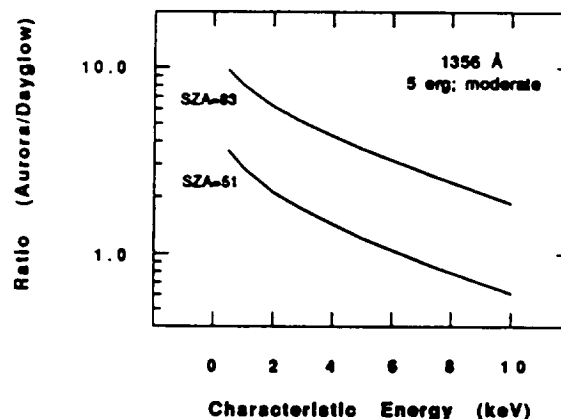


Fig. 10. Ratio of modeled dayglow and auroral 1356-Å emissions as a function of solar zenith angle for a 5 ergs  $\text{cm}^{-2} \text{s}^{-1}$  energy flux and a moderate activity level as given in Table 1.

emission exhibits an additional dependence due its altitude distribution. A broad energy distribution will result in reduced 1356-Å production, relative to a narrow distribution, because of increased collisional competition with other neutral targets.

As noted above, the magnitude of the changes in column intensities with choice of energy distribution is less than about 30%. The dependence of modeled FUV auroral emissions on energy distribution is therefore much less than their dependence on characteristic (or average) energy. The characteristic energy extracted from FUV color ratios should therefore be relatively unambiguous, since such determinations will not be dependent on an exact knowledge of the incident energy spectrum.

Typical aurora have also been modeled with concurrent dayglow emissions as a function of solar zenith angle, solar activity levels, total electron energy flux, and incident characteristic energy. The ratio of auroral to dayglow emissions is a strong function of solar zenith angle because of the dayglow dependence on solar zenith angle. For the FUV emissions of interest here, the dayglow is the strongest competing background and under certain conditions (energy flux  $\leq 1$  erg cm<sup>-2</sup> s<sup>-1</sup> and solar zenith angle  $\leq 50^\circ$ ) will be the limiting factor in the detection of weak auroras.

**Acknowledgments.** This work was supported by NASA grants NAGW-996 and NAG8-834, NASA contract NAS8-38145, and NSF grant ATM-9018165 to the University of Alabama in Huntsville. The authors acknowledge the helpful comments of the reviewers.

The Editor thanks D. Shemansky and another referee for their assistance in evaluating this paper.

#### REFERENCES

- Ajello, J. M., and D. E. Shemansky, A reexamination of important N<sub>2</sub> cross sections by electron impact with application to the dayglow: The Lyman-Birge-Hopfield band system and N I (1119.99 nm), *J. Geophys. Res.*, **90**, 9845, 1985.
- Daniell, R. E., Jr., and D. J. Strickland, Dependence of auroral middle UV emissions on the incident electron spectrum and neutral atmosphere, *J. Geophys. Res.*, **91**, 321, 1986.
- Germany, G. A., M. R. Torr, P. G. Richards, and D. G. Torr, The dependence of modeled O I 1356 and N<sub>2</sub> Lyman Birge Hopfield auroral emissions on the neutral atmosphere, *J. Geophys. Res.*, **95**, 7725, 1990.
- Hardy, D. A., M. S. Gussenhoven, and E. Holeman, A statistical model of auroral electron precipitation, *J. Geophys. Res.*, **90**, 4229, 1985.
- Hedin, A. H., MSIS-86 thermospheric model, *J. Geophys. Res.*, **92**, 4649, 1987.
- Meier, R. R., D. J. Strickland, J. H. Hecht, and A. B. Christensen, Deducing composition and incident electron spectra from ground-based auroral optical measurements: A study of auroral red line processes, *J. Geophys. Res.*, **94**, 13,541, 1989.
- Richards, P. G., and D. G. Torr, Auroral modeling of the 3371 Å emission rate: Dependence on characteristic electron energy, *J. Geophys. Res.*, **95**, 10,337, 1990.
- Robinson, R. M., R. R. Vondrak, J. D. Craven, L. A. Frank, and K. Miller, A comparison of ionospheric conductances and auroral luminosities observed simultaneously with the Chatanika radar and the DE 1 auroral imagers, *J. Geophys. Res.*, **94**, 5382, 1989.
- Robinson, R., T. Dabbs, J. Vickrey, R. Eastes, F. Del Greco, R. Huffman, C. Meng, R. Daniell, D. Strickland, and R. Vondrak, Coordinated measurements made by the Sondrestrom radar and the Polar Bear ultraviolet imager, *J. Geophys. Res.*, **97**, 2863, 1992.
- Spiro, R. W., P. H. Reiff, and L. J. Maher, Jr., Precipitating electron energy flux and auroral zone conductances -- An empirical model, *J. Geophys. Res.*, **87**, 8215, 1982.
- Stamnes, K., On the two-stream approach to electron transport and thermalization, *J. Geophys. Res.*, **86**, 2405, 1981.
- Stone, E. J., and E. C. Zipf, Electron-impact excitation of the 3S° and 5S° states of atomic oxygen, *J. Chem. Phys.*, **60**, 4237, 1974.
- Strickland, D. J., and D. E. Anderson, Jr., Radiation transport effects on the O I (1356 Å) limb intensity profile in the dayglow, *J. Geophys. Res.*, **88**, 9260, 1983.
- Strickland, D. J., J. R. Jasperse, and J. A. Whalen, Dependence of auroral FUV emissions on the incident electron spectrum and neutral atmosphere, *J. Geophys. Res.*, **88**, 8051, 1983.
- Strickland, D. J., R. R. Meier, J. H. Hecht, and A. B. Christensen, Deducing composition and incident electron spectra from ground-based auroral optical measurements: Theory and model results, *J. Geophys. Res.*, **94**, 13527, 1989.
- Torr, M. R., D. G. Torr, P. G. Richards, and S. P. Yung, Mid- and low-latitude model of thermospheric emissions, I, O\*(2P) 7320 Å and N<sub>2</sub>(2P) 3371 Å, *J. Geophys. Res.*, **95**, 2,1147, 1990.
- Wells, W. C., and E. C. Zipf, Lifetime of the metastable 5S<sup>0</sup> state of atomic oxygen, *Phys. Rev.*, **A9**, 568, 1974.
- Wells, W. C., W. L. Borst, and E. C. Zipf, Absolute cross section for the production of O(5S) by electron impact dissociation of O<sub>2</sub>, *Chem. Phys. Lett.*, **12**, 288, 1971.
- Zipf, E. C., and P. W. Erdman, Electron impact excitation of atomic oxygen: Revised cross sections, *J. Geophys. Res.*, **90**, 11,087, 1985.
- G. A. Germany, Center for Space Plasma and Aeronomic Research, University of Alabama, Huntsville, AL 35899.
- P. G. Richards, Computer Science Department, Center for Space Plasma and Aeronomic Research, University of Alabama, Huntsville, AL 35899.
- D. G. Torr, Department of Physics, Center for Space Plasma and Aeronomic Research, University of Alabama, Huntsville, AL 35899.
- M. R. Torr, NASA Marshall Space Flight Center, Mail Code JA01, Huntsville, AL 35812.

(Received September 24, 1992;  
revised August 6, 1993;  
accepted August 13, 1993.)

**APPENDIX F**

**“Determination of Ionospheric Conductances  
From FUV Auroral Emissions**

**Presented by Dr. Glynn A. Germanny**

**at**

**AGU Fall Meeting  
December 9-13, 1991  
San Francisco, California**

AGU Fall Meeting  
December 9-13, 1991  
San Francisco, CA

**Determination of Ionospheric Conductances From FUV Auroral Emissions**

G A Germany (Center for Space Plasma and Aeronomic Research, University of Alabama in Huntsville, Huntsville, AL 35899)

D G Torr (CSPAR/Physics Department, University of Alabama in Huntsville, Huntsville, AL 35899)

P G Richards (CSPAR/Computer Science Dept., University of Alabama in Huntsville, Huntsville, AL 35899)

M R Torr (Space Science Laboratory, Marshall Space Flight Center, Huntsville, AL 35812)

We have studied the behavior of modeled auroral Hall and Pedersen conductivities as a function of auroral electron flux and atmospheric composition. We show that the column integrated Hall and Pedersen conductivities may be determined from a single measurement of two FUV auroral LBH emissions: LBH 1464 Å and LBH 1838 Å. The dependence of the determined conductivities on incident characteristic energy, total energy flux, changes in solar activity levels, and arbitrary perturbations of the individual neutral components (O, O<sub>2</sub>, N<sub>2</sub>) have been studied. The conductivity determinations are stable with respect to changes in levels of solar activity and against changes in the neutral atmospheric composition. The incident energy flux is also provided by the LBH 1838 Å emission. Thus the two auroral LBH emissions are sufficient to determine the column integrated conductivities.



## **APPENDIX G**

89

**“Determination of Ionospheric Conductivities  
From FUV Auroral Emissions”**

**Submitted to  
Journal of Geophysical Research**

**DETERMINATION OF IONOSPHERIC CONDUCTIVITIES FROM FUV AURORAL EMISSIONS**

**G. A. Germany<sup>1</sup>, D. G. Torr<sup>1</sup>, P. G. Richards<sup>1</sup>, M. R. Torr<sup>2</sup>, and S. John<sup>1</sup>**

**<sup>1</sup> University of Alabama in Huntsville  
Huntsville, Alabama 35899**

**<sup>2</sup> NASA Marshall Space Flight Center  
Huntsville, Alabama 35812**

**Journal of Geophysical Research**

**Submitted January 1994**

**Revised May 1994**

### Abstract

The purpose of this paper is to examine the viability of using LBH emission ratios to infer auroral conductances and to quantify the strengths and weaknesses of this technique. We show that column-integrated Hall and Pedersen conductances may be determined from a single remote measurement of a pair of auroral LBH emissions, one in the region of strong O<sub>2</sub> absorption (1464 Å) and one lying outside of this region (1838 Å). The dependence of the determined conductivities on incident average energy, total energy flux, and changes in solar and magnetic activity levels is examined. We show that, for energies above 5 keV, auroral conductances may be scaled by the square root of the incident energy flux with errors less than about 20%. For lower energies, however, the scaling may deviate significantly from a power of 0.5. We provide appropriate scaling factors as a function of average energy. We also note that the choice of either a Gaussian or Maxwellian distribution can significantly affect low-energy (<1 keV) conductance calculations. Finally, we quantify the conditions under which the mean energy of a Gaussian energy distribution may differ significantly from the characteristic energy.

## INTRODUCTION

Knowledge of ionospheric conductivities is central to an understanding of the coupled nature of the ionosphere, thermosphere, and magnetosphere. This is reflected in models of ionospheric electrodynamics and convection requiring conductance distributions [e.g., *Richmond and Kamide*, 1988; *Rasmussen and Schunk*, 1987; *Senior and Blanc*, 1984; *Spiro and Wolf*, 1984; *Roble et al.*, 1982]. Considerable effort has been directed toward modeling ionospheric conductances from EUV solar illumination, nocturnal sources, and auroral precipitation [see, for example, *Moen and Brekke*, 1993; *Brekke and Hall*, 1988; *Rasmussen et al.*, 1988; and the reviews by *Brekke and Moen*, 1993 and *Reiff*, 1984]. Conductivities have been inferred from ground-based radar observations by a number of investigators, including *Robinson et al.* [1987, 1985]; *Robinson and Vondrak* [1984]; and *Vickrey et al.* [1981, 1982]. Satellite data is commonly used to determine conductances [e.g., *Watermann et al.*, 1993; *Fuller-Rowell and Evans*, 1987; *Vondrak and Robinson*, 1985; *Wallis and Budzinski*, 1981], with many studies featuring satellite overflights of ground-based facilities.

A particular difficulty in modeling conductances from auroral precipitation is proper accounting of the high temporal and spatial variability in the auroral zone, while at the same time mapping its global morphology. This difficulty can potentially be overcome by using images of the auroral region taken from space. For example, auroral images from Dynamics Explorer have been used to infer ionospheric conductances [*Robinson et al.*, 1989; *Kamide et al.*, 1986]. In addition, *Robinson et al.* [1992] and *Basu et al.* [1993] used FUV emissions measured by the AIRS instrument on the Polar BEAR satellite [*Meng and Huffman*, 1987; *Schenkel and Ogorzalek*, 1987] to infer *E* region electron density profiles.

A key to remote determination of auroral conductances by optical methods is the ability to characterize the incident auroral flux. Since the resultant column intensities are relatively

insensitive to choice of energy distribution [e.g., *Germany et al.*, 1994] the principal task is to estimate the energy flux and characteristic energy. *Rees and Luckey* [1974] showed that measurements of the 6300 Å emission of atomic oxygen and the 4278 Å emission of ionized molecular nitrogen could be used to infer the characteristic energy of the incident auroral particle flux. In this technique, the energy dependence is provided by the collisional deactivation of the 6300 Å emission at lower altitudes. *Strickland et al.* [1983] demonstrated the same capabilities using FUV auroral emissions. In particular, they proposed the use of the O I (1356 Å) and N<sub>2</sub> Lyman-Birge-Hopfield (LBH) emissions as remote diagnostics of the auroral process. Instead of quenching mechanisms, the FUV technique relied on absorption of O<sub>2</sub> at lower altitudes to supply an energy dependence. The potential of using FUV emissions from the Viking satellite as remote measures of characteristic energy was examined by *Steele et al.* [1992]. They found only a weak dependence on energy, but they were only able to examine energies below 1.4 keV. *Robinson et al.* [1992] compared electron density measurements from the Sondrestrom radar with electron densities inferred from O I (1356 Å) and N<sub>2</sub><sup>+</sup> (3914 Å) emissions observed by AIRS and found good agreement between the measured and inferred profiles. Since their method depends on a visible emission, it cannot be used for sunlit regions because of the intense Rayleigh scattering. To allow sunlit observations, *Strickland et al.* [1983] proposed the use of two FUV emissions, O I (1356 Å) and LBH (1273 Å), as diagnostics.

*Germany et al.* [1990] examined the stability of FUV emission ratios formed from atomic oxygen and LBH emissions as a function of likely changes in the neutral atmosphere. They found that emission ratios formed from the O I (1356 Å) emission varied significantly with seasonal and solar cyclic variations. On the other hand, emission ratios employing long- and short-wavelength LBH emissions were much less sensitive to changes in the neutral atmosphere. Furthermore, blending of the O I (1356 Å) and LBH (1354 Å) emissions represents a serious observational difficulty. Consequently, the LBH

emission ratios are potentially more valuable as remote diagnostics of the incident auroral flux than similar ratios using the O I (1356 Å) emission. *Germany et al.* [1994] examined the use of FUV emission ratios as remote diagnostics as a function of incident energy distribution. They found that the intensity of modeled FUV emissions are governed principally by the mean energy and relative width of the energy distribution. Column-integrated intensities are relatively insensitive (<30%) to changes in the actual functional form, i.e., the shape, of the energy distribution. Consequently, the LBH emission ratio can be used as remote diagnostics of auroral flux without *a priori* knowledge of the energy distribution. *Robinson et al.* [1987] noted similar results for auroral conductances, i.e., they are primarily dependent on the mean energy and energy flux, and less sensitive to the energy distribution.

This paper is a continuation of our previous examinations of the utility of LBH emission ratios as remote diagnostics of auroral processes. Here, we examine the relationship between FUV LBH auroral emissions and ionospheric conductances due to auroral precipitation. To our knowledge, this is the first time the LBH emission ratio has been used to infer auroral conductances. It is the purpose of this paper to examine the viability of using LBH emission ratios to infer auroral conductances and to quantify the strengths and weaknesses of this technique. We demonstrate that determinations of average energy and energy flux from a single measurement of two LBH emissions may be used to estimate column-integrated ionospheric conductances. In addition, we examine common assumptions regarding the energy flux scaling and the average value of a Gaussian energy distribution, and examine the conditions of their validity.

## MODELS

Conductances are directly proportional to the corresponding ionospheric electron densities. While FUV emissions may be used to infer characteristics of the auroral processes, they must be coupled with additional information to provide the electron

densities needed for the conductance determination. This information may be provided by ground-based radar measurements, by *in situ* measurements, or by numerical models. We calculate conductances using the densities, temperatures, and magnetic field strengths provided by the field line interhemispheric plasma (FLIP) model [Torr *et al.*, 1990]. The FLIP model solves the coupled time-dependent equations for energy, momentum, continuity, and photoelectron and auroral transport along a magnetic field line extending between the northern and southern hemispheres. The complete chemistry in the model is presented by Torr *et al.* [1990] and Torr [1985].

Incident auroral fluxes are modeled with a two-stream electron energy-loss model [Richards and Torr, 1990] and input to the FLIP model. The two-stream auroral model gives excellent agreement with the more detailed multistream calculations of Strickland *et al.* [1983] and Daniell and Strickland [1986]. The auroral code is optimized through the use of variable energy and altitude grids to calculate the degraded energy spectrum of the incident electron flux and the subsequent emission of a number of prominent auroral emissions, including O I (1356 Å) and the Lyman-Birge-Hopfield band system of N<sub>2</sub>. The incident auroral particle flux is assumed to be electrons only; precipitating ion fluxes are not modeled. Both the auroral and FLIP models use the MSIS-86 thermospheric model of Hedin [1987].

For this study, the incident auroral electron fluxes are modeled by Maxwellian energy distributions with average energies between 500 eV and 20 keV and energy fluxes between 1 and 10 erg cm<sup>-2</sup> s<sup>-1</sup>. Additionally, for comparison, calculations using Gaussian energy distributions are made for the same range of average energy and energy flux. Local ionospheric conditions are modeled for a flux tube characterized by an L-shell of 5 and magnetic longitude of 180° for midwinter conditions (day=356) and near local midnight (local time=1.4 hours; solar zenith angle=127°). As a consequence, the ionospheric conductances are assumed to be solely of auroral origin, i.e., there is no EUV contribution. In geographic coordinates, the flux tube is located at (74N, 111E) in the northern

hemisphere and (51S, 111E) in the southern hemisphere; the results presented are for the northern location. We have modeled different activity cases by adjusting the  $F_{10.7}$  and  $A_p$  model inputs. Maximum conditions are represented by  $F_{10.7}=200$  and  $A_p=100$ ; moderate conditions by  $F_{10.7}=110$  and  $A_p=20$ ; and minimum conditions by  $F_{10.7}=75$  and  $A_p=4$ . Results are presented for the moderate case except where noted.

The Pedersen volume conductivity,  $\sigma_P$ , is a function of the charged particle mobility in the direction of the local electric field and perpendicular to the local magnetic field. The Hall conductivity,  $\sigma_H$ , is dependent on the mobilities in the direction perpendicular to both the  $E$ - and  $B$ -fields.

$$\sigma_P = \frac{e}{B} \left[ n_e k_P^e + \sum_i n_i k_P^i \right] \quad (1a)$$

$$\sigma_H = \frac{e}{B} \left[ n_e k_H^e - \sum_i n_i k_H^i \right] \quad (1b)$$

The mobility coefficients are functions of the ratios of the collision frequency  $\nu$  and the gyrofrequency  $\Omega$ .

$$k_P^e = \frac{(\sum_k \nu_{ek} + \sum_i \nu_{ei}) / |\Omega_e|}{1 + ((\sum_k \nu_{ek} + \sum_i \nu_{ei}) / |\Omega_e|)^2} \quad (2a)$$

$$k_P^i = \frac{\sum_k \nu_{ik} / \Omega_i}{1 + (\sum_k \nu_{ik} / \Omega_i)^2} \quad (2b)$$

$$k_H^e = \frac{1}{1 + ((\sum_k \nu_{ek} + \sum_i \nu_{ei}) / |\Omega_e|)^2} \quad (2c)$$

$$k_H^i = \frac{1}{1 + (\sum_k \nu_{ik} / \Omega_i)^2} \quad (2d)$$

Our model includes three collisional interactions: ion-neutral (subscript  $ik$  in equations 2), electron-neutral ( $ek$ ), and electron-ion ( $ei$ ). The electron-neutral collision frequencies



are from *Schunk and Nagy* [1978]. The electron-ion and ion-neutral collision frequencies are from *Schunk and Nagy* [1980] except for the  $O^+-O$  collision frequency, which is taken from *Salah* [1993]. In practice, the conductivities below 250 km are dominated by the ion-neutral collision frequencies. The electron collision frequencies make no significant contributions to the conductivities, except above 250 km where the electron-ion collision frequency contributes slightly. For completeness, we include all three collision frequencies in the results discussed below.

Ionospheric conductivities are dependent on ionization due to both solar EUV illumination and incident particle flux. The combined FLIP and auroral models provide ionization from both sources. *Brekke and Hall* [1988] noted potential difficulties from not separating auroral and non-auroral ionization sources in conductance calculations. As noted above, we have chosen winter midnight conditions to minimize the solar EUV ionization sources as we are primarily interested in this study in the correlations of conductance with emissions from auroral particle fluxes. However, there are still nighttime sources from scattered light and starlight. To ensure we are dealing only with auroral ionization sources, we have subtracted underlying, i.e., non-auroral, ionization sources from the total ion production. Similar corrections are performed for the auroral emissions. This correction for non-auroral sources is significant principally for incident electron fluxes with characteristic energies below 1 keV.

*Moen and Brekke* [1990], using incoherent scatter radar measurements, derived quiet-time conductances due to solar EUV ionization and concluded that ion composition variations have little effect during solar minimum conditions. They noted that the height-dependent conductivities can be well represented without the explicit ion summations used in Eqs. (1). The present study, however, focuses only on auroral ionization sources. Low-energy auroral conductivities may be quite sensitive to ion composition. Therefore, the ion densities used are those of the major ion species ( $NO^+$ ,  $O_2^+$ ,  $N_2^+$ ,  $O^+$ , and  $N^+$ ). Local charge neutrality is assumed to hold; hence the electron density is taken to be the sum

of the ion densities. Only the three prominent neutrals are considered: O<sub>2</sub>, N<sub>2</sub>, and O. The ions are assumed to have a common temperature.

The column integrated conductances are the sum of the volume conductivities over the column height.

$$\Sigma_{P,H} = \int \sigma_{P,H} dz \quad (3)$$

The integration in Eq. (3) spans the entire range of available data (90 to 500 km). Column integrated conductances are a function of the average energy of the incident particle flux (Figure 1). The figure also shows conductances from *Vickrey et al.* [1981] and *Rasmussen et al.* [1988] for comparison. The three studies essentially agree for the Pedersen conductance with some differences for the Hall conductance. *Rasmussen et al.* [1988] noted that the choice of thermospheric model can significantly influence the modeled conductances. *Vickrey et al.* [1981] used the 1000 K thermosphere of *Banks and Kockarts* [1973] while *Rasmussen et al.* [1988] used the MSIS-83 model [*Hedin*, 1983]. We use the MSIS-86 model [*Hedin*, 1987]. *Brekke and Hall* [1988] used a simplified analysis to show that the Hall-to-Pedersen conductance ratio is directly proportional to  $k = \nu_{ik} / n_k$ . Therefore, differences in the Hall profiles may represent differences in choice and calculation of collision frequencies, in addition to differences in thermospheric models. In the discussions below, we use the term conductivity for the local volume conductivity and the term conductance will be reserved for the column integrated conductivities as given in Eq. (3). The units of volume conductivity are mho/m (siemens/m in SI units); those of conductance are mho (siemens).

#### DEPENDENCE ON ENERGY FLUX

The volume conductivities are dependent on the electron and ion densities which, in turn, are functions of the total incident energy flux. The continuity equation for the ion density,  $N_i$ , is given by

$$\frac{\partial N_i}{\partial t} = Q_i - L_i - (\nabla \cdot \mathbf{v}_i) N_i \quad (4)$$

where  $Q_i$  is the ion production rate,  $L_i$  is the corresponding loss rate, and the final term represents transport processes. As used here, the subscript  $i$  identifies total production and loss rates for all ion states. The principal losses are dissociative recombination,



and ion-atom interchange,



[Torr, 1985]. For illustration, we assume the recombination reactions of Eq. (5) proceed with a common recombination rate,  $\alpha$ . Similarly, we assume the interchange reactions of Eq. (6) can be described by a common reaction rate,  $k$ . Under these assumptions, the loss rate,  $L_i$ , is given by

$$L_i = \alpha[e]\{[N_2^+] + [NO^+] + [O_2^+]\} + k[O^+]\{[N_2] + [O_2]\} \quad (7)$$

where square brackets are used to denote number density of a given species.

If we ignore the transport term in Eq. (4) and assume equilibrium conditions, the production and loss rates can be equated. In the *F1* region at about 150 km, the dissociative recombination rate is the rate limiting process in Eq. (7). Furthermore, the sum of ion species in Eq. (7) is equal to the electron density at this altitude, so the production rate can be written as

$$Q = \alpha[e]^2 \quad (8)$$

where we have dropped the subscript  $i$  in recognition of the fact that the total ion and electron densities are equal. In the  $F2$  region between 200 and 400 km, the ion-atom interchange reactions of Eq. (6) are the rate limiting process. Furthermore, the  $O^+$  is the dominant ion species and can be taken as equal to the electron density. Under these conditions the production rate is

$$Q = k[e]([N_2] + [O_2]). \quad (9)$$

In both cases, the electron density can be solved for in terms of the production rate,

$$[e] = cQ^\gamma \quad (10)$$

where  $c$  is a proportionality constant and  $\gamma$  ranges from 0.5 at lower altitudes to 1.0 at higher altitudes. Since the ionization rate  $Q$  is proportional to the incident energy flux and the conductances are linear functions of the ion densities, the column conductances will scale with the energy flux, i.e.,

$$\Sigma_{P,H} = c E_f^\gamma \quad (11)$$

where  $E_f$  is the incident energy flux and  $c$  is, again, a proportionality constant. Since the conductivities typically peak in the lower thermosphere, it is usually assumed that  $\gamma=0.5$ . For example, *Moen and Brekke* [1993] and *Robinson and Vondrak* [1984] noted that column-integrated conductances due to only EUV ionization vary with the square root of the 10.7-cm solar flux, which is assumed to be proportional to the incident energy flux. A value for  $\gamma$  of 0.5 is strictly valid, however, only below about 150 km where dissociative recombination is the important loss rate.

Since we are discussing only auroral ionization sources, the ionization profiles peak at different altitudes depending on the average energy of the incident particle flux. Hence a single scaling will not necessarily be appropriate for all average energies. This is especially significant for relatively narrow energy distributions, such as the Gaussian used for

comparison below. Broader distributions, e.g. Maxwellian, will produce ionization across a greater altitude range, resulting in smaller variations in  $\gamma$  with average energy. In Figure 2 the column-integrated Pedersen conductivity is shown as a function of the incident energy flux for several average energies. Results for both Gaussian (dashed line) and Maxwellian (solid line) distributions are shown. In Table 1 we give the exponent  $\gamma$  from Eq. (11) as a function of the average energy of an incident electron flux. The exponent was obtained from a fit to column conductivities modeled with incident energy fluxes ranging from 1 to 5 erg cm<sup>-2</sup> s<sup>-1</sup>. For energies below about 2.5 keV  $\gamma$  exceeds 0.5 by more than 20% for the Pedersen conductances.

#### DEPENDENCE ON ENERGY DISTRIBUTION

The choice of modeled incident energy distribution can also be significant for low-energy fluxes, as shown in Figure 3. In the figure we show Hall conductivity profiles modeled for Gaussian and Maxwellian distributions with an average energy of 500 eV and an incident energy flux of 1 erg cm<sup>-2</sup> s<sup>-1</sup>. We define the Gaussian energy distribution as

$$f_{\text{gauss}}(E) = \frac{Q}{\pi^{1.5} W E_c^2} \exp\left[-\left(\frac{E-E_c}{W E_c}\right)^2\right] \quad (12)$$

and the Maxwellian distribution as

$$f_{\text{max}}(E) = \frac{Q E}{2\pi E_c^3} \exp\left[-\left(\frac{E}{E_c}\right)\right] \quad (13)$$

where  $Q$  sets the incident energy flux,  $W$  sets the width of the Gaussian distribution, and  $E_c$  is the characteristic energy of the incident distribution. These are the same distributions used by *Strickland et al.* [1983] except that we have replaced the Gaussian scale parameter  $W$  of *Strickland et al.* [1983] with  $W E_c$  in Equation (12). As used here,  $W$  is a dimensionless parameter. For comparison with the Maxwellian distribution, we set the Gaussian scale parameter  $W=0.25$ . The choice of this parameter is not important in itself as we are not trying to match a particular auroral energy distribution at this point. This

value was chosen to match that of *Strickland et al.* [1983]. The average energy  $\langle E \rangle$  of an energy distribution  $f(E)$  is taken to be

$$\langle E \rangle = \frac{\int_0^{\infty} E f(E) dE}{\int_0^{\infty} f(E) dE} . \quad (14)$$

*Robinson et al.* [1987] discussed the dependence of calculated conductivities on the choice of energy distribution and addressed potential confusion arising from the use of different energy distributions. They pointed out that the average energy of the asymmetric Maxwellian distribution is twice its characteristic energy. The Gaussian energy distribution used in Figure 3, however, is symmetric and the average and characteristic energies are the same. In an appendix, we examine conditions under which the average and characteristic energies of a Gaussian energy distribution may differ significantly. For a given average energy, the high-energy tail of the Maxwellian results in more ionization at lower altitudes than from the Gaussian used here with  $W=0.25$  (Figure 4). The additional ionization between 110 km and 180 km results in increased Hall conductivity over the same altitude range. The difference in conductivity for the two energy distributions is not significant for incident fluxes with average energies above about 5 keV.

The choice of energy distribution also affects modeled FUV auroral emissions, although to a much smaller degree. *Germany et al.* [1994] examined FUV auroral emissions as a function of energy distribution and found relatively small (<30%) dependence for column-integrated emissions. The observed differences were governed principally by line-of-sight loss mechanisms, i.e., absorption by  $O_2$  in the Schumann-Runge absorption continuum (1300 - 1750 Å). Consequently, the differences are largest for average energies of 10 keV.

*Robinson et al.* [1987] obtained good agreement between conductances calculated with energy spectra measured by the Hilat satellite and those based on a Maxwellian energy distribution. We use the Maxwellian distribution given in Eq. (13) without attempting to include more detailed modifications, e.g., a low- or high-energy tail [*Meier et al.*, 1989; *Strickland et al.*, 1993]. To facilitate comparison with other energy distributions, we present results as a function of average energy (twice the Maxwellian characteristic energy). If the maximum modeled energy in our auroral code is set too low there will be significant truncation of the high-energy tail of the Maxwellian distribution. We avoid this potential problem by setting the maximum modeled energy to be 100 keV, well above the largest average energy (20 keV) modeled here.

The curve labeled “nighttime” in Figures 3 and 4 is due to non-auroral ionization sources included in the FLIP model, principally from resonantly-scattered sunlight, airglow, and starlight [*Strobel et al.*, 1980]. The nighttime ion production rates are typically much smaller than those from auroral ion production. For incident fluxes with low average energies, however, the electrons do not penetrate into the E-region, leaving the nighttime photoionization as the dominant ion source in the lower thermosphere. The contribution to the conductivities from nighttime photoionization can be significant for low-energy auroras. As noted above, the nighttime ionization sources are subtracted from the results shown below.

#### CONDUCTIVITIES FROM AURORAL EMISSION RATIOS

The principal requirement for remote determination of both the Pedersen and Hall conductivities is a remote diagnostic of the characteristic energy and of the energy flux of the incident auroral flux. Such diagnostics can be provided from ratios of selected LBH bands [*Germany et al.*, 1990]. In Figure 5 we show the column-integrated intensity of two LBH auroral emissions (LBH (1464 Å) and LBH (1838 Å)) as a function of characteristic energy for a  $1 \text{ erg cm}^{-2} \text{ s}^{-1}$  incident energy flux. The LBH emission ratio (Figure 6) is a

clear function of characteristic energy and, unlike similar ratios using OI emissions, is virtually independent of seasonal and solar cyclic changes in neutral composition. The ratio thus represents a particularly useful tool for the determination of the characteristic energy of precipitating electrons.

The utility of these emission ratios is based on the absorption of FUV auroral emissions via the O<sub>2</sub> Schumann-Runge absorption continuum (1300 - 1750 Å). Because the LBH emissions are excited solely by electron impact the LBH column-intensity for a nightside aurora is a measure of the total energy flux, provided there are no significant loss mechanisms, e.g., O<sub>2</sub> absorption, in the viewing column. Longer-wavelength LBH emissions, such as LBH 1838, can thus be used as remote diagnostics of energy flux while shorter-wavelength, energy-dependent emissions (LBH 1464) may be used in conjunction with the longer-wavelength emissions to monitor average energy. The ratio of LBH 1838 and LBH 1464 serves as an indicator of characteristic energy that is independent of the incident energy flux.

With the use of the LBH emissions as a remote diagnostic of characteristic energy and energy flux, the integrated conductivities may be determined. In essence, we replace the average energy scale in Figure 1 with the LBH emission ratio and then scale by the incident energy flux as determined from the long-wavelength LBH measurement. This is shown in Figure 7 in which the conductances are plotted as a function of the LBH emission ratio. (The individual points are modeled for average energies of 0.5, 1, 2.5, 3.5, 5, 7.5, 10, 12.5, 15, 17.5, and 20 keV.) In Figure 8 the dependence of conductivities derived from the LBH emission ratio is shown as a function of activity. The activity levels were varied by changing the  $F_{10.7}$  and  $A_p$  indices, as discussed above. Since the LBH emission ratio is relatively insensitive to these changes, most of the variation seen in Figure 8 is due to changes in the ionization and temperature profiles.

It is at the low energies that the present method of inferring the conductivities is least sensitive because the LBH ratio is relatively insensitive to characteristic energies below 2



keV. In addition, the conductivities are more sensitive to solar activity changes in energy distribution at low energies. Furthermore, though they were removed for this study, nighttime ionization sources can exceed ion production in soft auroras. Clearly care must be taken when modeling lower energy auroras. These difficulties may conceivably be addressed by employing other remote diagnostics with greater sensitivity to low energies, such as the O I (1356 Å) to LBH (1838 Å) ratio. Unfortunately, using the O I (1356 Å) line to obtain increased sensitivity to low energies has the disadvantage of increased sensitivity to thermospheric perturbations. In addition, working with the 1356-Å emission is complicated by additional difficulties, e.g., blending with the LBH (1354 Å) emission.

### SUMMARY

In this study the calculation of ionospheric conductivities is linked to remote observables (FUV LBH emissions) which could be observed by a space-based, nadir-looking instrument with selected bandpasses in the far ultraviolet. The study is limited to auroral particle sources and examination of EUV ionization sources is deferred to a future study. A single observation of a pair of LBH emissions, one with wavelength less than about 1750 Å and the other at longer wavelengths, is sufficient to characterize both the incident energy flux and its characteristic energy. This characterization is relatively insensitive to changes in the ionosphere and thermosphere due to solar cyclic variations. Just two parameters, energy flux and characteristic energy, convey sufficient information to characterize the incident particle flux and, in turn, to infer the resultant ionospheric conductivities. The LBH emission ratio is least sensitive to changes in energy for average energies below 1 keV. In addition, the low-energy conductance calculations are particularly dependent on the choice of energy spectrum. We also examine the square-root scaling rule with incident energy flux usually applied to conductances. For our modeled cases, auroras with average energies greater than about 5 keV can be scaled by the square

root of the energy flux with errors less than about 20%. However, below 5 keV the scaling may deviate significantly from a power of 0.5, dependent on the modeled incident energy distribution.

## APPENDIX

It is common to state that the mean energy of a Gaussian energy distribution is its central, or characteristic, energy. Since energy is constrained to be non-negative, however, the distribution may be truncated at zero energy. If so, the distribution will be assymetric and the mean energy will be larger than the characteristic energy. For example, in Fig. A1, the curve labelled with  $w=0.75$  is truncated at zero. Therefore its mean energy is somewhat larger than the 5 keV mean shared by the other distributions. The discussion below details the conditions under which the mean energy of a Gaussian distribution may be taken as equal to its characteristic energy.

The Gaussian distribution is defined in terms of two parameters, the central value  $\mu$  and a width factor  $\sigma$ .

$$f_g(E; \mu, \sigma) = A e^{-\left(\frac{E-\mu}{\sigma}\right)^2} \quad (\text{A1})$$

The distribution in Eq. (A1) is the same as that given in Eq. (12) with  $\mu=E_c$  and  $\sigma=wE_c$ .

The width factor is related to the full width at half maximum ( $\Gamma$ ) by setting  $f_g(E+\Gamma/2; \mu, \sigma) = 0.5 f_g(\mu; \mu, \sigma)$ .

$$\Gamma = 2\sqrt{\ln 2} \sigma \quad (\text{A2})$$

The mean energy is the weighted average across the distribution,

$$\langle E \rangle = \frac{\int_0^\infty E f_g(E) dE}{\int_0^\infty f_g(E) dE} \equiv \frac{I_1}{I_2} \quad (\text{A3})$$

where the limits of integration reflect the constraint that energy be non-negative.

The integral in the denominator is evaluated first, using a transformation to the variable

$$\begin{aligned}
 I_2 &= \int_0^{\infty} f_g(E) dE \\
 &= A\sigma \int_{-\gamma}^{\infty} e^{-z^2} dz
 \end{aligned}
 \tag{A4}$$

where

$$\begin{aligned}
 z &\equiv \frac{E - \mu}{\sigma} \\
 dE &= \sigma dz
 \end{aligned}
 \tag{A5}$$

and  $\gamma$  is the ratio of the central energy and the width parameter,

$$\gamma \equiv \frac{\mu}{\sigma} .
 \tag{A6}$$

The integral is evaluated in terms of the error function,

$$\begin{aligned}
 I_2 &= A\sigma \left\{ -\int_0^{\gamma} e^{-z^2} dz + \int_0^{\infty} e^{-z^2} dz \right\} \\
 &= A\sigma \frac{\sqrt{\pi}}{2} \{ \text{erf}(\gamma) + 1 \}
 \end{aligned}
 \tag{A7}$$

where

$$\begin{aligned}
 \text{erf}(z) &\equiv \frac{2}{\sqrt{\pi}} \int_0^z e^{-t^2} dt \\
 \text{and } \text{erf}(-z) &= -\text{erf}(z) .
 \end{aligned}
 \tag{A8}$$

The integral in the numerator of Eq. (A3) is now evaluated, again using the transformation from Eq. (A5).

$$\begin{aligned}
I_1 &= \int_0^\infty E f_g(E) dE \\
&= A \sigma \int_{-\gamma}^\infty (\sigma z + \mu) e^{-z^2} dz \\
&= A \sigma^2 \int_{-\gamma}^\infty z e^{-z^2} dz + \mu I_2
\end{aligned} \tag{A9}$$

Note that the integral is given in terms of  $I_2$ , the integral in Eq. (A7). To complete the evaluation, a second transformation is used.

$$\begin{aligned}
y &\equiv z^2 \\
dy &= 2z dz
\end{aligned} \tag{A10}$$

$$\begin{aligned}
I_1 &= \frac{A \sigma^2}{2} \int_{\gamma^2}^\infty e^{-y} dy + \mu I_2 \\
&= \mu \left( \frac{A \sigma}{2 \gamma} e^{-\gamma^2} + I_2 \right)
\end{aligned} \tag{A11}$$

In the last step of Eq. (A11), the definition of  $\gamma$  is used to introduce a common factor of  $\mu$  in both terms.

The mean energy can now be written, using Eqs. (A3), (A7), and (A11), as

$$\langle E \rangle = \frac{I_1}{I_2} = \mu F(\gamma) \tag{A12}$$

where  $F(\gamma)$  is given by

$$F(\gamma) = 1 + \frac{e^{-\gamma^2}}{\sqrt{\pi} \gamma \{\text{erf}(\gamma) + 1\}}. \tag{A13}$$

Figure A2 shows  $F(\gamma)$  for values of  $\gamma$  between 0.1 and 10. As can be seen, for values of  $\gamma$  greater than 1.5 the low energy truncation of the distribution is negligible and the mean

energy can taken to be the characteristic energy. For values of  $\gamma$  below 1.5, the truncation is significant and the approximation that  $\langle E \rangle = E_c$  is not valid. Since  $\gamma$  is the ratio of the central energy to the width of the distribution, we see that the approximation of the mean energy by the characteristic energy fails for energy distributions that are very wide compared with the central energy.

In this work, we set  $\sigma = w\mu$ . The requirement that  $\gamma$  be greater than 1.5 therefore translates to the condition that  $w$  be less than 0.667. For our work,  $w = 0.25$  and the mean energy may thus be safely approximated by the characteristic energy.

#### ACKNOWLEDGEMENTS

We acknowledge the helpful comments of the reviewer. This work was supported by NASA grants NAGW-996 and NAG8-834, NASA contract NAS8-38145, and NSF grant ATM-9018165 to the University of Alabama in Huntsville.

## REFERENCES

- Banks, P. M., and G. Kockarts, *Aeronomy*, Academic, San Diego, Calif., 1973.
- Basu, Sunanda, S. Basu, R. Eastes, R. E. Huffman, R. E. Daniell, P. K. Chaturvedi, C. E. Valladares, and R. C. Livingston, Remote sense of auroral *E* region plasma structures by radio, radar, and UV techniques at solar minimum, *J. Geophys. Res.*, **98**, 1589, 1993.
- Brekke, A., and C. Hall, Auroral ionospheric quiet summertime conductances, *Ann. Geophys.*, **6**, 361, 1988.
- Brekke, A., and J. Moen, Observations of high latitude ionospheric conductances, *J. Atm. Terr. Phys.*, **55**, 1493, 1993.
- Daniell, R. E., and D. J. Strickland, Dependence of the auroral middle UV emissions on the incident electron spectrum and neutral atmosphere, *J. Geophys. Res.*, **91**, 321, 1986.
- Fuller-Rowell, T. J., and D. S. Evans, Height-integrated Pedersen and Hall conductivity patterns inferred from the TIROS-NOAA satellite data, *J. Geophys. Res.*, **92**, 7606, 1987.
- Germany, G. A., M. R. Torr, D. G. Torr, and P. G. Richards, Use of FUV auroral emissions as diagnostic indicators, *J. Geophys. Res.*, **99**, 383, 1994.
- Germany, G. A., M. R. Torr, P. G. Richards, and D. G. Torr, The dependence of modeled OI 1356 and N<sub>2</sub> Lyman Birge Hopfield auroral emissions on the neutral atmosphere, *J. Geophys. Res.*, **95**, 7725, 1990.
- Hedin, A. E., MSIS-86 thermospheric model, *J. Geophys. Res.*, **92**, 4649, 1987.



- Hedin, A. E., A revised thermospheric model based on mass spectrometer and incoherent scatter data: MSIS-83, *J. Geophys. Res.*, 88, 10170, 1983.
- Kamide, Y., J. D. Craven, L. A. Frank, B.-H. Ahn, and S.-I. Akasofu, Modeling substorm current systems using conductivity distributions inferred from DE auroral images, *J. Geophys. Res.*, 91, 11235, 1986.
- Meier, R. R., D. J. Strickland, J. H. Hecht, and A. B. Christensen, Deducing composition and incident electron spectra from ground-based auroral optical measurements: A study of auroral red line processes, *J. Geophys. Res.*, 94, 13541, 1989.
- Meng, C. I., and R. E. Huffman, Preliminary observations from the auroral and ionospheric remote sensing imager, *Johns Hopkins APL Tech. Dig.*, 8, 303, 1987.
- Moen, J., and A. Brekke, The solar flux influence on quiet time conductances in the auroral ionosphere, *Geophys. Res. Lett.*, 20, 971, 1993.
- Moen, J., and A. Brekke, On the importance of ion composition to conductivities in the auroral ionosphere, *J. Geophys. Res.*, 95, 10687, 1990.
- Rasmussen, C. E., R. W. Schunk, and V. B. Wickwar, A photochemical equilibrium model for ionospheric conductivity, *J. Geophys. Res.*, 93, 9831, 1988.
- Rasmussen, C. E., and R. W. Schunk, Ionospheric convection driven by NBZ currents, *J. Geophys. Res.*, 92, 4491, 1987.
- Reiff, P. H., Models of auroral zone conductances, in *Magnetospheric Currents, Geophys. Monogr. Ser.*, vol. 28, edited by T. A. Potemra, AGU, Washington, D. C., 1984.
- Rees, M. H., and D. Luckey, Auroral electron energy derived from ratio of spectroscopic emissions 1. Model computations, *J. Geophys. Res.*, 79, 5181, 1974.

- Richards, P. G., and D. G. Torr, Auroral modeling of the 3371 Å emission rate: Dependence on characteristic electron energy, *J. Geophys. Res.*, **95**, 10337, 1990.
- Richmond, A. D., and Y. Kamide, Mapping electrodynamic features of the high-latitude ionosphere from localized observations: Technique, *J. Geophys. Res.*, **93**, 5741, 1988.
- Robinson, R. M., and R. R. Vondrak, Measurements of *E* region ionization and conductivity produced by solar illumination at high latitudes, *J. Geophys. Res.*, **89**, 3951, 1984.
- Robinson, R. M., R. R. Vondrak, and T. A. Potemra, Auroral zone conductivities within the field-aligned current sheets, *J. Geophys. Res.*, **90**, 9688, 1985.
- Robinson, R. M., R. R. Vondrak, K. Miller, T. Dabbs, and D. Hardy, On calculating ionospheric conductances from the flux and energy of precipitating electrons, *J. Geophys. Res.*, **92**, 2565, 1987.
- Robinson, R. M., R. R. Vondrak, J. D. Craven, L. A. Frank, and K. Miller, A comparison of ionospheric conductances and auroral luminosities observed simultaneously with the Chatanika radar and the DE 1 auroral imagers, *J. Geophys. Res.*, **94**, 5382, 1989.
- Robinson, R., T. Dabbs, J. Vickrey, R. Eastes, F. Del Greco, R. Huffman, C. Meng, R. Daniell, D. Strickland, and R. Vondrak, Coordinated measurements made by the Sondrestrom radar and the Polar Bear ultraviolet imager, *J. Geophys. Res.*, **97**, 2863, 1992.
- Roble, R. G., R. E. Dickinson, and E. C. Ridley, Global circulation and temperature structure of thermosphere with high-latitude plasma convection, *J. Geophys. Res.*, **87**, 1599, 1982.

- Salah, J. E., Interim standard for the ion-neutral atomic oxygen collision frequency, *Geophys. Res. Lett.*, 20, 1543, 1993.
- Schenkel, F. W., and B. S. Ogorzalek, Auroral images from space: Imagery, spectroscopy, and photometry, *Johns Hopkins APL Tech. Dig.*, 8, 308, 1987.
- Schunk, R. W., and A. F. Nagy, Electron temperatures in the *F* region of the ionosphere: Theory and Observations, *Rev. Geophys. Space Phys.*, 16, 355, 1978.
- Schunk, R. W., and A. F. Nagy, Ionospheres of the terrestrial planets, *Rev. Geophys. Space Phys.*, 18, 813, 1980.
- Senior, C., and M. Blanc, On the control of magnetospheric convection by the spatial distribution of ionospheric conductivities, *J. Geophys. Res.*, 89, 261, 1984.
- Spiro, R. W., and R. A. Wolf, Electrodynamics of convection in the inner magnetosphere, in *Magnetospheric Currents, Geophys. Monogr. Ser.*, vol. 28, edited by T. A. Potemra, AGU, Washington, D. C., 1984.
- Steele, D. P., D. J. McEwen, and J. S. Murphree, On the possibility of auroral remote sensing with the Viking Ultraviolet Imager, *J. Geophys. Res.*, 97, 2845, 1992.
- Strickland, D. J., J. R. Jasperse, and J. A. Whalen, Dependence of auroral FUV emissions on the incident electron spectrum and neutral atmosphere, *J. Geophys. Res.*, 88, 8051, 1983.
- Strickland, D. J., R. E. Daniell, J. R. Jasperse, and B. Basu, Transport-theoretic model for the electron-proton-hydrogen atom aurora, 2. Model results, *J. Geophys. Res.* 98, 21533, 1993.
- Strobel, D. F., C. B. Opal, and R. R. Meier, Photoionization rates in the night-time *E*- and *F*-region ionosphere, *Planet Space Sci.*, 28, 1027, 1980.

- Torr, D. G., The photochemistry of the upper atmosphere, in *The Photochemistry of Atmospheres*, edited by J. S. Levine, pp. 165-278, Academic, San Diego, Calif., 1985.
- Torr, M. R., D. G. Torr, P. G. Richards, and S. P. Yung, Mid- and low-latitude model of thermospheric emissions 1.  $O^+(2P)$  7320 Å and  $N_2(2P)$  3371 Å, *J. Geophys. Res.*, **95**, 21147, 1990.
- Vickrey, J. F., R. R. Vondrak, and S. J. Matthews, The diurnal and latitudinal variation of auroral zone ionospheric conductivity, *J. Geophys. Res.*, **86**, 65, 1981.
- Vickrey, J. F., R. R. Vondrak, and S. J. Mathews, Energy deposition by precipitating particles and Joule dissipation in the auroral ionosphere, *J. Geophys. Res.*, **87**, 5184, 1982.
- Vondrak, R., and R. Robinson, Inference of high-latitude ionization and conductivity from AE-C measurements of auroral electron fluxes, *J. Geophys. Res.*, **90**, 7505, 1985.
- Wallis, D. D. and E. E. Budzinski, Empirical models of height integrated conductivities, *J. Geophys. Res.*, **86**, 125, 1981.
- Watermann, J., O. de la Beaujardiere, and F. J. Rich, Comparison of ionospheric electrical conductances inferred from coincident radar and spacecraft measurements and photoionization models, *J. Atm. Terr. Phys.*, **55**, 1513, 1993.

Fig. 1. Column-integrated Hall and Pedersen conductances for an incident energy flux of  $1 \text{ erg cm}^{-2} \text{ s}^{-1}$  and a Maxwellian energy distribution. Dashed line, *Vickrey et al.*, [1981]; solid line, *Rasmussen et al.*, [1988]; circles, this work.

Fig. 2. Column-integrated Pedersen conductances as a function of incident energy flux and average energy. Dashed line, Gaussian; solid line, Maxwellian.

Fig. 3. Hall conductivity due to an incident auroral flux with an average energy of 500 eV and an incident energy flux of  $1 \text{ erg cm}^{-2} \text{ s}^{-1}$ . Conductivities are modeled for both a Gaussian and a Maxwellian energy distribution. The curve labelled "Nighttime" is due to non-auroral sources.

Fig. 4. Electron density profiles corresponding to the Hall conductivity profile in Figure 3.

Fig. 5. Column-integrated intensity of LBH (1838 Å, 1464 Å) for a  $1 \text{ erg cm}^{-2} \text{ s}^{-1}$  incident energy flux and a Maxwellian energy distribution.

Fig. 6. Ratio of auroral LBH (1838 Å) to LBH (1464 Å) for a  $1 \text{ erg cm}^{-2} \text{ s}^{-1}$  incident energy flux. Three cases are shown:  $F_{10.7}=75$ ,  $Ap=4$ ;  $F_{10.7}=110$ ,  $Ap=20$ ;  $F_{10.7}=200$ ,  $Ap=100$ .

Fig. 7. Column-integrated Hall and Pedersen conductances as a function of auroral LBH emission ratio. The individual points are modeled for average energies of 0.5, 1, 2.5, 3.5, 5, 7.5, 10, 12.5, 15, 17.5, and 20 keV and a  $1 \text{ erg cm}^{-2} \text{ s}^{-1}$  incident energy flux.

Fig. 8. Column-integrated Hall and Pedersen conductances as a function of auroral LBH emission ratio for a  $1 \text{ erg cm}^{-2} \text{ s}^{-1}$  incident energy flux. Three cases are shown:  $F_{10.7}=75$ ,  $Ap=4$  (dot);  $F_{10.7}=100$ ,  $Ap=20$  (line);  $F_{10.7}=200$ ,  $Ap=100$  (dash).

Figure A1. Gaussian energy distributions with fixed characteristic energy and varying widths. The plots are labelled with the dimensionless parameter  $w = \sigma/\mu = 1/\gamma$ .

Figure A2.  $F(\gamma)$  as a function of  $\gamma$ .  $F(1.5) = 1.0202$

TABLE 1. Power-law dependence of conductances with energy flux.

Average Energy (keV)	$\gamma$ (Maxwellian)		$\gamma$ (Gaussian)	
	Pedersen	Hall	Pedersen	Hall
0.5	0.74	0.60	0.80	0.62
1.0	0.66	0.55	0.76	0.65
2.5	0.58	0.54	0.60	0.57
5.0	0.56	0.53	0.57	0.55
10.0	0.54	0.52	0.54	0.53
15.0	0.54	0.52	0.54	0.52

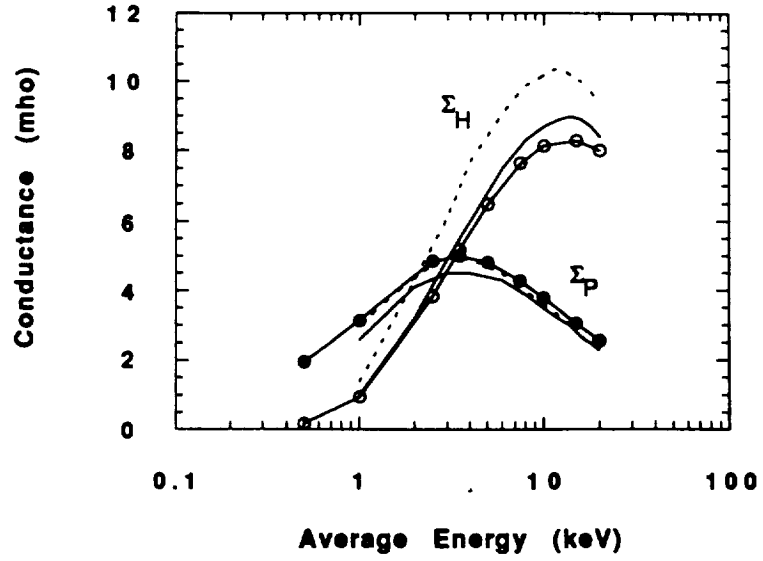


Fig. 1. Column-integrated Hall and Pedersen conductances for an incident energy flux of  $1 \text{ erg cm}^{-2} \text{ s}^{-1}$  and a Maxwellian energy distribution. Dashed line, *Vickrey et al.*, [1981]; solid line, *Rasmussen et al.*, [1988]; circles, this work.



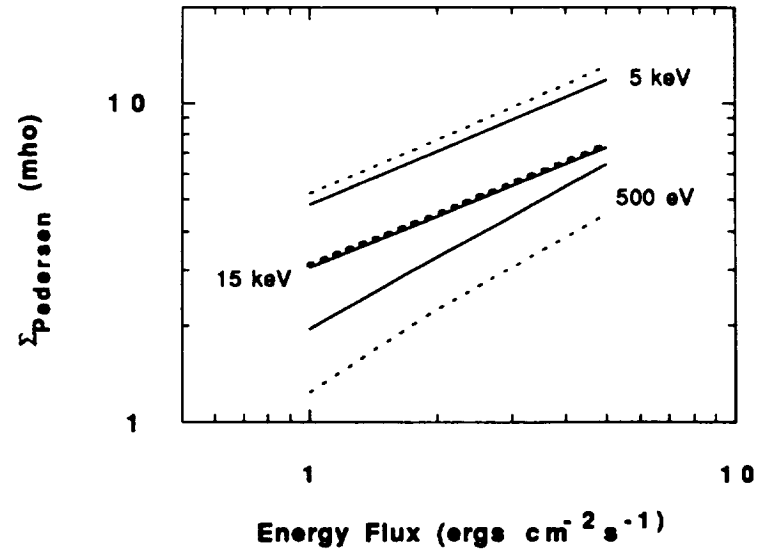


Fig. 2. Column-integrated Pedersen conductances as a function of incident energy flux and average energy. Dashed line, Gaussian; solid line, Maxwellian.

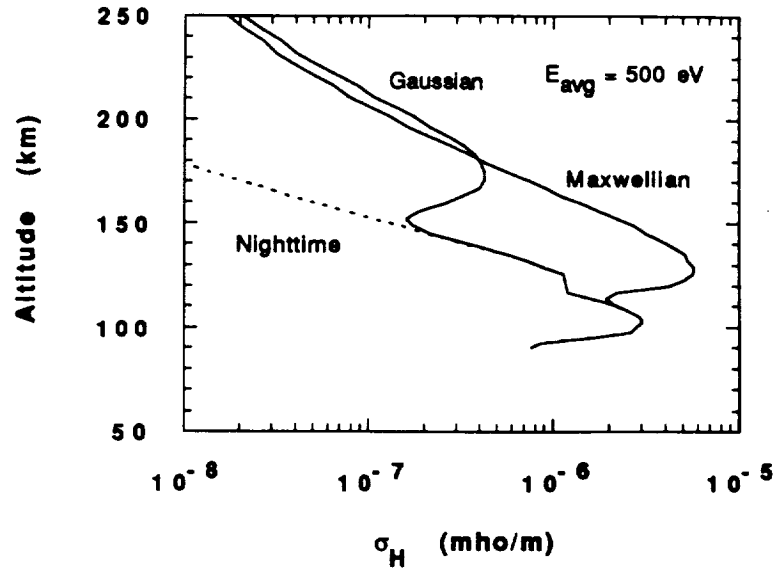


Fig. 3. Hall conductivity due to an incident auroral flux with an average energy of 500 eV and an incident energy flux of 1 erg cm<sup>-2</sup> s<sup>-1</sup>. Conductivities are modeled for both a Gaussian and a Maxwellian energy distribution. The curve labelled "Nighttime" is due to non-auroral sources.

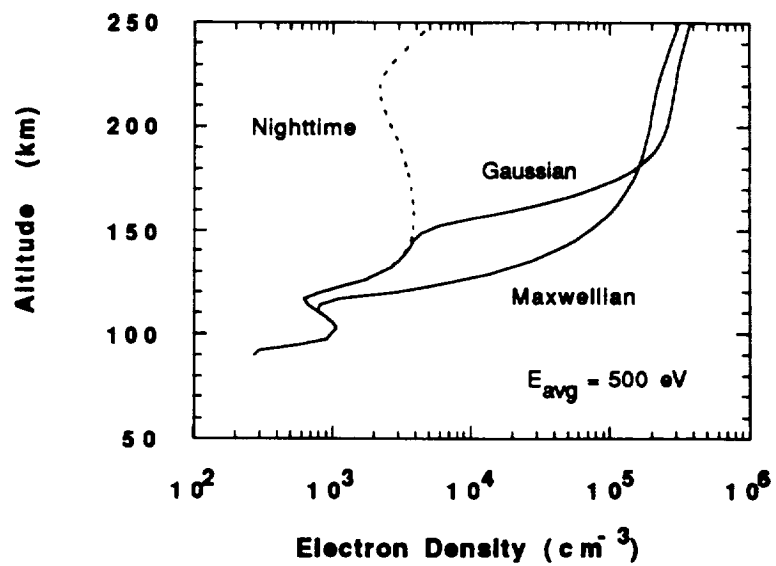


Fig. 4. Electron density profiles corresponding to the Hall conductivity profile in Figure 3.

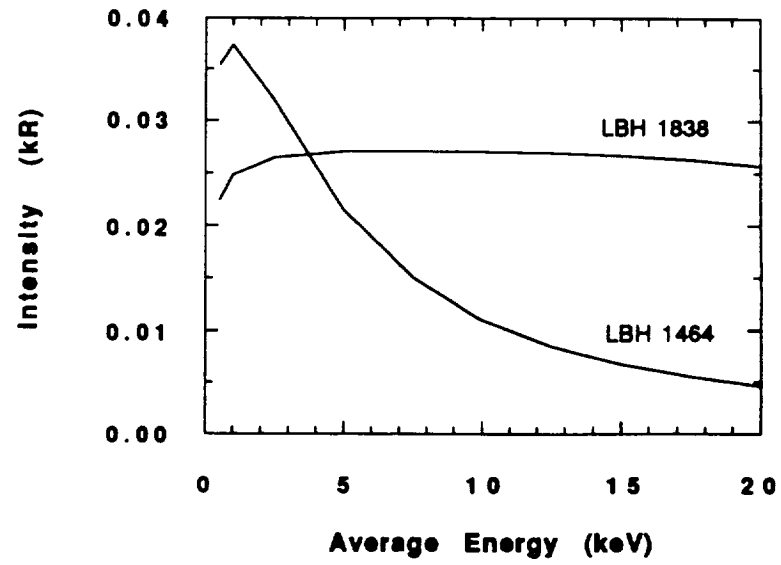


Fig. 5. Column-integrated intensity of LBH (1838 Å, 1464 Å) for a  $1 \text{ erg cm}^{-2} \text{ s}^{-1}$  incident energy flux and a Maxwellian energy distribution.

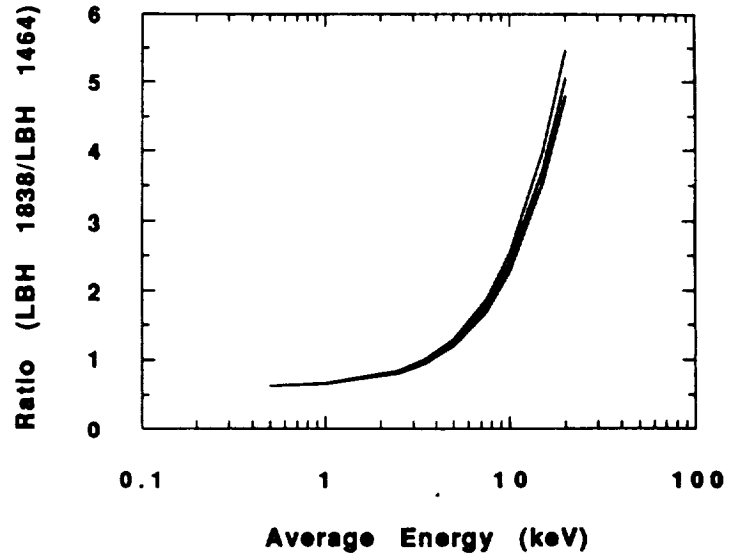


Fig. 6. Ratio of auroral LBH (1838 Å) to LBH (1464 Å) for a 1 erg cm<sup>-2</sup> s<sup>-1</sup> incident energy flux. Three cases are shown:  $F_{10.7}=75$ ,  $Ap=4$ ;  $F_{10.7}=100$ ,  $Ap=20$ ;  $F_{10.7}=200$ ,  $Ap=100$ .

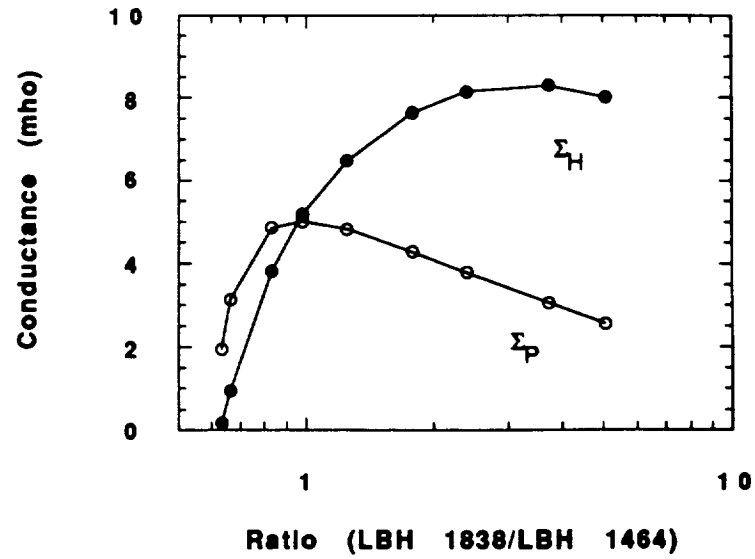


Fig. 7. Column-integrated Hall and Pedersen conductances as a function of auroral LBH emission ratio. The individual points are modeled for average energies of 0.5, 1, 2.5, 3.5, 5, 7.5, 10, 12.5, 15, 17.5, and 20 keV and a  $1 \text{ erg cm}^{-2} \text{ s}^{-1}$  incident energy flux.

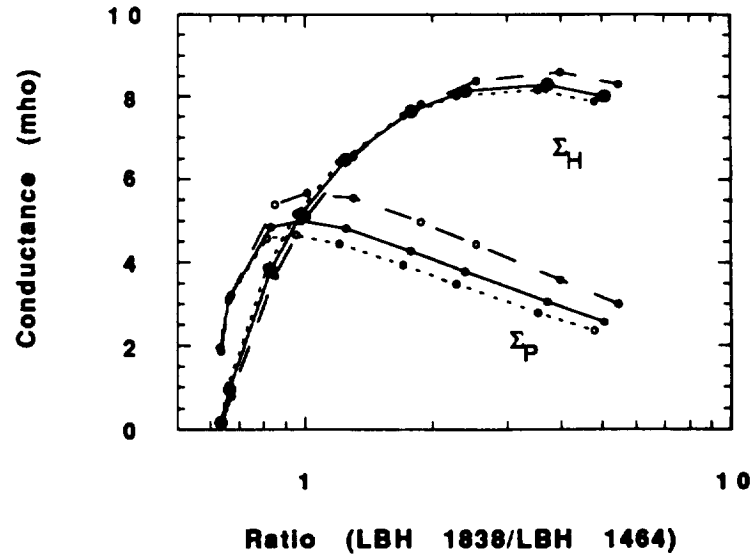


Fig. 8. Column-integrated Hall and Pedersen conductances as a function of auroral LBH emission ratio for a  $1 \text{ erg cm}^{-2} \text{ s}^{-1}$  incident energy flux. Three cases are shown:  $F_{10.7}=75$ ,  $A_p=4$  (dot);  $F_{10.7}=100$ ,  $A_p=20$  (line);  $F_{10.7}=200$ ,  $A_p=100$  (dash).

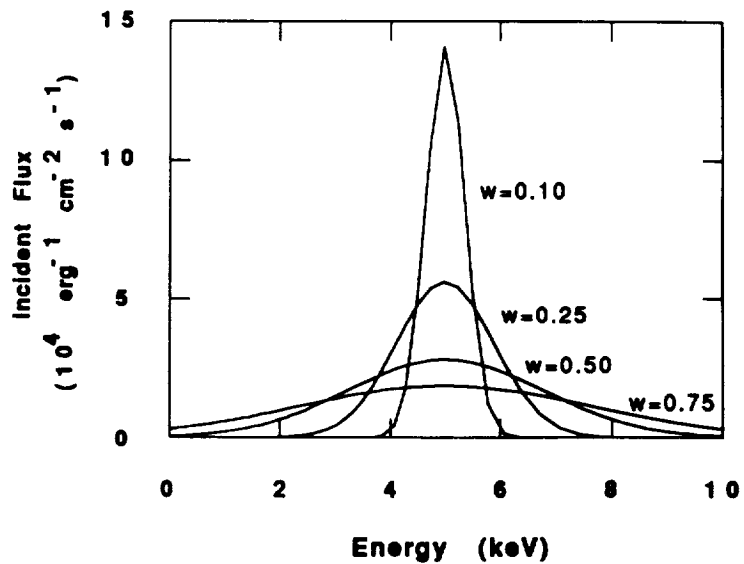


Figure A1. Gaussian energy distributions with fixed characteristic energy and varying widths. The plots are labelled with the dimensionless parameter  $w = \sigma/\mu = 1/\gamma$ .



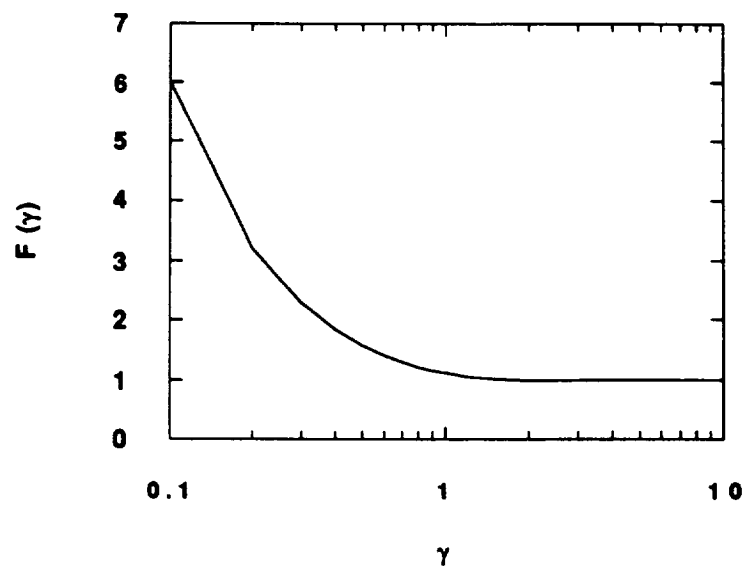


Figure A2.  $F(\gamma)$  as a function of  $\gamma$ .  $F(1.5) = 1.0202$